IJCESEN

ISSN : 2149-9144

International Journal of Computational and Experimental Science and ENgineering

Volume: 6 - Issue: 2 - 2020

ijcesen@gmail.com

Founder-Editor-in-Chief : Prof.Dr. İskender AKKURT

dergipark.org.tr/en/pub/ijcesen

Journal Info	
Web	dergipark.org.tr/en/pub/ijcesen
E-mail	ijcesen@gmail.com
ISSN	2149-9144
Frequency	March-July-November
Founded	2015
Journal Abbreviation	IJCESEN
Language	English-Turkish

Indexing/Abstracting Databases

ASOS indeks

INDEX COPERNICUS INTERNATIONAL

ISIFI – International Services for Impact Factor and Indexing

GENERALIMPACTFACTOR
Universal Digital Object Information

Google Scholar

DRJI

ISI INTERNATIONAL Scientific Indexing

publons

Cosmos

SIS

J-Gate

WorldCat

ESJI Eurasian Scientific Journal Index
www.ESJIndex.org

JIF – Global Society for Scientific Research
JIFACTOR

CiteFactor
Academic Scientific Journals

Academic Resource Index
ResearchBib

Scientific Journal Impact Factor
TOGETHER WE REACH THE GOAL

Table of Contents

International Journal of Computational and Experimental Science and ENgineering (IJCESEN)
Vol. 6-No.2 (2020) pp. 78-81
http://dergipark.org.tr/en/pub/ijcesen

ISSN:2149-9144

Research Article

Study of the Influence of Cementation Layer Thickness on Properties of Chromium Carbide Obtained by Conversion Treatment

Rabah BOUBAAYA[1,2*], Omar ALLAOUI[1], Mokhtar DJENDEL[1,2], Younes BENARIOUA[3], Zied DRISS[4]

[1]Laboratoire de Génie des procédés, Université Amar Telidji - Laghouat, Algeria
[2]Département des Sciences et Techniques, Faculté des Sciences et de la Technologie, Université de Bordj Bou Arreridj, 34000, Bordj Bou Arreridj, Algeria
[3]Département de Génie Mécanique, Faculté de la Technologie, Université de M'sila, Algeria
[4]Laboratory of Electro-Mechanic Systems (LASEM), National School of Engineers of Sfax (ENIS), Tunisia

* **Corresponding Author** : raboubaaya@yahoo.fr
ORCID:0000-0002-3672-3185

Article Info:

DOI: 10.22399/ijcesen.692070
Received : 22 February 2020
Accepted : 24 April 2020

Keywords

Steel
Carbon
Chromium
Layer
Cementing
Chromium carbide
Diffusion
Precipitation
Deposition

Abstract:

Steel substrates low carbons were face-hardened by cementing in case, and then thin layers of chromium were deposited by electrolytic way on these substrates. After deposition, the samples were exposed to isothermal annealing in the temperature of 950°C. The characterization of the thin layers was made by means of optical microscopy and interferometry Vickers micro-hardness. From the obtained results, we have established the kinetics of phase shift (under effect the layer of cementing) in the thin layers of chromium which are transformed into chromium carbide while passing by metastable phases of transition. These transformations occurred by diffusion of the carbon atoms coming from layer of cementing, germination and growth in solid phase. This fact has examined according to the temperature of annealing, the evolution of the lattice parameter and the morphology of the deposited chromium layer. As regards the mechanical properties, it was established that the micro-hardness believes with the evolution of the phase shift.

1. Introduction

Over the past two decades, the transition metal carbides of the coatings were found to be one of the most effective materials for increasing the life time of the machine components, cutting tools and forming tools, in particular to improve wear and corrosion resistance [1,2]. Among these metal compounds, chromium carbide has the best mechanical and chemical resistance in harsh conditions. Recent research on chromium carbide stressed their resistance to oxidation and corrosion and suggested that they have great potential to replace hard chrome electroplating as protective coatings [3,4]. The chromium carbide layers can be obtained by physical vapor deposition (PVD) [5,6] or thermo-reactive deposition/diffusion (TRD) technology [7,8]. In the case of PVD thickness is much less than 10 µm making those unfit also withstood the high contact pressure and further adhesion to the substrate is less than that obtained with other types of coating techniques. TRD coatings must very long process times at high temperatures. For example, a thickness 8 µm chromium carbide layer was obtained on a steel AISI D2 with a treatment at 1030 °C for 4 h [9] and a thickness of 13 µm was obtained with treatment at 1000 °C for 3 h [10]. Indeed, there are very common industrial methods that can be combined in any manner to produce chromium carbide coatings.

In order to produce a high-hardness coating, a good adhesive properties and a sufficient thickness with stand severe loading conditions, we propose an alternative technique based on a three-step process using only standard industrial methods. The first step intends to increase the carbon content at the

surface of the substrate using a standard carburizing process. The second step consists to coat the carburized material with a layer of chromium. The final step considers the heat treatment at temperatures which allow the diffusion of carbon into the surface of the material. In this work, we propose to determine the experimental conditions which allow complete conversion of the chromium layer in a uniform layer of high hardness of chromium carbide and a good adhesion to the substrate.

2. Experimental methods

2.1. Materials and coating deposition

Cylindrical steel samples were selected of 20 mm in diameter and 15 mm in length. The chemical composition of the substrate reported in Table 1 was determined by spectrometric analysis using a spectrometer HILGER.

Table 1. *Chemical composition of steel to be coated (%).*

Fe	**C**	**Si**	**Mn**	**P**	**S**	**Cr**
95.99	0.19	0.22	0.94	0.003	0.056	1.12
Mo	**Ni**	**Al**	**Co**	**Cu**	**Ti**	**Sn**
0.07	1.18	0.0116	0.01	0.20	0.0012	0.010

The preparation of the substrate consists on a mechanical polishing on each sample using abrasive papers. The finishing operation provides a good polishing with felt washed down with a suspension of alumina in water. The polished surface must be cleaned thoroughly with water and dried with compressed air and hot filtered. To conduct a comparative study, we divided the samples into 4 groups as is reported in Table 2.
Cementing is performed using a cement coke powder. To accelerate cementing process, barium carbonates $BaCO_3$ is added to coal activators.

Table 2. *Carburizing test parameters.*

Group	**I**	**II**	**III**	**IV**
Hold time	00	03 hours	06 hours	12 hours
Cementing thickness	E1= 00 mm	E2= 0.6 mm	E3= 1.3 mm	E4= 2.5 mm
Temperature		900 °C	900 °C	900 °C

Samples were chrome electroplating, the standard composition of plating bath: 250 g/1 CrO_3, 2.5 g/1 SO_4H_2, bath temperature (40 - 44 °C), antimony lead anode, retention time 0.5 hour and deposition rate of about 40 µm/h.
In order to obtain a layer of chromium carbide, chromium coated samples were a thermal annealing treatment in the temperature of 950 °C. The hold time is taken 1 hour.

2.2. Characterization and analysis techniques

Microscopic observation requires fine polishing of the surface or the cutting of the deposit to be observed. Cleaning with acetone and drying by hot air flow end the mechanical polishing. The second phase consists of a chemical attack using the product nital, the composition and proportions by volume are nitric acid (5 ml) and ethanol (95 ml). Chemical etching can reveal the different phases presenting the optical microscope. The equipment used is a universal optical metallographic microscope ZEISS type.
The micro Vickers hardness test allows us to measure the size of the indentation made on the deposit. Measurements of the micro hardness of the deposits have been made on surfaces of polished sections. The indentations under a load of 50 grams were made through a microdurometer type Buehler MICROMET (HARDNESS TESTER) which is equipped with a Vickers diamond indenter. The samples have been tested in the Vickers micro-hardness with five measurements on each sample. Considering the average value obtained over five fingerprints to reduce measurement errors.

3. Results and discussion

3.1. Morphology

Figure 1 shows the observation of metallographic faces layer/substrate after annealing at 950 °C. From these results, it has been observed that no chromium carbide trace could be revealed in the pictures corresponding the sample without cementation (e_1 = 0 mm). The sample of group II (e_2 = 0.6 mm), a chromium carbide edge occurs in the vicinity of the interface. This fact is reflected by the low diffusion of carbon cementation zone in the deposited chromium layer. In the picture corresponding to the sample of group III (e_3 = 1.3 mm), it has been noted that the microstructure is predominantly in chips arranged on the substrate surface. This kind of morphology is found in several cases of phase change in the solid state. The structure of the incipient phase is usually in the form of needles certain plane oriented parallel to the surrounding parent phase. Increasing the amount of carbon diffusion from the substrate causes a progressive propagation of chromium carbide in the deposition of chromium. For the sample of group IV (e_4 = 2.5 mm), chromium matrix is transformed completely to chromium carbides. The formed layer has a granular structure. The morphology of the deposit of chromium carbides mainly depends on the treatment temperature, which promotes the mobility of atoms in the layer and the substrate. Mobility supports

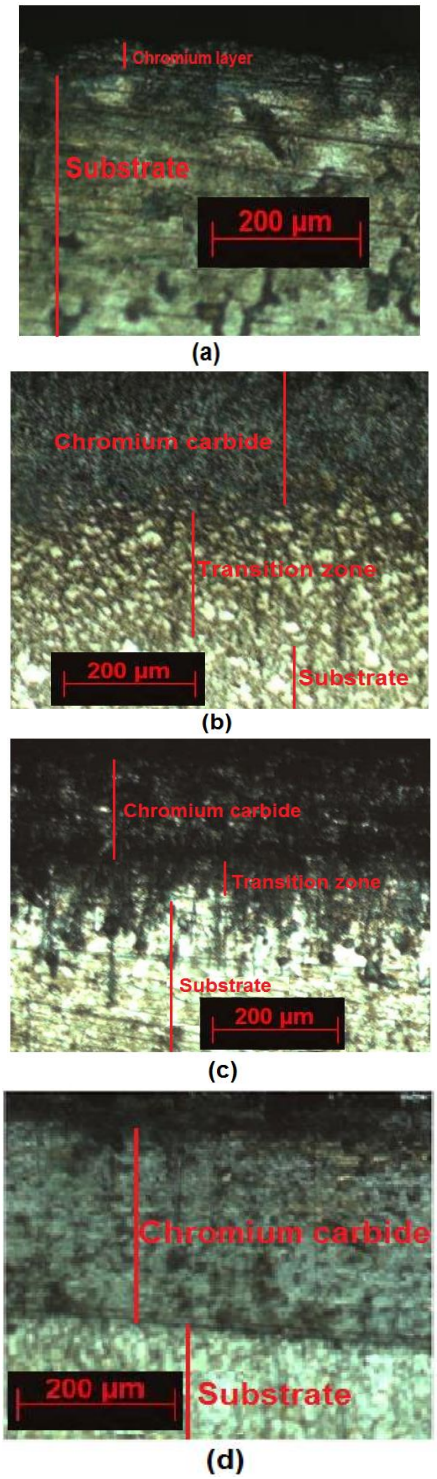

Figure 1. *Observation of metallographic faces layer/substrate after annealing at 950 °C: (a) the sample of group I (e_1 = 0 mm), (b) the sample of group II (e_2 = 0.6 mm), (c) the sample of group III (e_3 = 1.3 mm), (d) the sample of group IV (e_4 = 2.5 mm).*

traverses the diffusing carbon element concentration from the substrate to the layer.

Indeed, the thickness of the carburized layer presents a great effect on the chromium conversion rate into chromium carbides.

3.2. Hardness

Fig.2. shows the effect of the thicknesses of the carburizing layer on the micro-hardness. According

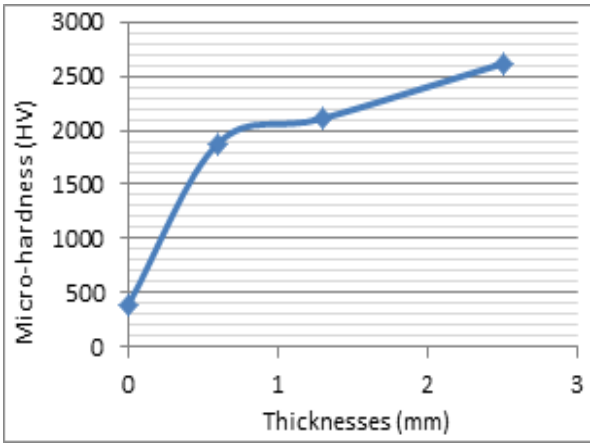

Figure 2. *Effect of carburizing layer thicknesses on micro-hardness.*

Table 3. *Change in micro-hardness depending on the thicknesses of the carburizing layer.*

Thicknesses of the carburizing layer	Micro-hardness (HV)
e_1 = 0 mm Without cementation	390
e_2 = 0.6 mm	1880
e_3 = 1.3 mm	2110
e_4 = 2.5 mm	2615

to these results, it is clear that the micro-hardness still is evolving in ascending order. Micro-hardness measurements made on samples e_3 and e_4 show that the micro-hardness is even greater than that of the samples e_1 and e_2 as it is shown in Fig.2 and reported in Table 3.

Curing would be linked to the complete formation of the chromium carbide that will cause a reinforcing of deposits. Diffusion of carbon atoms reaches the outer surface of the layer; the atoms occupy the chromium surface interstices; for thus, it will be a total loss of chromium phase.

In these conditions, the thicknesses of the carburizing layer e_2, e_3 and e_4 are equal to: 0.6, 1.3 and 2.5 mm, respectively. From these results, we can confirm that the difference between the cementation thicknesses may cause difference in micro-hardness.

4. Conclusion

In this paper, we are interested on the increasing of the performance steels chromium carbide creation with high features. For thus and after carburizing

and deposition by electroplating, a chromium layer on the steel samples (layer/substrate) were subjected to annealing at 950°C. In this temperature, the deposited film is gradually converted to chromium carbide. Phase transformation which took place primarily by diffusion of the substrate carbon atoms in the layer was determined by metallographic analysis. The hardness of the produced layers evolved following the thickness of the carburized layer. The obtained value is in agreement with the changing properties determined by microscopic observation.

Indeed, it has been noted that for sample without cementation (e_1 = 0 mm), thin films retain their monophasic character, micro-hardness of the deposited raw layer is larger than that treated. It should be noted that for the sample of group II (e_2 = 0.6 mm) and the sample of group III (e_3 = 1.3 mm), the incipient phase is increased while the chromium mother phase undergoes a decrease. This causes a high hardening of the obtained deposit. For the sample of group IV (e_4 = 2.5 mm), the chromium layer is completely converted into chromium carbides that would be responsible for the increase of the hardness.

In this case, it is both the thicknesses of the layers of carburization temperature treatment which play an essential role in the transformation of the chromium layer to chromium carbides.

References

[1] K. Hirota, K. Mitani, M. Yoshinaka, O.Yamaguchi, Simultaneous synthesis and consolidation of chromium carbides (Cr_3C_2, Cr_7C_3 and $Cr_{23}C_6$) by pulsed electric-current pressure sintering, Materials Science and Engineering A 399 (2005) 154-160. DOI:10.1016/j.msea.2005.02.062

[2] C. Y. Wei, F. S. Chen, Thermoreactive deposition /diffusion coating of chromium carbide by contact-free method, Materials Chemistry and Physics 91 (2005)192-199. DOI:10.1016/j.matchemphys.2004.11.010

[3] N. Syla, F. Aliaj, B. Dalipi, The law of growth of nitrided layer in 31CrMoV9 steel, Acta Physica Polonica A 130 (2016) 83-86. DOI:10.12693/APhysPolA.130.83

[4] G. Herranz, G. Matula, A. Romero, Effects of chromium carbide on the microstructures and wear resistance of high speed steel obtained by powder injection moulding route, Powder Metallurgy 60 (2017)120-130. DOI:10.1080/00325899.2017.1288778

[5] İ.H. Karahan, F. Tiltil, Electrodeposition and corrosive properties of environmental ZnFe /polyaniline on low carbon steel, Acta Physica Polonica A 130 (2016) 282-285. DOI: 10.12693/APhysPolA.130.282.

[6] M. Petrovic, A. Voloder, Flexural strength reduction in cemented carbides, Acta Physica Polonica A 128 (2015) B23-B25. DOI:10.12693/APhysPolA.128.B-23

[7] M. Davraz, The effect of boron compound to cement hydration and controllability of this effect, Acta Physica Polonica A 128 (2015) B26-B33. DOI: 10.12693/APhysPolA.128.B-26

[8] K. Natesan, R.N. Johnson, Corrosion resistance of chromium carbide coatings in oxygen-sulfur environments, Surface and Coatings Technology. 33 (1987) 341-351. DOI:10.1016/0257-8972(87)90200-3

[9] A. Akkas, A.B. Tugrul, B. Buyuk, A.O. Addemir, M. Marsoglu, B. Agacan, Shielding effect of boron carbide aluminium metal matrix composite against gamma and neutron radiation, Acta Physica Polonica A 128 (2015) B176-B179. DOI: 10.12693/APhysPolA.128.B-176

[10] J. E.G. Ruíz, A. R. Cristo, A. P. Ramos, R. Q. Puchol, Deposition of multicomponent chromium carbide coatings using a non-conventional source of chromium and silicon with micro-additions of boron, Materials Research 20 (2017) 168-174. DOI: 10.1590/1980-5373-mr-2016-0308.

International Journal of Computational and Experimental Science and ENgineering (IJCESEN)
Vol. 6-No.2 (2020) pp. 82-87
http://dergipark.org.tr/en/pub/ijcesen

ISSN: 2149-9144

Research Article

Study on Determination Method of Inter Well Pumping System for Liquid Supply Shortage Well

Xingyuan LIANG[1*], Jiang LEI[2], Yi LU[3]

[1]China University of Petroleum beijing, 102249, Beijing-China
[2]Drilling & Production Technology Research Institute, CNPC Chuanqing Drilling Engineering Co., Ltd., 710018, Xiaan-China
[3]Eighth Oilfield Operation, CNPC Changqing Oil Field Company, 710018,Xiaan-China

* **Corresponding Author** : lxypetro@163.com
ORCID: 0000-0002-7583-3969

Article Info:

DOI: 10.22399/ijcesen.693839
Received : 25 February 2020
Accepted : 20 April 2020

Keywords

Submergence
Intermittent recovery
Intermittent pumping

Abstract:

In the grim situation of low oil prices, the oil exploration and production companies have to reduce costs and increase benefits. The wells with deficient-liquid supply account for 20%-30% for all production wells, the proportion of the oil field in the long production time is greater. Intermittent production is an effective way to reduce the cost and increase the efficiency of the oil supply shortage. The purpose of intermittent production is to increase production and reduce cost. The key is determining a reasonable intermittent pumping system, which means develop a proper close time and open time. The author studies the dynamic liquid level variation, uses electrical power curve to solve the dynamometer card, through changing in the diagram to determine the dynamic liquid level decline rule, and then get the time of open well; through analyzing the relationship between the inflow performance of oil wells and the submergence to determine the close time.

Introduction

With the severe situation of low oil price, most of oil field take actions to reduce the expenditure and improve the benefit. There are a lot of shortage supply wells in China, and the intermittent method is an effective way to operation for these wells[1,2]. The intermittent method means that opening well to produce oil for some time, when liquid in the annulus is plenty; then shut-in the well for some time, when the liquid in the annulus decreased till the well can't work normally. The intermittent can reduce the energy consumption, improve the pump efficiency and alleviate the abrasion of pump and casing. The key of intermittent is to determine the open time and shut-in time, a reasonable intermittent regime can maximize the profile. There are four ways to determine the intermittent regime so far, which are the way of liquid curve, the way of production declination, the way of economical limitation and analytical method.

Jiang yan et al used the liquid recovery way to optimize intermittent system of liquid shortage wells[3]. Zhang maiyun et al used the annulus flow pressure distribution theory and pressure recovery well test theory to determine the intermittent system, according to the porosity and production of liquid shortage wells[4]. Lei qun pointed that the appropriate intermittent system can make the production tend to stable, and can largely improve the economic benefit[5]. Yu xiaoming concludes that most of intermittent system is unchangeable, which are easy to handle but also are not the best intermittent system[6]. Because the ability of liquid supply is different for each well at different periods, which means the intermittent system should be changed every once in a while. Guan ning used matter balance equation to get an exponential relationship between the shut-in time and production[7]. Zhou daiyu et al use the balance theory and break-even analysis to determine an economical limitation for each well, and build an

intermittent model for liquid shortage wells[8]. Liu haitao study the principles of selecting well and the characteristics of the recovery curve for liquid shortage wells, and find the suitable open time and shut-in time[9]. According to the production test and theory analysis, Yan qingyu et al determine the intermittent time by using the variation rate of casing pressure[10]. Meng xiaoling et al define a reduced pressure and develop an initial intermittent system[11]. Based on the initial system, they build a model on annulus liquid height variation, which connected with the time, and got the liquid recover line, finally gave an intermittent system for liquid shortage wells.

These ways all needs sound wave to observe the dynamic liquid depth. However, the sound wave was tested by human, and gathered the data for a period, which means it can't gather the data constantly. In this paper, we propose a new way to get the intermittent regime. First, we can draw the ground dynamometer card through the electrical parameters, which are gathered in real time; second, the dynamic liquid depth can be solved by the pump dynamometer card, which can be converted from the ground dynamometer card, and which can draw the variation curve of dynamic liquid depth during operation period; third, analyzing the relationship between the inflow performance of oil wells and the submergence to draw the recover curve during the shut-in period. Finally, the intermittent regime can be solved by the slope method.

2. Method: The determination of intermittent time

2.1 Using power curve to get the ground dynamometer card

There are all kinds of behaviors, when pumping unit is working[1]. The power of pumping unit is electricity. Electrical energy is input into the motor at the entrance, then the motor drives the donkey head movement through the belt reducer and four bar linkage. The electrical energy is converted into mechanical energy[12,13]. If the stress of suspension point is big, then the more power is needed. For example, if the pump is struck or the viscosity of oil is large, the stress of suspension point will increase, and correspondingly the input power will increase too. On the contrary, if there exists pump loss and blowing, the pumping unit need less power. Therefore, the power curve can also represent the well behavior. We set a mathematical model for loading and electrical power, through studying the relationship of power, torque and loading, which are as follows:

$$E = 9549\frac{N_r \eta i}{n_m} \qquad (1)$$

$$E = [\frac{a}{b}\mathrm{P} - \frac{c}{b}\mathrm{W}_b(\cos\theta - \frac{c}{a}\frac{a_A}{g})]\frac{r\sin a}{\sin\beta} - W_c' r\sin\varphi \qquad (2)$$

Where E is torque of crankshaft, N.m; N_r is motor power, KW; n_m is motor revolution, r/min; η is driving efficiency; I is driving ratio; R is balancing radius, which represents the distance from the core of crank balancer to crank shaft, m; P is the loading of suspension center, kN; a,b is the length of before and after beam arm, m; c is distance from the core of beam balancer to beam pivot,m; W_b is the weight of beam, kN; W_c'is the balance weight of crank radius after converting; a_A is the acceleration of suspension center, θ is the beam angel ,which is started from the horizontal position; β is the angel between after arm of beam and pitman. The figure 1 is the geometry size of pumping unit:

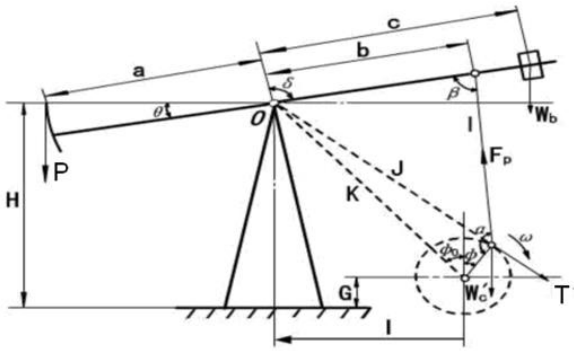

Figure 1. *Geometry size of pumping unit*

We can get the relationship between power and loading from above two formulas:

$$P = f(\mathrm{N_r}) \qquad (3)$$

The displacement curve can be solved from the crank angel, and the ground dynamometer card can be obtain from the electrical power curve.

2.2 Getting dynamic liquid level from ground dynamometer card

The pump dynamometer card can be obtain from ground dynamometer card through using Gibbs equation[12]. The dynamic liquid level is defined as the height of liquid in the annulus between tubing and casing[1]. The corresponding loading difference is the loading difference of liquid height between annulus and tubing. When the pumping unit at the bottom dead center, the stress of suspension (F_d) can be express as the following equation:

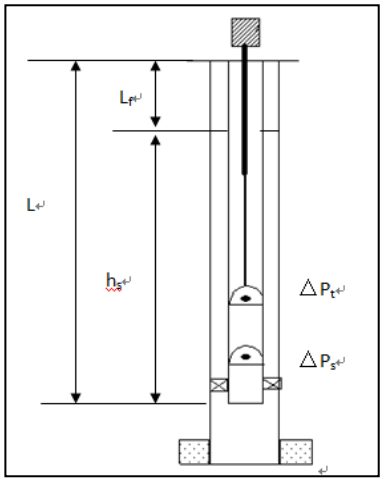

Figure 2. *The location of the static and dynamic level*

$$F_d = [\mathrm{h}_s \rho_l g + (P_c - \Delta \mathrm{p}_s) * 10^6] A_p \qquad (4)$$

When the pumping unit at the top dead center, the stress of suspension (F_u) can be express as the following equation:

$$F_u = [L\rho_l g + (P_t + \Delta p_t) * 10^6] A_p \qquad (5)$$

$$L_f = L - h_s \qquad (6)$$

$$\Delta p_t = \Delta p_s = \Delta p = \frac{\rho_l v_f^2}{2\xi^2} \qquad (7)$$

We can get the following formula from above equations:

$$L_f = \frac{(F_u - F_d) - 10^6 (\mathrm{P_t} - \mathrm{P_c}) \mathrm{A_p}}{\mathrm{A_p}\, \rho_l g} - \frac{10^6 v_f^2}{\xi^2 g} \qquad (8)$$

Which also can be expressed as the following equation :

$$L_f = \frac{\Delta W - 10^6 (\mathrm{P_t} - \mathrm{P_c}) \mathrm{A_p}}{\mathrm{A_p}\, \rho_l g} - \frac{10^6 v_f^2}{\xi^2 g} \qquad (9)$$

Where L is pump depth,m; ρ_l is the density of liquid in the well bore, g/cm^3 ; P_c is casing pressure, MPa ; ΔP_t is the resistance of travel valve , MPa ; P_t is the tubing pressure, ; ΔPs is the resistance of affix valve, MPa ; A_p is the area of plunger, m^2 ; h_s is the distance from pump depth to dynamic liquid depth, m ; v_f is the velocity when the liquid flow through the valve, m/s ; L_f is the dynamic liquid depth, m ; ξ is the coefficient of valve flow rate, which is the function of valve diameter, viscosity and flow rate; ΔW is the loading difference between bottom dead center and top dead center of pump dynamometer card.

2.3 Changing rule of the submergence depth

(1) Decline law of the submergence depth

The submergence depth means the depth of pump in the well bore, which equals the value of pump depth minus the dynamic liquid depth. The pumping unit can start working, when the dynamic liquid depth of well annulus arrives a certain position. At this time, the dynamic liquid depth, submergence depth and the liquid in the pump is high. So, when pump starts sucking liquid, the decline rate is fast. When the submergence depth decline a certain level, the liquid in the pump is becoming less and less, the coefficient of fullness of pump is start decreasing, until it arrives a certain value.

（2）Increasing law of the submergence depth

During the shut-in period, because of pressure difference between layer and bottom hole, the fluid flow into the bottom of the well, and the fluid in the annulus becomes higher and higher, which means the submergence depth improves[14]. The higher of dynamic fluid depth , the higher of bottom hole flowing pressure, and corresponding to the less pressure difference between layer and bottom hole, which leads to less fluid flow into bottom of the well. In this period, the liquid in the annulus rises slowly, and the submergence also varies slowly. It turns out that the longer shut-in time, the higher dynamic liquid level, the less cumulative production. For liquid shortage wells, the submergence first decline fast, then tend to a stable position.

2.4 Determination of open well time

According to the actual situation, we pick up the suit interval, test the electrical curve in every stable time, turn to the submergence depth, and draw the submergence decline curve. We can get the slope of curve in every interval, if the interval less than the certain value, then shut-in the well, and record the working time T_1.

Detail: we pick up N points, and record the two adjacent points coordinates, then get the slope. If the slop is small than a certain value, then shut-in the well, the mathematics equation is $\left|\frac{h_2 - h_1}{t_2 - t_1}\right| \le \varepsilon_1$. The open point is this point, record as T_1. The

determination of ε_1 can be gotten from the truth condition or former experience.

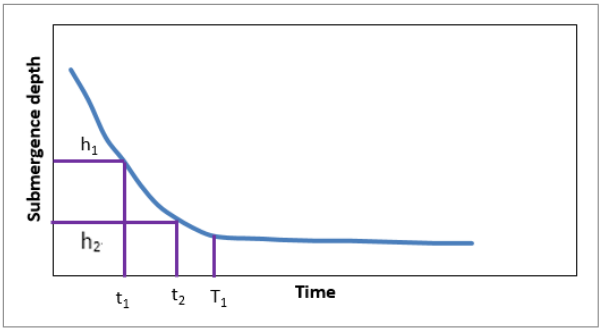

Figure 3. *Curve of submergence descent*

2.5 Determination of shut-in time

We can get the liquid depth backup law from the bottom hole inflow performance. There are three-phase in the late production period, which is oil, gas and water, so we use Petrobras way to get the production equation.

$$dp_{wf} = \rho g dh \tag{10}$$

$$dh = \frac{Qdt}{s} \tag{11}$$

We can get the following equation from the above equations:

$$\frac{dp_{wf}}{Q} = \frac{\rho g}{s} dt \tag{12}$$

Besides:

$$q_{oil} = q_b + (q_{omax} - q_b)[1 - 0.2(\frac{p_{wf}}{p_b}) - 0.8(\frac{p_{wf}}{p_b})^2] \tag{13}$$

$$J_1 = \frac{q_b}{p_r - p_b} \tag{14}$$

$$q_{water} = J_1(p_r - p_{wf}) \tag{15}$$

$$Q = (1 - f_w) q_{oil} + f_w q_{water} \tag{16}$$

Finally we get the follow equation from the above five equation

$$-Bdt = \frac{dp_{wf}}{Wp_{wf}^2 + Yp_{wf} + Z} \tag{17}$$

Where

$$B = \frac{\rho g}{s}$$

$$W = \frac{0.8(1 - f_w)(q_{omax} - q_b)}{p_r^2}$$

$$Y = \frac{0.2(1 - f_w)(q_{omax} - q_b)}{p_r} + f_w \frac{q_b}{p_r - p_b}$$

$$Z = -[(1 - f_w) q_b + f_w \frac{q_b}{p_r - p_b} p_r]$$

And then

$$p_{wf} = \frac{\frac{2M}{1 + e^{-M(Bt + C)}} - Y - M}{2W} \tag{18}$$

$$M = \sqrt{Y^2 - 4WZ}$$

The C in the equation can be gotten when the t=0 and the corresponding submergence depth in the shut-in time.

Therefore, the relationship between submergence and time is as follows:

$$H = \frac{p_{wf}}{\rho g} + H_{pump} - H_0 \tag{19}$$

$$H = \frac{\frac{2M}{1 + e^{-M(Bt + C)}} - Y - M}{2W\rho g} + H_{pump} - H_0 \tag{20}$$

$$M = \sqrt{Y^2 - 4WZ}$$

Where B,M,W,Y,Z is inter variation, which have no physical meanings; H is the submergence depth; h is dynamic liquid value; H_{pump} is pump value; H_0 is the middle depth of formation.

According to the submergence backup curve, we pick up N points, record the two adjacent point coordinates, and get the slope of two points, if the slop less than a certain value, then shut-in the well. The mathematics equation is $\left|\frac{h_3 - h_4}{t_3 - t_4}\right| \le \varepsilon_2$. The shut-in point is this point, record as T_2. The determination of ε_2 can be gotten from the truth condition or former experience.

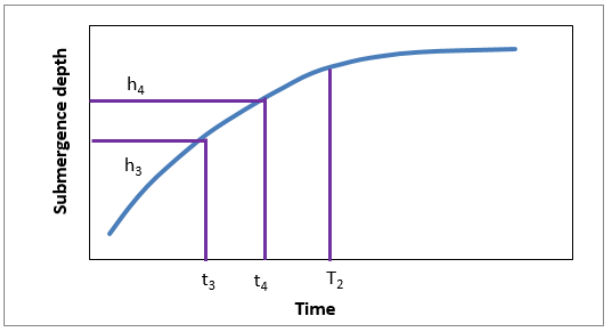

Figure 4. *Curve of submergence rising*

3. Conclusion

We studied the intermittent system for liquid shortage wells, and realized the importance of intermittent for oil operation. We also studied the variation law of annulus dynamic liquid depth, and got the ground dynamometer card from electrical power curve, finally solved the open and shut-in time. We conclude several conclusions, which are as follows:

(1) By using the relationship between electrical power, torque and loading, we draw the dynamometer card from electrical power curve, which can calculate the dynamic liquid depth.
(2) During the open and shut-in period, both of the decrease and rise speed of submergence depth are first quick back slow, the inflection point can determine the open and shut-in time.
(3) The determination of shut-in time can be solved by the mathematics relationship between inflow performance and submergence variation law.

Nomenclature

E is torque of crankshaft, N.m;
N_r is motor power, KW;
n_m is motor revolution, r/min;
η is driving efficiency;
I is driving ratio;
R is balancing radius, which represents the distance from the core of crank balancer to crank shaft, m;
P is the loading of suspension center, kN;
a,b is the length of before and after beam arm, m;
c is distance from the core of beam balancer to beam pivot,m;
W_b is the weight of beam, kN;
W_c'is the balance weight of crank radius after converting;
a_A is the acceleration of suspension center,
θ is the beam angel ,which is started from the horizontal position;
β is the angel between after arm of beam and pitman.
L is pump depth,m;
ρ_l is the density of liquid in the well bore, g/cm^3 ;
P_c is casing pressure, MPa ;
ΔP_t is the resistance of travel valve , MPa ;
P_t is the tubing pressure,MPa ;
ΔPs is the resistance of affix valve, MPa ;
A_p is the area of plunger, m^2 ;
h_s is the distance from pump depth to dynamic liquid depth, m ;
v_f is the velocity when the liquid flow through the valve, m/s ;
L_f is the dynamic liquid depth, m ;
ξ is the coefficient of valve flow rate, which is the function of valve diameter, viscosity and flow rate;
ΔW is the loading difference between bottom dead center and top dead center of pump dynamometer card
B,M,W,Y,Z is inter variation, which have no physical meanings;
H is the submergence depth;
h is dynamic liquid value;
H_{pump} is pump value;
H_0 is the middle depth of formation.

Acknowledgement

Authors thanks to China University of Petroleum Beijing agree to publish the paper.

References

[1]. Zhang qi.2006. Oil Production engineering. Petroleum industry press.100-108
[2]. Cui zhenhua, Yu guoan, An jingao et al.1992. Sucker rod pumping system. Petroleum industry press.301-305
[3]. Jiang yan, Zhang jiayou, Wang zhaohui et al. 2005.The Study and Application of Intermittent for Oil Wells. Inner Mongolia Petrochemical Industry. (05) 172-173
[4]. Zhang maiyun, Bai xuedong, Yao yanfang et al.2005.Method For Intermittent Production System In Low Production Well. Drilling & Production Technology. 28(03)68-70
[5]. Lei qun, Zhao weiguo.2001. A Study on Interval

Pumping Technique in Stripper Well. Drilling & Production technology. 24(02)28-29

[6]. Yu xiaoming, He guanzhong Jin yinglan.2006. Study on Rationality of Intermittent Pumping System for Pumping Well. Petroleum Geology & Oilfield Development in Daqing. 25(04):78-79

[7]. Guan ning, Ouyang huazhang, Li hua.2006. Pumping Well Liquid Producing Changing Rule Between Pumping Unit is Inefficient. Oil and Gas Field Surface Engineering. 25(02): 17-18

[8]. Zhou daiyu. Liang zheng.2003. A New Approach for Determining the Reasonable Intermittent Pumping Period for Low Efficiency Well. Drilling & Production technology. 26(01):52-55

[9]. Liu haitao. 2006. The Determination of Intermittent Production System for Low Production Wells. Chinese Technology Information（04）：45-47

[10]. Yan qingyu. 2004. The study of intermittent cycle for intermittent wells. Small Oil field. (02):32-35

[11]. Meng xiaoling, Zhang hongbo. 2006 Quantitative optimization of the intermittent production of low producing oil wells and its applications. Journal of Xi'an Shiyou University (Natural Science Edition). 21(04)64-68

[12]. MARSH H. Deep-well Pumping in California. SPE Journal. 1928:15

[13]. M.Cimic. 2006. Data Acquisition in Pumping Wells. SPE101846. 3

[14]. Xiang yuzhang, Liang guangjiang. 2004. Development and Application of Pump- Off Controlling in the Swabbing Well. Oil Drilling& Production Technology. 26(06):68-70

International Journal of Computational and Experimental Science and ENgineering (IJCESEN)
Vol. 6-No.2 (2020) pp. 88-91
http://dergipark.org.tr/en/pub/ijcesen

ISSN: 2149-9144

Research Article

Microstructure & Tribological Performance of Alumina-3wt% Titania Coatings Produced by APS

Mokhtar DJENDEL[1,2*], Omar ALLAOUI[2], Mourad MAAZOUZ[3],Rabah BOUBAAYA[1,2]

[1] Department of Science and Technics, Faculty of Technology, University of Bordj Bou Arreridj, Algeria
[2] Process Engineering Laboratory, University of Laghouat, BP 37G, Laghouat, Algeria.
[3] Departement of Mechanical Engineering, Faculty of Technologies, University of M'Sila, BP 166, M'Sila, Algeria

* **Corresponding Author** : m.djendel@lagh-univ.dz or djendelm@gmail.com
ORCID: 0000-0002-8175-6744

Article Info:

DOI: 10.22399/ijcesen.665097
Received : 26 December 2019
Accepted : 14 May 2020

Keywords

Plasma spray
Alumina–3wt.% Titania Coatings
Microstructure
XRD, SEM
Wear behavior.

Abstract:

Al_2O_3-3wt%TiO_2 coatings were deposited by atmospheric plasma spraying (APS). The microstructure and phase composition of the coatings were characterized by X-ray diffraction (XRD) and scanning electron microscopy (SEM). The wear and friction properties of Alumina–3wt.% titania coatings against a steel ball under dry friction conditions were examined. The microstructure result and the phase of the spray coating is analyzed and presented. In addition, wear behavior of the sprayed coating are evaluated for final coating performance. , test results showed that increasing some process parameters increased the performance of mechanical properties of coating and gave the lowest friction coefficient value of coating.

1. Introduction

Plasma-sprayed ceramic coatings such as Al_2O_3–TiO_2 coatings have been widely applied to structural materials and various machine parts in order to improve resistances to wear, corrosion, oxidization, erosion, and heat [1,2,3]. Plasma Thermal spraying techniques are coating processes in which melted or heated materials are sprayed onto a surface. Thermal spray coatings have a wide range of applications, for instance, by repairing machine parts damaged in service or by the production of parts with high wear resistance [4,5,6]. The Atmospheric Plasma Spraying (APS) is one of these processes. Plasma sprayed alumina–titania ceramic is one of the materials largely used in the APS process [7]. It is known for its wear, corrosion, and erosion resistance applications. In order to advance understanding the relationships between the microstructure and wear resistance of the plasma-sprayed coatings, an Al_2O_3-3wt% TiO_2 coating was prepared by plasma spraying and its tribological behaviors against a steel ball under dry conditions was examined.

2. Experimental procedure

2.1. Materials & coating deposition

An atmospheric plasma spraying system (Sulzer-Metco 9MC equipment) was used to deposit the Al_2O_3-3%wt TiO_2 coatings. Using two powder feeder containers, the powders were sprayed in sequence, by following (Ni-20wt%Cr)6Al powders as a bond coat and finally Al_2O_3-3%wtTiO_2 powder with particle size of -45+15µm as a top coating. In the spraying process, three passes were sprayed for (Ni-20%wtCr)6Al and 8 passes for Al_2O_3-3%wtTiO_2 coating. After coating, the samples were cooled in room temperature in order to avoid internal stress occurred to the coating. Finally, the samples were collected for analysis. Plasma primary and auxiliary gases were Ar and H_2: N_2 was used as carrier gas. The substrates were stainless steel and prior to the plasma spraying, were degreased and grit blasted. The substrate was grit-blasted with corundum at a pressure of 3.2 bar and cleaned using ethanol in order to remove remaining dust or grease from the surface.

During the process, the material to be deposited is injected in powder form using argon as carrier gas. The main spraying parameters are listed in Table 1.

Table 1. *Plasma spraying conditions*

APS Parameters	Bond Coat	Powder Coating
Arc Current, A	600	650
Arc Voltage, V	60	50
Primary gas (Argon) flow rate	25	80 lpm
Secondary gas (He) flow rate	45	50 lpm
Powder carrier gas (Ar) flow rate	90	30 lpm
Powder flow rate	20	20 gpm
Spray distance	100	100 mm
Passes, layer	3	8
Spray angle, °	90°	90°

Table 2. *chemical composition of AISI 304*

Elements	C	Si	Mn	P	S	Cr	Ni	Co	Cu	Fe
% wt	0.032	0.75	2.00	0.045	0.030	17.5/19.5	8.0-10.5	0.122	0.375	Bal

2.2. Coating Characterization

The phase and microstructure analysis of the coating samples were measured using XRD Machine and Scanning Electron Microscopy (SEM). The wear tests were carried out on a sliding, reciprocating and vibrating test machine (SRV). The wear test mode is the reciprocal motion of a steel ball against a disc, as illustrated in Fig.1. The upper ball specimen bearing a normal load vibrates against the lower stationary disc specimen. The wear tests were performed under four applied loads (20, 40, 60 and 80 N), with a slip amplitude of 1.4 mm, a frequency of 30 Hz and a period of 20 min. For all wear experiments, the samples were unlubricated; the tests were conducted at an ambient temperature of 10oC and relative humidity of 60 ~ 70 %. The ball specimens were composed of steel with a diameter of 10 mm and the disc specimen were Al_2O_3-3wt% TiO_2 coated steel substrates with dimensions of 20x20x5 mm.

3. Results & Discussion

3.1. Morphology and structure

The samples with different setting parameters were observed for the coating morphology. Fig.2 shows an example of morphology of coated samples of coating surface. The coating features observe the molten particles condition and spread as out on top of the surface to develop coating layers. Some areas on the surface appear as semi-molten particles and they agglomerate together with molten particle to

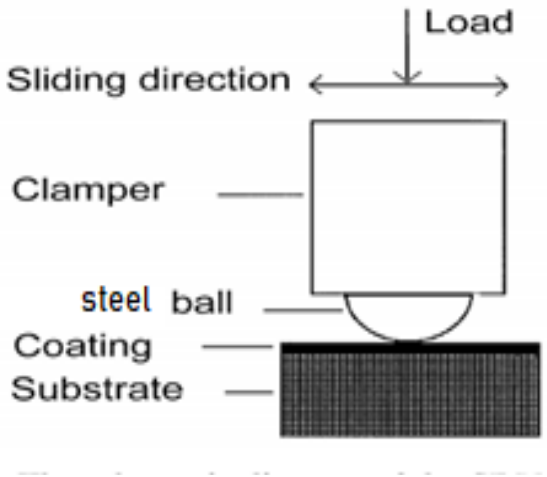

Figure 1. *The schematic diagram of the SRV tester.*

form coating layers [2,8,9]. The semi-molten particles exhibit pinholes, which are characteristic of porosity, occurred on the coated sample. The occurred porosity also may be due to the lamellae structure, which exhibit molten and semi-molten particles and will create pinholes inside the coating. The porosity may occur due to absorbed gases during spraying process. In this study, it is identified that the average porosity of the coating samples are 8.1%. Less porosity will produce better structure and bonding between the individual layers of coating. It also results in increase of density, hardness, adhesion strength and wear resistance of the coating [10,11].

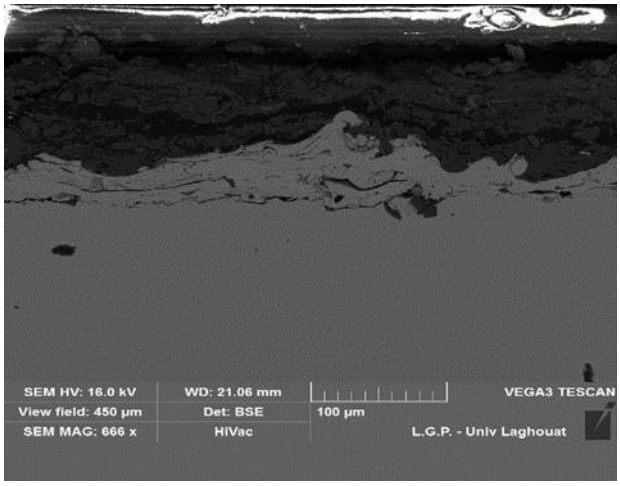

Figure 2. *The morphology of coating surface scanning with SEM at magnification 100µm.*

Referring to the coating cross-section samples, three different phases are observed. These are the Al_2O_3-3wt%TiO_2 coating (top coating), Ni-20wt%Cr6Al coating (bond coating) and metal substrate, which is shown in Fig.3.

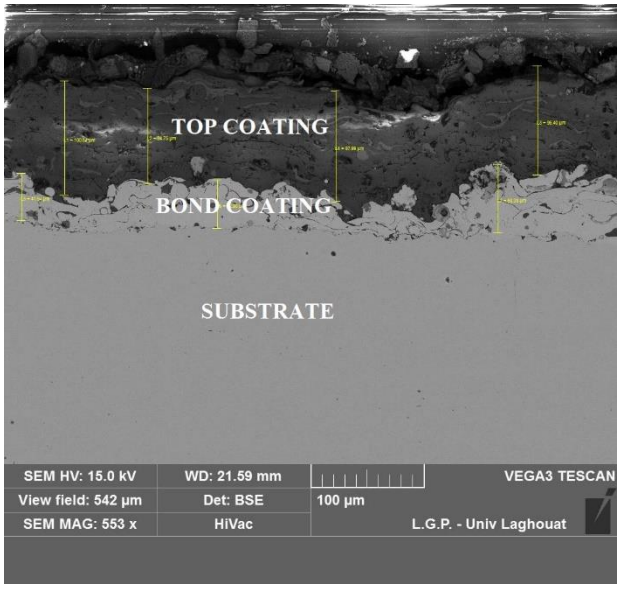

Figure 3. *SEM micrographs of Al_2O_3-3wt.%TiO_2 coating at magnification 200µm.*

When the molten particle of Al_2O_3-3wt%TiO_2 impacted the substrate, it spreads and solidifies rapidly and formed a coating. The bonding effect of particles in forming a coating is due to mechanical interlocking, chemical reaction and partial fusion of the contact surface and will lead to mechanical adherence.

As shown in Fig.4, all Al_2O_3-3wt%TiO_2 coating predominately contains γ-Al_2O_3 (Gamma alumina) coexisting with α-Al_2O_3. In view of the nucleation kinetics, under-cooling of the α-Al_2O_3 phase, resulting liquid droplets led to the nucleation of γ-Al_2O_3 nucleated rather than of α-Al_2O_3. This occurs because of lower interfacial energy between crystal and liquid [12]. Cooling rate after solidification was rapid enough to prevent subsequent transformation to α-Al_2O_3. The presence of α-Al_2O_3 in the Al_2O_3-3wt%TiO_2 coating is due to the incorporation of unmelted particles during coating process [10,11].

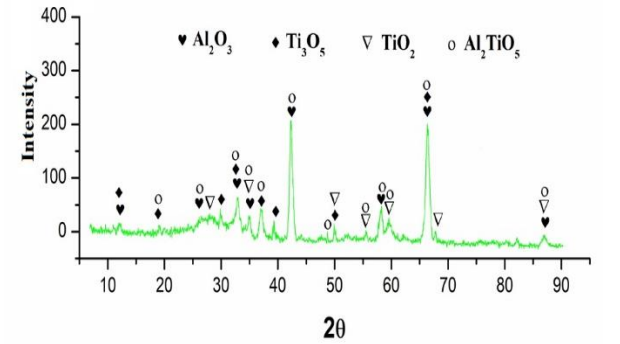

Figure 4. *Typical Photo Of The XRD Patterns.*

3.2. Wear and Friction

Fig.5 show the effect of contact load on the wear rate of the nanostructured Al_2O_3-3wt%TiO_2 coatings. The wear rate of the samples was lowest at 20N and gradually increased with increasing load. The improved wear resistance of the coating was attributed to the increase of toughness and cohesion strength between splats [12,13].

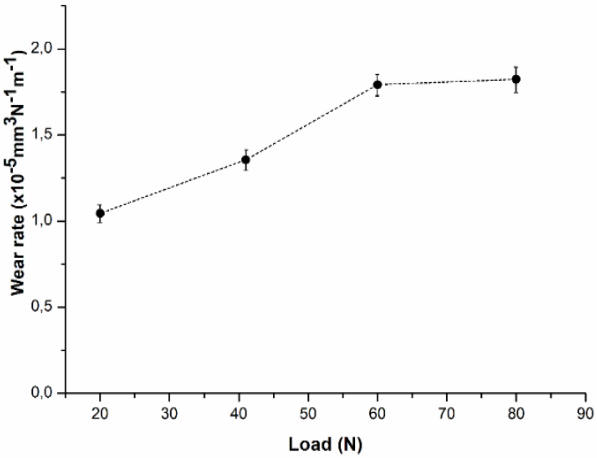

Figure 5. *Wear rates of the sprayed Al_2O_3-3wt% TiO_2. coatings sliding against steel ball*

Fig.6 shows the steady-state friction coefficients of the nanostructured and conventional Al_2O_3-3wt% TiO_2 coatings against a steel ball under dry sliding conditions. The results showed that the friction coefficients of coatings were similar at all test loads and exhibited no great change with increasing contact load under unlubricated conditions. The friction coefficients of the Al_2O_3-3wt.%TiO_2 coatings were similar and about 0.51.

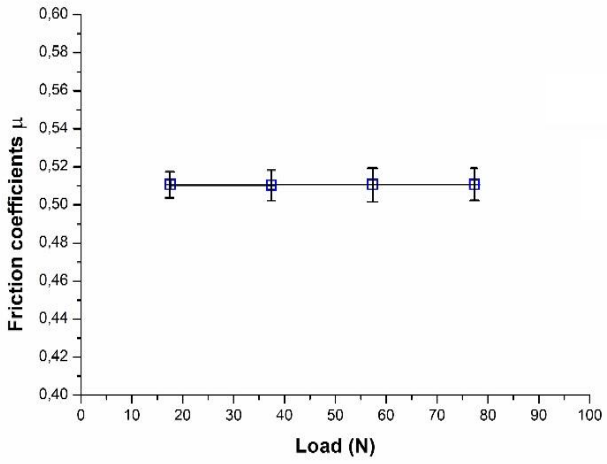

Figure 6. *Friction coefficient of Al_2O_3-3wt% TiO_2 coatings sliding against steel ball.*

4. Conclusions

Al_2O_3-3wt.%TiO_2 coatings were deposited by atmospheric plasma spraying. Microstructure and phase properties of the as-sprayed coatings were characterized.

The difference in microstructure and properties of the coatings led to different tribological behaviours.

The Al_2O_3-3wt.% TiO_2 coatings contained both equiaxed α-Al_2O_3 and γ-Al_2O_3. Moreover, the coating possessed a more homogeneous microstructure and TiO_2 phases is rutile in this coating, which is due to the reaction between TiO_2 and Al_2O_3 particles during plasma spraying.

In addition, the coating possessed an improved wear resistance; it was gradually increased with increasing load. Although the friction coefficient exhibited no variation with increasing contact load.

Acknowledgement

Authors gratefully thank Professor İskender Akkurt and other staff members of ICCESEN 2019 for the best organization.

We gratefully thank Professor Omar Alaoui for his support, his useful and very important comments and for providing facilities in Process Engineering Laboratory, University of Laghouat for this study.

References

[1] L. Pawlowsky, The Science and Engineering of Thermal Spray Coatings, John Wiley & Sons, New York, 1995.

[2] P. Fauchais, A. Vardelle, B. Dussoubs, in: Thermal Spray 2001: New Surfaces for a New Millennium, Eds. C.C. Berndt, K.A. Khor, E.F. Lugscheider, ASM International, Materials Park (OH) 2001, p. 1.

[3] M. Djendel, O. Allaoui, R. Boubaaya, Characterization of Alumina–Titania Coatings Produced by Atmospheric Plasma Spraying on 304 SS Steel. Acta Phys. Pol. A 132, 538 Vol. 132(2017),DOI: 10.12693/APhysPolA.132.538

[4] Günen, Ali. (2016). Micro-Abrasion Wear Behavior of Thermal-Spray-Coated Steel Tooth Drill Bits. Acta Physica Polonica A, DOI: 10.12693/APhysPolA.130.217

[5] H. Ageorges, P. Ctibor, Comparison of the structure and wear resistance of Al_2O_3–13wt.%TiO_2 coatings made by GSP and WSP plasma processwith two different powders, Surf. Coat. Technol. 202 (18) (2008) 4362–4368. DOI: 10.1016/j.surfcoat.2008.04.010

[6] L. Shaw, D. Goberman, M. Gell, S. Jiang, Y. Wang, T.D. Xiao, P. Strutt, The dependency of microstructure and properties of nanostructured coatings on plasma spray conditions, Surf. Coat. Technol. 130 (2000) 1–8. DOI: 10.1016/S0257-8972(00)00673-3

[7] E.H. Jordan, M. Gell, Y.H. Sohn, D. Goberman, L. Shaw, S. Jiang, M.Wang, T.D. Xiao, Y. Wang, P. Strutt, Fabrication and evaluation of plasma sprayed nanostructured Alumina–Titania coatings with superior properties, Mater. Sci. Eng. A301 (2001) 80–89,https://doi.org/10.1016/S0921-5093(00)01382-4

[8] İ.H. Karahan, Effect of Borax Pentahydrate Addition to Acid Bath on the Microstructure and Corrosion Resistance of Zn-Co Coating. Acta Phys. Pol. A Vol.128, B-432 (2015). DOI: 10.12693/APhysPolA.128.B-432

[9] Djeghdjough Mohamed, Bacha Nacer eddine and Dilmi Nacer, Effect of Substrate Preheating, Roughness and Particles Size on Splat Morphology of Thermal Sprayed Coatings. Proc. International Conference on Computational and Experimental Science and Engineering (IJCESEN) Vol. 1-No.1 pp. 16-18(2015).

[10] Rahim, M.S.A.,Hayati, S.N. and Bakir, H.L. (2009) 'Plasma spray ceramic coating and measurement of developed coating behaviour', Int. J. Precision Technology, Vol. 1, No. 2, pp.163–172. DOI: 10.1504/IJPTECH.2009.026375

[11] M. Djendel, O. Allaoui, Abderrazak Bouzid. Effect of Air Plasma Spraying Parameters on the Quality of Coating. Proc. International Journal of Computational and experimental Science and Engineering (IJCESEN) Vol.2 –No. 2 (2016)pp.1-5.

[12] Lin, X., Zeng, Y. and Ding, C.X. (2003) 'Microstructure of alumina -3wt.% titania coating by plasma spraying with nanostructure powders', Materials Science and Engineering, Vol.A.357,pp.228.234,https://doi.org/10.1016/S0955-2219(03) 00254-1

[13] Haghighatzadeh, Azadeh & Mazinani, Babak & abdolahpour salari, Maryam. (2017). Coating of Ordered Large-Pore Mesoporous Silica with TiO_2 Nanoparticles and Evaluation of Its Photocatalytic Activity. Acta Physica Polonica A. DOI: 10.12693/APhysPolA.132.420.

International Journal of Computational and Experimental Science and ENgineering (IJCESEN)
Vol. 6-No.2 (2020) pp. 92-97
http://dergipark.org.tr/en/pub/ijcesen

ISSN: 2149-9144

Research Article

Shale Gas Technical Development and Innovation

Xingyuan LIANG[1*], Ji HU[2], Qishuang ZHOU[2], Lei DU[2], Qiang LI[3], Baofeng LI[4], Yuan CHENG[4]

[1]China University of Petroleum at Beijing, 102249,Beijing-China
[2]Xuanhan Gas Production Area northeast Sichuan Oil and Gas district, CNPC Southwest Oil and Gas Field Company, 635000,Dazhou-China;
[3]CNPC Xibu Drilling Engineering Company Limited, 834000,Karamay-China;
[4]CNPC Xingjiang Oilfield, 834000,Karamay-China

* **Corresponding Author** : lxypetro@163.com
ORCID: 0000-0002-7583-3969

Article Info:

DOI: 10.22399/ijcesen.692724
Received : 25 February 2020
Accepted : 14 May 2020

Keywords

Hydraulic fracturing
Volume fracturing
Horizental well

Abstract:

The classical theory of geology believe that shale reservoir physical property is poor, the oil and gas could not be saved, or only as source rock cover, almost have no exploitation value. Later people found that shale belongs to in-situ large area continuous reservoirs, and put forward a series of shale gas development technology. In this paper, we base on time sequence and shale gas production, study the transition of the shale gas geology theory and shale gas development technology advances, analyzing the important role of technological innovation, in order to give some enlightenment to the development of shale gas development technology.

1.Introduction

In 1821, the first bite of shale gas is used in street lamp lighting in the United States, which is the beginnings of the U.S. natural gas development[1,2]. Then shale gas is known by people gradually. Through untiring efforts, the development and production of shale gas has finally entered the stage of rapid development. 2005 ~ 2008, the United States of shale gas production increased at an annual rate of 10 billion, 2008 ~ 2011 years increased at an annual rate of 40 billion. By 2012, the U.S. shale gas production reaches 2653 x $10^8 m^3$, 853 x $10^8 m^3$ more than in 2011 (Fig. 1). From the perspective of the development of shale gas development technology, the transition of the shale geological theory and exploratory development technology progress is the key to the success of the shale gas.

1.1 The transition of the shale geological theory

The classical theory of geology believes that the valuable oil and gas reservoir must have three general conditions[1-4], which are source, reservoir and cap. Due to shale matrix porosity is less than 10%, permeability is less than 1 mD, namely poor reservoir physical property .Therefore, although a lot of oil and gas Wells in the drilling process encountered the dark shale section, organic matter is thought to be only produce air source of oil and gas layer, rather than a reservoir. For a long time, dark organic matter has been as hydrocarbon source rocks or shale cap-rock, only a few have crack shale as reservoir development. And the success of the North American commercial shale gas development, breaking the traditional geological theory. People found a lot of gas resources from shale, gradually realized the dark mud shale is not only a gas source rock, but also a reservoir and capping layer, is the typical of gas accumulation. The success of the shale gas development also makes people widened to find oil and gas fields. Traditional geological theory, the porosity and permeability of rock strata below a certain threshold value, it almost has no economic value. And the success of the shale gas mining, make a lot of gas density layers, which are previously discarded by conventional oil also has

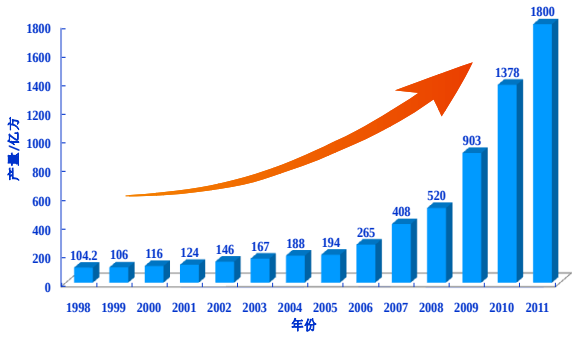

Fig. 1 *The calendar year American shale gas production*

the development value. Data show that new proved reserves in the proportion of low permeability reserves increased from about 30% to nearly 70%[5]. Horizontal Wells of low permeability reservoir and fracturing technology can get considerable exploration effect greatly.

In the past, people focused on gathered hydrocarbons, which is composed by large area dispersed gas through migration .And the good physical properties in trap formation is the key area of oil and gas development. Because the shale system's matrix porosity and permeability are both low, and it's nearly impossible to migrate the oil and gas. So people think that the amount of oil and gas in shale system should be very little. Later people found that there are a large number of nano-scale holes and gaps in shale, and clay minerals of plant-based ultrafine particles, which have large surface area and strong adsorption ability. Gas is adsorbed on clay surface and free in the micro pore. That is to say, the whole shale formations are reservoir. The discovery once again changed the traditional geological cognition, because the aim of the traditional prospecting theory is to find oil and gas gathering the limitation of the trap, and shale gas is a large area of continuous accumulation. In layman's terms, conventional natural gas storage in "point", and shale gas is stored in the "face"(Fig.2).

2 Innovation of shale gas exploration and development technology

On the basis of new geological theory knowledge, People emancipate the mind, change ideas, explore new technology to increase production of shale gas continuously.

2.1 Water fracturing

Before 1997, most people used gel fracturing technology at home and abroad, but he construction effect was bad. Because of high liquid rubber plug concentration, the damage to the reservoir, long operation period and high cost. Traditional fracturing theory considered that the cracks will be closed after fracturing, so people must use a lot of proppant for supporting, in order to prevent the crack closure. but due to the incomplete drainage and stratigraphic residues within a large amount of residue can affected the fracture diverting capacity, furthermore residue can damage formation, and reduce the development effect.

Later people found that[6]for high brittleness index, natural fracture development and scratchy crack shale gas reservoirs, water fracturing shearing force in the process of fracturing can make natural micro cracks in the shale gas reservoir slip, and cracks couldn't return to its original state after being stopped pump. Therefore, the cracks can keep a high permeability (Fig.2), at the same time ,also greatly reduce the amount of proppant and residual damage to the reservoir. In 1997, Mitchell energy company tried to use water in the Barnett shale instead of scraping gum fracturing, the result was very satisfactory. Water fracturing has increased Barnett shale ultimate recovery more than 20%, but also reduced the cost more than 60% of the work, the construction effect is significantly more than scraping gum fracturing technology.

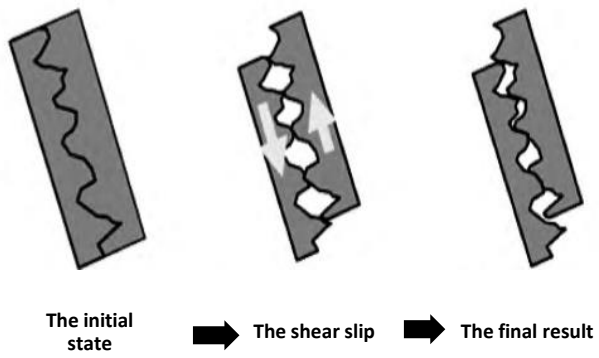

Fig. 2 *Shear slip mechanism*

Water Fracturing is a technology[7], which is adding surfactant and drag reduction agent in clean water as the working fluid fracturing operation. With only a small amount of proppant in work fluid, sometimes, sand amount according to the situation. Compared with the scraping gum fracturing, water fracturing has the following several advantages: ①Due to water fracturing does not require the preparation of gel cross linking agent and gelling agent, etc., thus it eliminats the gel hurt, doesn't contain residues, won't block formation and can accelerate the flow back process; ②Easy to form a certain diversion ability long cracks; ③Easy to extend the natural cracks or cracks formed interconnected network;④Reduces the transport and dosage of proppant, greatly reduces the operating costs, than with the size of

the gel fracturing operation cost reduced by 40% ~ 60%.

2.2 Bold attempt of horizontal well

Before the 21st century, the development of shale gas mining almost all adopted the way of a vertical Wells, but because of thin shale gas reservoir, reservoir physical property was poor, vertical Wells development had not been able to obtain high yield. In 1992, Mitchell Energy Company completed the first horizontal well in the Barnett shale, since then the application in the development of shale gas horizontal well was began. In 2002, Devon Energy Company in Barentt shale drilled a number of horizontal well; then the horizontal well technology scale expanded unceasingly. 2003 ~ 2007, the number of horizontal wells in Barnett is more than 4960, which is more than 50% of the total number of Barnett shale gas production Wells, in 2007 ,there was 2219 horizontal Wells, accounted for 94% of the year number of shale gas well completed. At present, horizontal Well has become the main development of shale gas, which greatly accelerated the development process of shale gas[8]. Fig. 3 is based on the well type Barnett shale gas production every year.

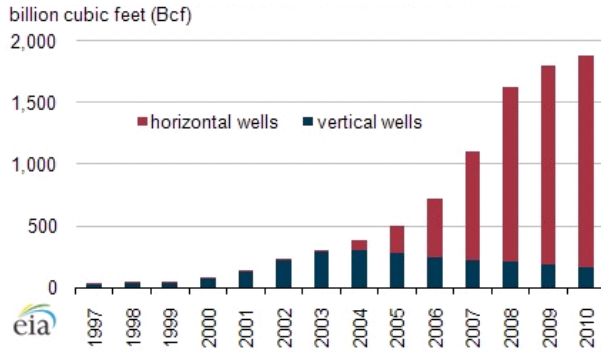

Fig. 3 *Horizontal Wells and vertical Wells shale gas output (from EIA)*

Compared with vertical Wells, the advantages of the horizontal Wells are as follows: ① horizontal well can cross the longer the length of the reservoir, and has bigger chance to fellowship with more cracks, furthermore, the single well production is 3 ~ 5 times of vertical Wells, the cost is 1 ~ 1.5 times of vertical Wells[9];②mining areas is bigger, can avoid the interference of ground disadvantage;③ vertical Wells can't get industrial hydrocarbon flow region, horizontal well development effect is very good;④the development cycle is longer.

2.3 The combination of the horizontal well staged fracturing

In the 1980 s[10], people began to use horizontal well fracturing technology for oil and gas, the first is the general fracturing, but the fracturing effect is not obvious ,which is because of the long horizontal section , multi-layers and lower surface pump pressure.

Later, people put forward a way, which is dividing the horizontal well into several segments by packer, and then fracturing step by step. In 2005[11], Newfield company of the United States adopted 5 ~ 7 sections of staged fracturing in parts of the Woodford shale, the shale gas single-well maximum initial yield reached 28.32 x 10^4 m^3 / d, the maximum yield of 16.99 x 10^4 m^3 / d. At present, 85% of the shale gas production Wells in the United States is using horizontal well and multi-stage fracturing technology combination of drilling, increases the yield significantly.

Horizontal well staged fracturing is that packer or bridge plug is used to change the horizontal section is divided into several small pieces, then step by step fracturing. Multistage fracturing can undertake targeted construction according to the characteristics of the reservoir, the target accurately. And the fracturing effect is remarkable. The emphasis and difficulty in multi-stage fracturing is the down hole completion tools of research and development. Both at home and abroad have been staged fracturing down hole tool of independent research and development and technical innovation. At present, the mainstream of the down hole tool has two types: one is the pitch sliding sleeve, the other is the rapid drillable bridge plug.

2.3.1 Pitching sliding sleeve

Baker hughes, in 2005,successfully developed pitch sliding sleeve multi-stage segmental fracturing technology[12], has successfully finished 40 segments. Pitching sliding sleeve multi-stage segmental fracturing technology use expandable casing packer and sliding, by closing one and multiple layers in a wellbore selectively into a number of different reservoirs, instead of using articulated tubing or coiled tubing to separate interval. In the fracturing fluid input, in turn, bigger diameter packer ball, can be the interval after fracturing packer, then go to the next layer fracturing, the continuous operation process, need not stop pumping fracturing fluid. The process pipe strings generally adopt the fixed string structure,

fracturing string and production string are together, and construction efficiency is higher.

Open hole packer and the sliding sleeve technology can give full play to the advantages of open hole[13], which expose more drainage period, short operation time, simple technology, which is a multistage horizontal well fracturing in the forefront of well completion technology, it can be in a vertical or horizontal well fracturing multiple interval and at the same time do not need to use the bridge plug space.

2.3.2 Drilling bridge plug

At present, many domestic and foreign companies adopt pumping bridge plug and staged fracturing perforating technology in this kind of well completion. Through the bridge plug the packer, the technology is presented. The perforating and fracturing, pressure with coiled tubing belt grinding shoes after a drilling bridge plug fluid side by side. Fast drilling bridge plug fracturing technology with unlimited block series, bridge plug pressure as high as 70 MPa, heat-resistant up to 150 ℃, the effective rate was 100%. The technology is suitable for large liquid volume, large displacement characteristics of shale gas fracturing, wellbore isolation high reliability, and quick construction. In addition, the pumping bridge plug and perforation pattern perforating the process using cluster, so more conducive to form a joint network.

Due to the bridge plug perforating technology [14], can in a short time after fracturing drill out all bridge plug, greatly save the construction time and cost, and also reduce the retention time of fracturing fluid in formation, reduce the liquid damage to reservoir. By means of this kind of perforating, each fracturing period of 4 ~ 6 cracks can be formed, stress interference between the cracks will be more apparent, fracturing after the completion of the formation of the joint network will be more complex. Transform the horizontal section is divided into multiple segments, after the completion ,they can form 8 to 15 paragraph of fracture clusters, transforming volume is bigger, the effect after fracturing operations is also more satisfied.

2.4 The application of factory fracturing

Traditional fracturing is decorated well and then fracturing, wells are often scattered. Shale gas fracturing need to use a lot of big crews take, and related supporting facilities, such as personnel, materials and pools, etc., at the same time many shale gas reservoir are extremely flat terrain. Traditional way of fracturing is fast for a certain area of a few Wells after completion of construction, then turn to the next block of several Wells to construction, the "hit a shot, in one place", which can lead to a long construction period, operation cost increases.

In 2005, Halliburton proposes the concept of "fracturing factory"[15,16], that is in a central region for hundreds of meters to thousands meters apart of fracturing Wells. All fracturing equipment layout in central region, do not need to move equipment, personnel and materials to multiple fracturing Wells. Later, this concept gradually expanded into a "factory" Well (Well Plant), namely the multi-port Well from drilling, perforation, fracturing and completion and production, the entire process is completed by a "central". Through "Well factory", completion cycle from 60 days to complete 1 Wells down to the present 20 days to complete 5 Wells, the completion cost was reduced by 60%.This construction method can generate more complex cracks, the average output by 21% ~ 25% higher than single fracturing, cost down more than 50%.

Factory fracturing technology is characterized by: ① high land utilization: deploy multiple location in a region, in every multi-port horizontal well site deployment. Each drill Wells usually 4 ~ 10 Wells, sometimes 12 ~ 16, up to more than 50; ② quick: drilling, cementing, perforating and fracturing operation which are mass, streamline, standardization, and achieve seamless connection between each working procedure;③ low cost: fluid recycling, relocation costs less; ④ form complex fracture fracturing, easy volume reconstruction;⑤ the ground utilization high infrastructure construction (public pools); ⑥ mass operation, reduce moving time, high work efficiency, the construction efficiency can be improved more than 1 times; ⑦ All landowners liquid concentration, facilitate processing and recycling, every 3 Wells can save water of the well.

2.5 Innovation of Synchronous/Zipper fracturing

Fracturing cracks of press out as much as possible, is the purpose of improving fracture diverting capacity, so as to reduce the resistance of hydrocarbon migration. In order to be able to press out more cracks, people developed synchronous/zipper fracturing technology. In 2006[17], synchronous fracturing technique for the first time in the Barnett shale, operators within the range of 152 ~ 305 m apart on two parallel

horizontal well fracturing at the same time. After operation, 2 Wells are all manufactured with fairly high speed, with nissan 25.5 x 1 well among them a rate of 10^4 m^3 continual production for 30 days, and the other without fracturing Wells nissan speed between 5.66 x 10^4 ~ 14.16 x 10^4 m^3.At present, the commonly used in synchronous fracturing has become in the Barnett shale development of hydraulic fracturing technology.

Synchronous Fracturing refers to two or more adjacent parallel Wells Fracturing at the same time[13]. In the process of fracturing, the fracturing fluid and proppant at high pressure from a well to the other well migration distance is the shortest way, to increase the fracture surface area of the grid and density, advantage between Wells and well connected to increase the degree and intensity of the workspace cracks, thus the rapid increase of shale gas well production. If the limited space can't for multi-port well Fracturing at the same time, people put forward the "Zipper Fracturing".

Synchronous fracturing and Zipper Fracturing comparing with ordinal fracturing[11,17,18], maximize the fracture fracturing Wells have been achieved, the yield increased by 20% ~ 55%, and small environmental impacts of the workspace, low cost and fast completion, and started to return time is short. Originally two close to each other and depth of roughly the same between the horizontal well fracturing at the same time, now the technology has developed into three or even four Wells fracturing at the same time.

2.6 The concept of "volume fracturing" is put forward

Due to the reservoir conditions, injection-production well spacing, fracturing process and so on, a single increase length to increase production of ultra-low permeability reservoir and the effect is not obvious, the conventional fracturing modification is difficult to achive commercial exploitation of the oil and gas reservoirs, so we must explore new fracturing technology.

In 2006, M.J.Mayerhofer et al. first mentioned the "Stimulated Reservoir Volume" the SRV) concept [19]. The principle of Volume fracturing is that in the process of hydraulic fracturing, the natural crack expanding and brittle rock shear sliding, the mutual interactions form the natural and artificial cracks fracture network, thus increasing volume, improve the initial production and ultimate recovery. Operators fractured 19 Wells in Barnett, fracturing volume is 5.3 x 10^6 ~ 52.7 x 10^6 m^3, and the production is bigger and bigger as the volume increasing[20].

The concept of "volume fracturing" overturn the classic theory of fracturing, volume reconstruction of form is no longer wings symmetry, but a complex network fracture system, crack fracture with the extension not only is the destruction of tensile fracture, but also is a cut, sliding, such as fault section of complex mechanical behavior. Volume fracturing technology is the most representative in the Barnett shale gas development in the United States.

3 Summary

The effective development of America's shale gas changed the pattern of world energy. The success of the shale gas exploration and development is the transformation of shale geological theory and engineering technology innovation results. According to the development of shale gas mining technology, people should realize the importance of theoretical innovation and technological innovation.

(1) Through geological theory innovation, people find the commercial value of natural gas, from the poor physical properties of shale, and expanded the oil and gas fields.

(2) In view of the high brittleness index, natural fracture development and scratchy crack shale gas reservoir, people developed water fracturing technology, and replaced the crosslinked gel fracturing technology, reducing reservoir damage, and increases the fracture diverting capacity.

(3) Because of the shale reservoir physical property is poor, a vertical Wells are unable to get high yield, people successfully used horizontal well to drill the reservoir.

(4) Because of the horizontal well length is longer, the fracturing effect is poorer, people developed staged fracturing technology, and developed a pitching sliding sleeve and fast drilling down hole completion tools ,such as bridge plug, to improve the shale gas production, simplifies the construction.

(5) Aiming at the problem of limited space, the cost is too high, people worked out the "factory" well fracturing technology, greatly reduce the cost, operation time, and increase the production.

(6) In order to fracturing more cracks, worked out the synchronous fracturing and zipper

fracturing technology, cause the fracturing well fracture to maximize, improved fracture diverting capacity.

(7) For wings symmetric seam output effect is not obvious, people put forward the concept of "volume fracturing", make the yield increase after modification, and subvert the traditional theory of fracturing.

Acknowledgement

Authors thank China University of Petrleum Beijing permit to publish the paper.

Reference

[1] LI Zongtian. SU Jianzheng. ZHANG Rusheng. Modern Fracturing Technology of Horizontal Well in Shale[M]. China Petrochemical Press.2016

[2]XIAO Gang ,TANG Ying .Shale gas exploration and development technology[M]. Higher education press.2012

[3] LIU Guang-di . Petroleum geology [M]. Petroleum industry press, 2009.

[4] ZHANG Kang. The shale gas revolution to rewrite the traditional theory of oil and gas geological exploration [J]. China petrochemical. 2013 (01) : 21-23.

[5] LI Zong-tian , LI Feng-xia , HUANG Zhi-wen . The key role of hydraulic fracturing in oil and gas field exploration and development [J]. Journal of oil and gas geology and oil recovery. 2010 (5) : 76-79.

[6] LI Xiao-gang, SU Zhou, YANG Zhao-zhong, etc. Shale gas reservoir volume net seam fracturing technology progress [J]. Journal of oil and gas. 2014 (7) : 154-159.

[7] WANG Su-bing. Water fracturing technology review [J]. Journal of natural gas exploration and development. 2005 (04) : 39-42.

[8] Kent A Bowker，George Moretti，Lee Utley. Fayetteville Maturing[R]. Oil and Gas Invester. 2007,Jan.:14-17.

[9] ZhANG Wei-dong, GUO Min, YANG Yan-hui. Shale gas drilling technology review [J]. Chinese and foreign sources of energy. 2010 (6) : 35-40.

[10] XU Dong-jin, YOU Yan-rong, WANG Sheng-liang etc. Dense reservoir horizontal well staged fracturing technology status and progress [J]. Chinese and foreign sources of energy. 2013 (4) : 36-41.

[11] ZHANG Ran, LI Gen-sheng, Yang Ling. Shale gas production technology present situation and prospect [J]. Journal of petroleum machinery. 2011 (S1) : 117-120.

[12] LI Shao-ming, WANG Hui, DENG Han etc. Horizontal well staged fracturing technology review [J]. Journal of China petroleum and chemical industry. 2013 (10) : 56-59.

[13] TANG Ying ,TANG Xuan, WANG Guang-yuan etc. Shale gas development of hydraulic fracturing technology review [J]. Geological report. 2011 (Z1) : 393-399.

[14] XUE Cheng-jin . Shale gas fracturing technology present situation and development Suggestions [J]. Oil drilling technology. 2011 (3) : 24-29.

[15] ZHANG Huan-zhi, HE Yan-qing, LIU Jia, etc. Present situation and the trend of development of the horizontal well staged fracturing technology abroad [J]. Journal of petroleum science and technology BBS. 2012 (6) : 47-52.

[16] WU Qi, XU Yun, LIU Yuzhang. U.S. shale gas volume reconstruction technology present situation and the enlightenment to our country [J]. Oil drilling technology. 2011 (02) : 1-7.

[17] Gary W，Schein，Stephanie Weiss. Simultaneous fracturing takes off：enormous multiwell fracs maxmize exposure to shale reservoirs ， achieving more production sooner[J]. E&P. 2008:81(3):55-58

[18] ZENG Fan-hui , GUO Jian-chun, LIU Heng, etc. The north American shale gas effective fracturing experience and enlightenment to China [J]. Journal of southwest petroleum university (natural science edition), 2013 (6) : 90-98.

[19]S.C.Maxwell，C.K.Waltman，N.R.Warpinski，etal.Imaging Seismic Deformation Induced by Hydraulic Fracture Complexity.[C].SPE102801，2010.

[20] ZUO Chen ,XUE Cheng-jin , JIANG Ting-xue , etc. The application of the volume of shale gas well fracturing technology in our country suggested [J]. Journal of natural gas industry. 2010 (10) : 30-32.

International Journal of Computational and Experimental Science and ENgineering (IJCESEN)
Vol. 6-No.2 (2020) pp. 98-101
http://dergipark.org.tr/en/pub/ijcesen

ISSN: 2149-9144

Research Article

Thermodynamics of the Quark Gluon Plasma in the Early Universe

Hamid ALZAKI*

Suleyman Demirel University, Science and Arts Faculty, Physics Department, 32200, Isparta-Turkey

* **Corresponding Author** : alshamary632000@yahoo.com
ORCID: 0000-0002-1142-8614

Article Info:

DOI: 10.22399/ijcesen.686962
Received : 09 February 2020
Accepted : 11 June 2020

Keywords:
Quark gluon plasma
Early Universe
Equation of states

Abstract:

The recent progress in collider experiments provides us with valuable information to understand the properties of the quark-gluon plasma. In this study, we provide the analytical solution to the differential equation of the time evolution of the temperature in the early Universe in the MIT bag model for gluons only. We discuss the equation of state of a QGP in a particular model, the possible signs for a plasma created in heavy-ion collisions and provide analytic solutions describing the time evolution of the energy density, temperature and pressure of this plasma in the early universe.

1. Introduction

The early Universe during the first 10 microsecond after the big bang was filled with soup of quarks and gluons, in other word Quark gluon plasma is a state of matter with the highest energy level in which the elementary particles that make up the hadrons of baryonic matter are free and are not affected by strong interactions between them under extremely high energy densities (with temperature higher than 150 MeV) [1]. Quarks, the subatomic particles carrying a fractional electric charge and one of two basic components of matter in the theory of standard model of particle physics. Gluons, the massless particles that "carry" the force between quarks, they are the particles that quarks exchange as they interact, or, in the language of modern physics, they mediate the strong force between quarks, that compose baryonic matter [2]. The conception, of the state of the quark gluon plasma have been improved and evolved by experimentally and theoretically studies. Experimentally by using colliders, through the relativistic heavy-ion collision experiments at Brook-haven National Laboratory in the United States of America and European Nuclear Council, Geneva in Switzerland. Theoretically, from the numerical simulation of finite temperature quantum chromo-dynamics on a lattice [3]. The new results obtained by som work about the nature of the QGP motivate them to achieve their logical results in the early Universe. This could be done through solving the Fried-mann equations, which allow them to determine the exact temporal development of thermodynamic quantities at the beginning of the universe. So we see that the study of quark matter is very important to understand the nature of universe which gave me an incentive to research in this field. The Quark Gluon Plasma was first proposed by Collins and Perry and others in the 1970s. Their arguments are based on the principle of asymptotic freedom in Quantum dynamics (QCD) is the widely accepted theory in the world that describing the strong interactions of quarks, gluons and nucleons [4]. It is the strongest comparison with other interactions and for example, the gravitational force is $\sim 10^{-39}$, the weak interaction is $\sim 1/137$ and the strong interaction is ~ 1. It is known through studies in the field of cosmology, the Universe is homogeneous and isotropic. Such characteristics indicate that the Fried-mann Robertson-Walker metric will parameterize the space-time, which has been introduced into the Einstein equations to provide the Fried-mann equations. So, of these latter equations, the time evolution equatio n can be derived in the following [5].

$$\frac{d\varepsilon}{3\sqrt{\varepsilon}(\varepsilon+B)} = -\sqrt{\frac{8\pi G}{3}}\,dt \qquad (1)$$

It helps us to evaluate the temporal evolution of the density of energy ε, by we know just the pressure P, $P \equiv P(\varepsilon)$. Throughout this study we analytically solved the above equation, using some previously inferred state equations and estimating the time evolution of certain thermodynamic quantities for gluon in the early universe, such as energy density ε, temperature T and pressure P.

2. Equation of State

The equation of state (EOS), in thermodynamic, describes the relationship between the state functions of a thermodynamic system. It can describe the state of the system and the way it changes. Equations of state are used to identify the properties of gases, liquids and mixtures of liquids as well as the properties of solid matter. The system in thermodynamics (which is a department of physics and chemistry and a number of branches of engineering). A system of limited size (gas, liquid, solids, or a mixture there of). We conduct our observations on it, it is characterized by a balanced energy condition. This applies to a closed system, i.e. there is no heat or radiation exchange or material exchange between the system and the surrounding medium. This is in contrast to an "open system" and is in exchange with the surrounding medium, and between them there is an exchange of materials or heat [6]. In this study, the focus is on the equations of state (EOS) of the quark gluon plasma QGP and finding an analytical solution to a specific case in the case of the free gluons. Equations of state of the quark gluon plasma were extensively used in cosmology and astrophysics, where the first equation was derived in the MIT bag model [7]. We want to investigate how fluctuations in the EOS influence the time evolution of the gluons in the early universe. We believe this study is important in order to confirm numerical solution previously calculated by other researchers in order to be able to compare and think about other solutions for scientific research service.

3. MIT Bag Model

The MIT bag model is a very simple phenomenological model. It was developed by a physicist Chodos in 1974 at the Massachusetts Institute of Technology in Cambridge in the United States of America after a brief period wording of quantum chromo-dynamic and it became a main instrument for researchers in the field of hadron physics. Scientists evidenced that bag model results in to energy momentum conservation violation at the bag surface, unless the internal pressure inside the bag is balanced by an external pressure. This led to some modification to the model, by using quarks carrying colour, they managed to partially destroy the real vacuum inside the bag. Quarks are subjected by a fixed external pressure, to move only in a specific spatial area, one perception is that of flexible bag allows to the quarks to move freely inside it in case of quark confinement and so long as we don't allow them to be isolated out. But if you try to take the quark out, the bag extends and resists. This combination of quarks and real vacuum made it possible to treat the physics of the interior of the bag by troubled quantum chromo-dynamics, this is called troubled vacuum inside the bag. This change in the model of the bag leads to a new boundary case. The necessity condition of pressure balance at the surface can be written as follows [8-9].

$$-\frac{1}{2} n^{\mu}\, \partial_{\mu}(\textstyle\sum_i \bar{\psi}_i \psi_i)|_S = \mathcal{B}, \qquad (2)$$

where B is the bag constant, i runs over all quarks contained in the bag, n^{μ} is normal to the surface at given point, ψ N component Dirac field and transformation of ψ represents as follow

$$\psi(x) \rightarrow \bar{\psi}(x) = U(x)\psi(x) = e^{-i\tau.\alpha(x)}\psi(x), \qquad (3)$$

where $U(x)$ is the operator of the transformation, τ generators and $\alpha(x)$ is the parameters of the transformation.

As we mentioned, inside the "bag", the quarks and gluons freely move and the deconfined phase (which describes a system of these particles that have relative freedom of movement), can be created by compressing the bags against one another. And after that, the plasma constituents are free to move through large spatial areas at these high baryon numbers and energy densities. A high temperature increases the existence of quark-anti-quark pairs. Even under these conditions, the bag constant still represents some non-perturbative element. Energy density and pressure are given respectively by

$$\varepsilon = \frac{37\pi^2}{30} T^4 + \mathcal{B} \quad \text{and} \quad p = \frac{37\pi^2}{90} T^4 - \mathcal{B}. \qquad (4)$$

Upon eliminating the temperature T from the above equations we get

$$p(\varepsilon) = \frac{1}{3}(\varepsilon - 4\mathcal{B}). \qquad (5)$$

In this study, the focus was on solving the time evolution of temperature in the early universe in MIT bag model for case of gluon only. The equation of state of gluon are given [7,10]

$$\varepsilon_g = \frac{8\pi^2}{15} T^4 + B, \qquad (6)$$

$$p_g = \frac{8\pi^2}{45}T^4 - B. \quad (7)$$

Where ε_g is the energy density of gluon, p_g is the pressure of gluon, T is the temperature and □□is the bag constant.

4. Analytical Solution for Temperature

In this section, we derive the analytical solution of differential equation that represents the time evolution of temperature. We start with the time evolution of energy density equation which is given as

$$\frac{d\varepsilon}{3\sqrt{\varepsilon}(\varepsilon+B)} = -\sqrt{\frac{8\pi G}{3}}dt \quad (8)$$

From the eqs[6,7] we obtained

$$d\varepsilon = \frac{4\times 8\pi^2 T^3}{15}dT \ , \ (\varepsilon + B) = \frac{32\pi^2}{45}T^4 \quad (9)$$

By substitute Eq. 9 in Eq. 8 and integration of both sides we get

$$\int_{T_0}^{T} \frac{1}{T\sqrt{\frac{8\pi^2}{15}T^4+B}}dT = -\int_{t_0}^{t}\sqrt{\frac{8\pi G}{3}}dt \quad (10)$$

Let $x = T^2 \Rightarrow dx = 2TdT, dT = \frac{dx}{2\sqrt{x}}$. By substitute in above Eq. we get

$$\frac{1}{2}\int_{\sqrt{x_0}}^{\sqrt{x}} \frac{1}{x\sqrt{\frac{8\pi^2}{15}x^2+B}}dx = -\int_{t_0}^{t}\sqrt{\frac{8\pi G}{3}}dt$$

$$\frac{\sqrt{15}}{4\sqrt{2}\pi}\int_{\sqrt{x_0}}^{\sqrt{x}} \frac{1}{x\sqrt{x^2+\frac{15B}{8\pi^2}}}dx = -\int_{t_0}^{t}\sqrt{\frac{8\pi G}{3}}dt$$

$$\frac{\sqrt{15}}{4\sqrt{2}\pi}\int_{\sqrt{x_0}}^{\sqrt{x}} \frac{1}{x\sqrt{x^2+\alpha^2}}dx = -\int_{t_0}^{t}\sqrt{\frac{8\pi G}{3}}dt,$$

where $\alpha^2 = \frac{15B}{8\pi^2}$

$$-\frac{\sqrt{15}}{4\alpha\sqrt{2}\pi}\left[\ln|\frac{\alpha+\sqrt{x^2+\alpha^2}}{x}|\right]_{\sqrt{x_0}}^{\sqrt{x}} = -\left[\sqrt{\frac{8\pi G}{3}}t\right]_{t_0}^{t}$$

$$\ln\frac{T_0^2[\alpha+\sqrt{T^4+\alpha^2}]}{T^2[\alpha+\sqrt{T_0^4+\alpha^2}]} = \frac{K}{a}(t-t_0); a = \frac{\sqrt{15}}{4\alpha\sqrt{2}\pi}, k = \sqrt{\frac{8\pi G}{3}}$$

$$\frac{T_0^2[\alpha+\sqrt{T^4+\alpha^2}]}{T^2[\alpha+\sqrt{T_0^4+\alpha^2}]} = e^{\frac{K}{a}(t-t_0)}$$

$$\frac{T^2[\alpha+\sqrt{T_0^4+\alpha^2}]}{T_0^2[\alpha+\sqrt{T^4+\alpha^2}]} = e^{-\frac{K}{a}(t-t_0)}$$

$$\frac{T^2}{[\alpha+\sqrt{T^4+\alpha^2}]} = C; C = \frac{T_0^2}{[\alpha+\sqrt{T_0^4+\alpha^2}]}e^{-\frac{K}{a}(t-t_0)} \quad (11)$$

$$T^2 = \frac{2\alpha C}{1-C^2} \quad (12)$$

$$T = \sqrt{\frac{2\alpha C}{1-C^2}} \quad (13)$$

Below we show the graphic representation of the time evolution of temperature for gluon state only in this model

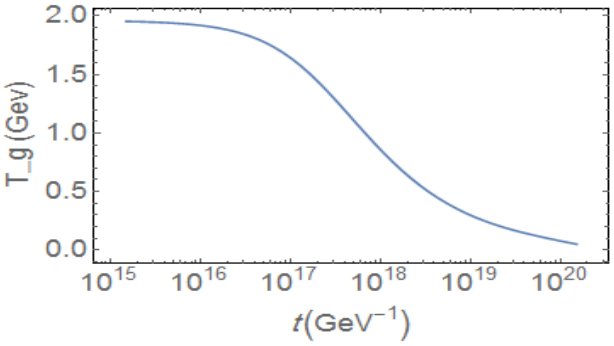

Figure 1. *Time evolution of temperature.*

In this solution we used the initial condition [11], it was converted to natural units, Giga-electron volts as follow

$$\varepsilon_i(t_i) = 10^7 \ MeV/fm^3 = 7.674\times 10(Gev)^4 \ at \ t_i = 10^{-9} \ s = 1.52\times 10^{15}(Gev)^{-1} \quad (14)$$

In graphical representation. The evolution from the time of the electroweak transition phase $t_i = 1.52\times 10^{15}(Gev)^{-1}$, to the time of the quantum chromodynamics phase transition, $t_f = 1.52\times 10^{20}(Gev)^{-1}$. For the current study, we are mainly interested in obtaining analytic equations that describe the time evolution of the temperature, energy density and pressure for the plasma in the early universe during the time period discussed above. In figure 1 we display the time evolution of the temperature resulting by solving Eq. 1 with the MIT bag model equation of state of a gluon gas after converting it in terms of temperature and time. By looking at the figure, one can notice that the temperature was very high and then began to drop dramatically during this period. From the above equation of temperature we can find the energy density and pressure to same state respectively

$$\varepsilon_g = \frac{8\pi^2}{15}(\frac{2\alpha C}{1-C^2})^2 + B \quad (15)$$

$$p_g = \frac{8\pi^2}{45}(\frac{2\alpha C}{1-C^2})^2 - B \quad (16)$$

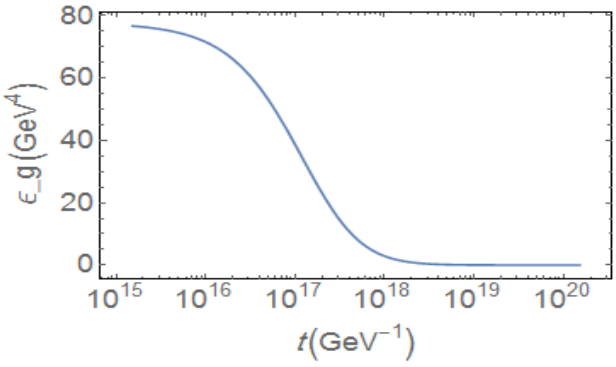

Figure 2. *Time evolution of energy density.*

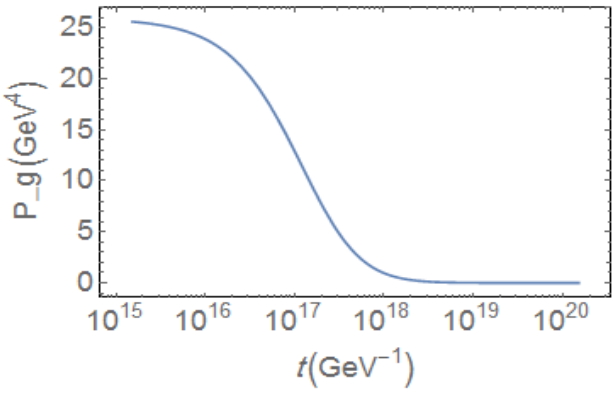

Figure 3. *Time evolution of pressure.*

In figures 2 and figure 3 we displayed time evolution of energy density and time evolution of pressure respectively.

5. Conclusions

As mentioned earlier in this work, in view of the experimental and theoretical studies that relevant to cosmology, show that the Universe was filled with dense plasma. This plasma consisted of deconfined quarks and gluons. This case of plasma is called as Quark-Gluon plasma. So, understanding this state allows us to learn more about the early universe. During the era of Quark-Gluon Plasma, the area of the relevant parameter consists of the total energy density, pressure, and temperature. Owing to the experimental data of heavy ion collisions, modern astrophysical measurements and also the developments in lattice QCD calculations, our understanding of the equation of state of the quark gluon plasma has been growing rapidly. These advanced results have helped us to understand of the time evolution of thermodynamic parameters at the beginning of the universe. We took the equations of state for the gluon that binds energy density and pressure to its temperature in the MIT bag model and solved Fried-man's differential equations that govern the time evolution of energy density, temperature, and pressure. We have showed that changes in the equations of state of gluon can lead to changes in the time evolution of these thermodynamic parameters in the early Universe in MIT bag model. Finally, we confirm that there are still some other components of the quark gluon plasma phase and other analytical solution for various models.

Acknowledgement

Author thanks to Dr. Gaber Faisal for his guidance during preparation and publication of this paper.

References

[1] Rafelski, Johann and Berndt Muller. Strangeness production in the quark gluon plasma. Physical Review Letters 48 no. 16 (1982): 1066.

[2] Markum, H., M. Meinhart, G. Eder, M. Faber, and H. Leeb. "Interactions between quark clusters in lattice QCD." *Physical Review D* 31, no. 8 (1985): 2029.

[3] Pickering, Andrew, and James T. Cushing. "Constructing quarks: A sociological history of particle physics." (1986): 381-383..

[4] Griffiths, David. *Introduction to elementary particles*. John Wiley & Sons, 2008.

[5] Collins, John C., and Malcolm J. Perry. "Superdense matter: neutrons or asymptotically free quarks?." *Physical Review Letters* 34, no. 21 (1975): 1353.

[6]http://en.wikipedia.org/wiki/Equation of state 2011 /11/ 2

[7] Chodos, Ao, R. L. Jaffe, K. Johnson, Charles B. Thorn, and V. F. Weisskopf. "New extended model of hadrons." *Physical Review D* 9, no. 12 (1974): 3471.

[8] Guardo, G. L., V. Greco, and M. Ruggieri. "Energy density fluctuations in Early Universe." In *AIP Conference Proceedings*, vol. 1595, no. 1, pp. 224-227. American Institute of Physics, 2014.

[9] Florkowski, Wojciech. "The realistic QCD equation of state in relativistic heavy-ion collisions and the early Universe." *Nuclear Physics A* 853, no. 1 (2011): 173-188.

[10] Sanches Jr, S. M., F. S. Navarra, and D. A. Fogaça. "The quark gluon plasma equation of state and the expansion of the early Universe." *Nuclear Physics A* 937 (2015): 1-16.

[11] Fogaça, D. A., L. G. Ferreira Filho, and F. S. Navarra. "Nonlinear waves in a quark gluon plasma." *Physical Review C* 81, no. 5 (2010): 055211.

International Journal of Computational and Experimental Science and ENgineering (IJCESEN)
Vol. 6-No.2 (2020) pp. 102-107
http://dergipark.org.tr/en/pub/ijcesen

ISSN: 2149-9144

Research Article

An Investigation of the Formability, Mechanical Properties and Microstructure of Niobium and Niobium-Titanium Microalloyed Steels

Ali Murat SANCAKTAR, Sebahattin KIRTAY, Aliye ARABACI*

Istanbul University-Cerrahpasa, Engineering Faculty, Department of Metallurgical and Materials Eng.
34320 Avcilar - Istanbul / Turkey

* **Corresponding Author** : aliye@istanbul.edu.tr
ORCID: 0000-0003-1209-8618

Article Info:

DOI: 10.22399/ijcesen.720035
Received : 14 April 2020
Accepted : 11 June 2020

Keywords

Formability
Microalloys
Steel
Strength

Abstract:

Microalloyed steels are widely used in the automotive sector due to their formability and strength. One example application is rim manufacturing where the cost of wheel is expected to be low. In this study, formability, microstructure and mechanical properties of low carbon steels containing Niobium and Niobium-Titanium as microalloying elements were investigated. The measurements showed that the tensile strength of non-alloyed steel was 433.5 MPa, the yield strength was 292.6 MPa, the tensile strength of Nb alloyed steel was 489 MPa and the yield strength was 385.4 MPa. These values indicate that the tensile strength increase of about 12 % and the yield strength increase of 24 % were obtained. Also for Nb-Ti added steel, the tensile strength was 591.3 MPa and the yield strength was 462.6 MPa. These correspond to 27 % increase in the tensile strength and 37 % increase in the yield strength. Furthermore, elongation values were measured as 27.6 % in non-alloyed steel, 32 % in Nb-added steel, and 28 % in Nb-Ti added steel. In the microstructure analysis, the grain size of Nb and Nb-Ti added alloys were found to be approximately 50 % smaller than the grain size of unalloyed steel. These results indicated that we achieved high elongation values and improved mechanical properties for Nb and Nb-Ti added steel. Furthermore, we managed to hold the elongation value at 27.7 % while achieving higher yield and tensile strengths and formability by adding a small amount of Nb-Ti to the steel.

1. Introduction

Microalloyed or High Strength Low Alloy (HSLA) steels have been used since 1960s. They are estimated to be 12 % of total world steel production. The use of microalloyed steels has played an important role in the expansion of certain key industries such as oil and gas extraction, construction, and transportation [1].

In automotive sector, microalloyed steels enable the production of fuel efficient and improved performance vehicles. Many manufacturers in the automotive industries, have focused on the microalloyed steels because of their mechanical properties [2]. Microalloyed steels have small amounts of elements Nb, V and Ti whose contents vary from 0.001 to 0.1 %. These are combined with elements present in the steel (Mn, Si, Mo) to improve mechanical properties such as strength, toughness, ductility and weldability by the formations and precipitation of carbide, nitride and carbonitrides [3-6].

Mild steel has a lower yield strength, σy, of 150-200 MPa. On the other hand, microalloyed steels are designed to have a yield strength between 500 and 750 MPa without heat treatment, with the potential to exceed 1000 MPa [7]. The weldability of microalloyed steel is at least equal to that of mild steel, and can be improved by reducing carbon content while maintaining strength. In microalloyed steels, fatigue life and wear resistance are superior to similar heat-treated steels. The disadvantages are

that ductility and toughness are not as good as quenched and tempered (Q&T) steels [8]. Furthermore, microalloyed steels permit reductions in component weight and manufacturing cost.

This work has investigated effects of Niobium and Niobium-Titanium additions in mild steels by examining microstructure and mechanical properties. The impact on the formability properties has also been examined.

2. Materials and Method

Samples used in this work were produced in an iron and steel plant located in Turkey. Fe-Ti ve Fe-Nb were used in the microalloying process. The Nb and Nb–Ti containing steels described here were applied industrial heating, continuous casting and hot rolled before sampling. The samples were subject to tensile tests. Optical and scanning electron microscope analyses were implemented for grain size measurements and fracture surface investigations. Table 1 shows non-microalloyed EN 10025-2:2004 S275JRC (RSt37-2), Nb-added EN 10149-2:2013 S355MC (QStE 380TM) and Nb-Ti added EN 10028-3 - P355NH (WStE 355) steels that were used in this work together with their chemical compositions.

Table 1. *Chemical composition of steels used in experimental study*

Alloying Element (%)	**EN 10025-2:2004 S275JRC (RSt37-2)**	**EN 10149-2:2013 S355MC (QStE 380TM)**	**EN 10028-3 - P355NH (WStE 355)**
C	0.14	0.08	0.17
Mn	1.2	0.9	1.6
Si	0.1	0.006	0.4
Ti	0.0003	0.0002	**0.017**
V	0.0005	0.0007	-
Ni	0.0326	0.028	0.0332
Nb	0.0001	**0.055**	**0.04**

Samples shown above in Table 1 were grinded and polished. This was followed by etching with 2% Nital solution for metalographic examination which was performed with Nikon Eclipse MA200 optical microscope. The grain size was estimated using a linear-intercept method. Intercept lengths were determined and then converted into nominal grain diameters using standard tables.
Standard tensile tests were conducted at room temperature on longitudinal specimens machined according to EN 6892-1 (ISO 6892-1:2016) specification [9] using computerised tensile testing system with Zwick / Z1200 equipment.

Fracture surface analysis were undertaken with JEOL JSM 5600 SEM (Scanning Electron Microscopy) to examine microstructure, distribution and morphologies of carbide and carbonitride compounds of microalloyed elements.

3. Results and Discussions

Figures 1-3 show microstructures of non-microalloyed EN 10025-2:2004 S275JRC (RSt37-2), Nb-added EN 10149-2:2013 S355MC (QStE 380TM) and Nb-Ti added EN 10028-3 - P355NH (WStE 355) steels, respectively.

In Figure 1, black areas show pearlite phase and white areas indicate acicular ferrite phase. Acicular ferrite is a structure that forms in unalloyed and low alloy steel during the solidification from the austenite phase. As can be seen, the amount of pearlite formation is limited. The average grain size was measured to be 7 μm.

In Figure 2, black areas show pearlite, white areas show ferrite and grey areas show Nb[C, N] carbides and nitrides. As can be seen, the grain size of microalloyed steel is smaller than that of the non-microalloyed steel. This is due to the precipitation of carbide and nitride at the grain boundry. The average grain size was measured to be 4 μm.

In Figure 3, black areas show pearlite phase and white areas show ferrite phase. The banded region shown in Figure 3a indicates the presence of Ti carbides. The grey areas show Nb carbides. The average grain size is measured to be approximately 5 μm. Furthermore, microstructures of added microalloying elements show that the amount of pearlite phase has increased. This may indicate that microalloying elements prevent ferrite formation while supporting pearlite formation.
For the tensile test, five samples were taken from each specimen group. The arithmetic means of measured values are shown in Table 2.

The results shown in Table 2 suggest that the yield strength of Nb-added steel has increased by 24 % compared to that of non-microalloyed steel. Similarly, the Nb-Ti added steel has its yield strength incerased by 37 %. The tensile strength was increased by 12 % for the Nb-added steel and 27 % for the Nb-Ti added steel compared to that of non-microalloyed steel. Preciptation phases affect mechanical properties of microalloyed steels. Microalloying elements, such as Nb and Ti and their combination, result in carbide, nitride and corbonitride precipitation phases.

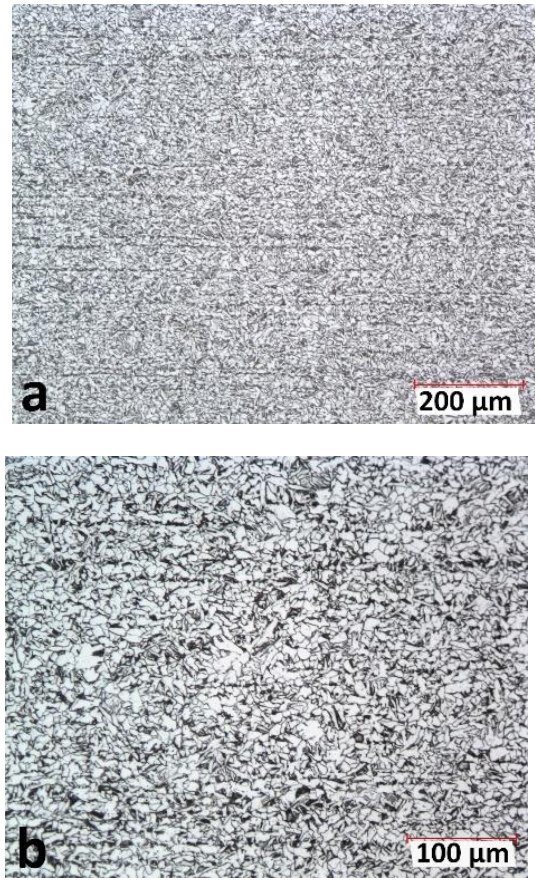

Figure 1. *Microstructure of non-microalloyed steel (EN 10025-2:2004 S275JRC (RSt37-2))*
(in figure c a : acicular ferrite b : pearite)

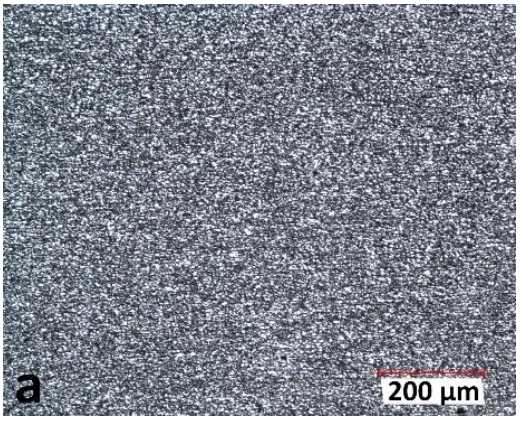

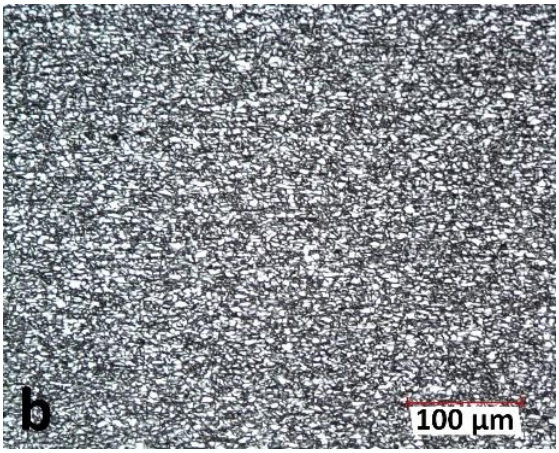

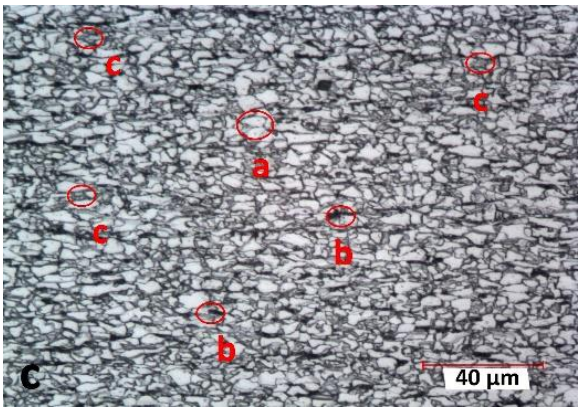

Figure 2. *Microstructure of Nb-added microallyed steel (EN 10149-2:2013 S355MC (QStE 380TM))*
(in figure c a : ferrite b : pearite c : NbC)

Table 2. *Tensile tests results.*

	EN 10025-2:2004 S275JRC (RSt37-2)	**EN10149-2:2013 S355MC (QStE 380TM)**	**EN 10028-3 - P355NH (WStE 355)**
Yield Strength (MPa)	292.6 ±3.45	385.4 ±13.74	462.6 ± 2.41
UTS (MPa)	433.5 ±7.95	489 ±8	591.3 ± 6.5
Elongation %	27.6	32	27.7

The distribution of these phases in microstructures prevents the dislocation movements and increases strength due to precipitation hardening [10]. Najafi et al [11] examined the impact of Nb and V in mechanical properties of microalloyed steels. They pointed out that the improvement in mechanical properties is the result of Nb(C,N) formation in ferrite phases. Our results are in agreement.

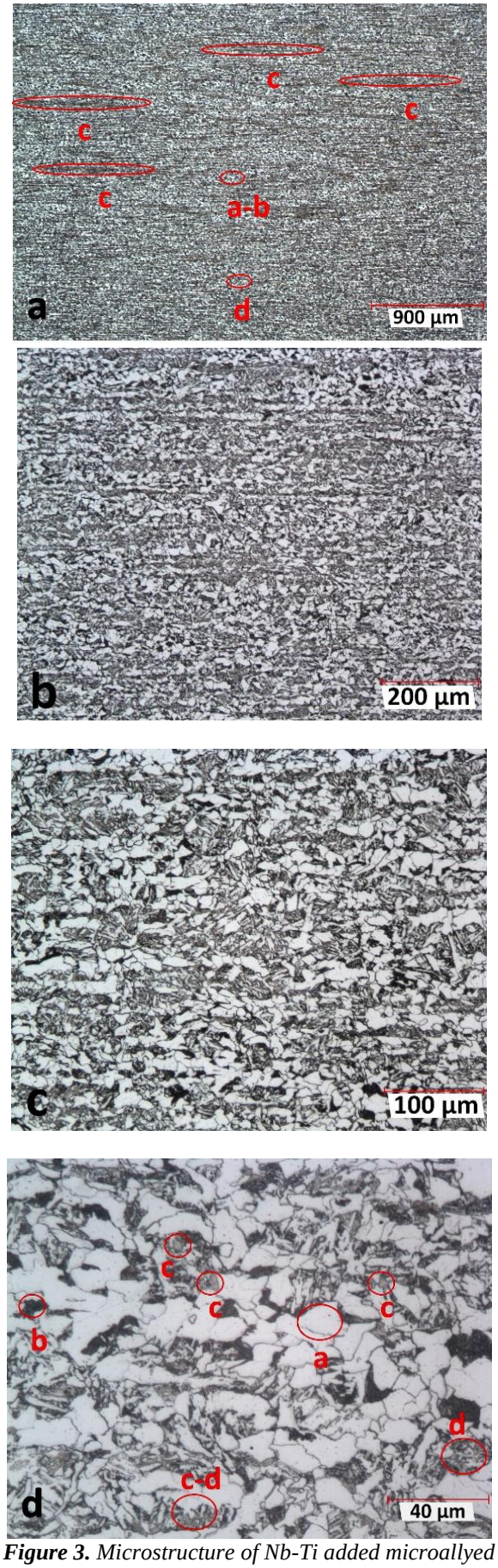

Figure 3. *Microstructure of Nb-Ti added microallyed steel* ***(****EN 10028-3 - P355NH (WStE 355))*
(in figure a,d a : ferrite b : pearite c : Ti[C,N] d : NbC)

El-Faramawy et al argued that the addition of Ti in steel for microalloying reduces the grain size and this prevents the dislocation movement which, in turn, causes improvement in the mechanical properties [12].

Fractography of tensile specimens was carried out under scanning electron microscopy and the fracture surfaces were examined. Nb and Nb-Ti added specimen were examined using SEM analyses (Figure 4). In Figures 4a and 4b, fracture surfaces of the Nb-added steel are shown. Figures 4c and 4d illustrate fracture surfaces of the Nb-Ti added steel. From these figures, we can observe better toughness depending on whether they show dimple ductile or cleavage fracture. If a specimen shows dimple and toughness features this can be an advantage in terms of formability. SEM photographs show that the Nb-Ti added specimen has sponge-like and matt fracture surfaces. The Nb-added specimen has more dense cleavage fracture than that of the Nb-Ti added specimen. In particular, we observe typical cleavage fractures. The Nb-Ti added specimen shows clear dimple ductile fractures. This suggests a presence of high energy and toughness. The cleavage fracture requires a low energy and it is intergranular. The result is a leaf-like shape. Fractures in the Nb-Ti added specimen are the result of fracturing at the grain boundry rather than fracturing inside the grains. Therefore, the Nb-Ti added specimen has resulted in higher toughness. Davis et al [13] examined the fracture behaviour of medium carbon Ti-V-N and V-N microalloyed ferritic-pearlitic ve bainitic steels. They suggested that Titanium reduces the austenite grain size, creates rough (Ti, V) (C,N) particules and decreases toughness by heat transfer. In our work, Vanadium was not used and, contrary to Davis et al, it was shown that Nb-Ti addition improves the toughness.

4. Conclusions

In this work, the formability and mechanical properties of Nb and Nb-Ti microalloyed steels were examined by comparing against mild steel. In order to examine the impact of Nb and Nb-Ti, EN 10149-2:2013 S355MC and EN 10028-3 - P355NH were selected, respectively. For non-microalloyed steel, EN 10025-2:2004 S275JRC was used. The results of tensile tests have shown that the yield strengths of Nb and Nb-Ti added steels were increased by 24 % and 37 %, respectively, compared to that of non-alloyed steel. Similarly, the tensile strengths of Nb and Nb-Ti added steels were increased by 12 % and 27 %, respectively, compared to that of non-alloyed steel.

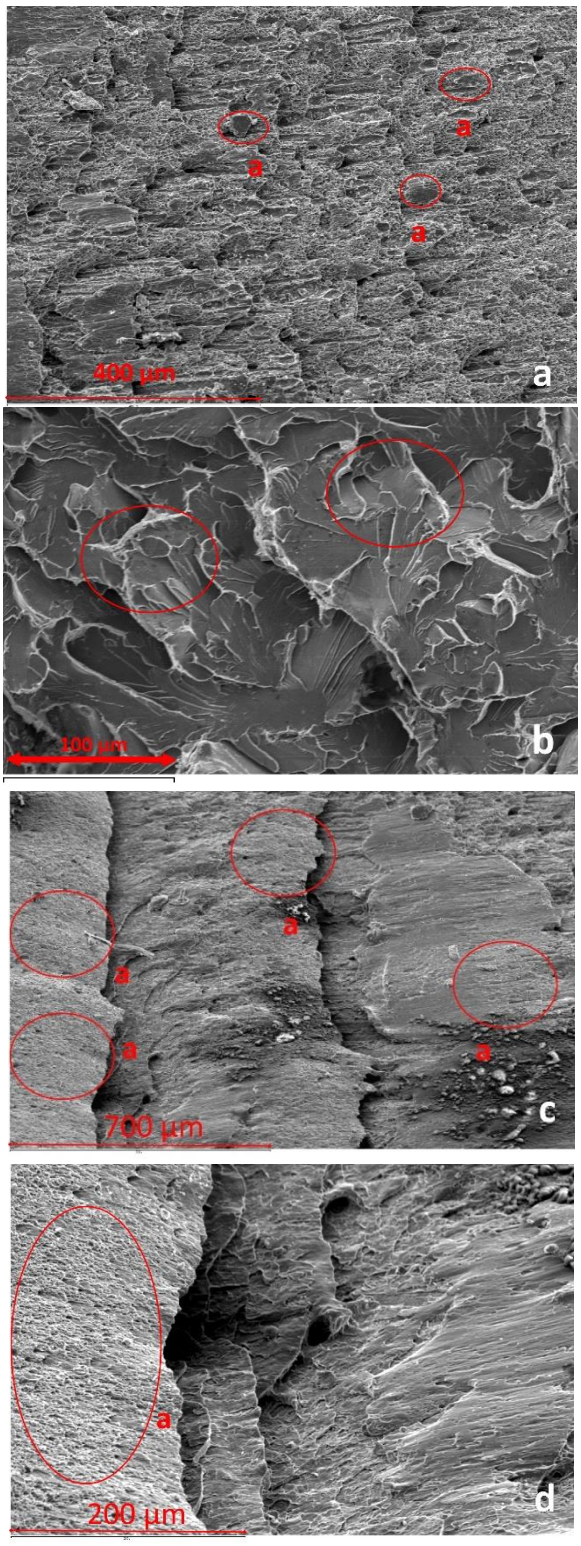

Figure 4. *Fracture surfaces of samples (a, b Nb-added steel, c and d Nb-Ti added steel)*
(in figure c and d, a : dimple ductile fracture)

The average grain sizes of Nb and Nb-Ti added steels were measured as 4 and 5 µm, respectively. The grain size of the non-alloyed steel was 7 µm. The reduction in the measured grain size indicates better toughness which, in turn, leads to increasing yield and tensile strengths. These values also suggest that Nb and Nb-Ti added steels improve formability.

It should be noted that higher yield and tensile strengths and formability were achieved without reducing the elongation value by adding a small amount of Nb-Ti to the steel.

It was also shown that microalloying elements prevent ferrite formation and support pearlite formation.

When comparing the formability properties of Nb and Nb-Ti added steels the fracture behaviour relating to ductile and toughness features was considered. It was shown that Nb and Nb-Ti added steels have a better formability properties compared against the formability properties of non-alloyed steels.

References

[1] C. J. Van Tyne, D. K. Matlock, and J. G. Speer, "Microallyed Forging Steels" International Forging Congress, (2008) 189-197.

[2] M. Hajisafari, S. Nategh, H. Yoozbashizadeh, A. Ekrami, "Improvement in Mechanical Properties of Microalloyed Steel 30MSV6 by a Precipitation Hardening Process" J. of Iron and Steel Research. (2013)66-73, DOI: 10.1016/S1006-706X(13)60100-4

[3] Xiao-Huai Xue, Yi-Yin Shan, and Song-Nian Lou, "Microstructure Characteristic of Low Carbon Microalloyed Steels Produced by Thermo-Mechanical Controlled Process" Materials Science &Engineering A. 438-440 (2006) 285-287, DOI: 10.1016/j.msea.2006.02.064

[4] M. Niikura, M. Fujioka, Y. Adachi, A. Matsukura, T. Yokota, Y. Shirota, and Y. Hagiwara, "New Concepts for Ultra Refinement of Grain Size in Super Metal Project" J. Mater. Process. Technol. 117 (2001) 341-346, DOI: 10.1016/S0924-0136(01)00800-7

[5] E. Esenera , E. Sönmeza , M. Özsoyb and M. Firatb,∗ "Determining Springback Behavior of High-Strength Steels via Channel Forming Process" Acta Physica Polonica A. 132 (2017)1010-1012, DOI: 10.12693/APhysPolA.132.1010

[6] V. Onar, S. Aslanlar and N. Akkaş, "Effect of Welding Current on Tensile–Peel Loading of Welding Joints in TRIP 800 and Micro-Alloyed Steels in Resistance Spot Welding" Acta Physica Polonica A 132(2017) 822-824, DOI: 10.12693/APhysPolA.132.822

[7] H. Xie, L-X. Du, J. Hu and R.D.K. Misra, "Microstructure and mechanical properties of a novel 1000 MPa grade TMCP low carbon microalloyed steel with combination of high strength and excellent toughness" Mater. Sci. Eng. (2014) A612 123-130, DOI: 10.1016/j.msea.2014.06.033

[8] E. Paul DeGarmo, J T. Black Ronald, A. Kohser, Materials and Process in Manufacturing, Ninth Edition, 2003 John Wiley & Sons, Inc.

[9] European Committee for Standardization, "Metallic materials - Tensile testing - Part 1: Method of test at room temperature" (ISO 6892-1), 2016.

[10] Danijela A. Skobir, "High-Strength Low-Alloy (HSLA) Steels" Materials and Technology. 45 (2011) 4 295-301.

[11] H. Najafi, , R. Jafar, S. Asgari, "As-cast mechanical properties of vanadium/niobium microalloyed steels" Materials Science and Engineering. (2008) A 408 1-7, DOI: 10.1016/j.msea.2007.08.057

[12] Hoda S. El-Faramawy, Saeed N. Ghali, Mamdouh M. Eissa, "Effect of Titanium Addition on Behavior of Medium Carbon Steel" Journal of Minerals and Materials Characterization and Engineering. (2012) 11 1108-1112, DOI: 10.4236/jmmce.2012.1111118

[13] C. L. Davis, M. J. Balart, M. Strangwood, "Fracture Behaviour In Medium-Carbon Ti–V–N And V–N Microalloyed Ferritic-Pearlitic And Bainitic Forging Steels With Enhanced Machinability" Materials Science and Engineering A. 328 48-57, DOI: 10.1016/s0921-5093(01)01679-3

International Journal of Computational and Experimental Science and ENgineering (IJCESEN)
Vol. 6-No.2 (2020) pp. 108-121
http://dergipark.org.tr/en/pub/ijcesen

ISSN: 2149-9144

Research Article

Analysis of Laser Pulse Heating Model Using the Finite Element Analysis

Erhuvwuvoke EBOJOH[1*], John Ajokpaoghene AKPOBI[2], Kelechi NWOSU[2]

[1]University of Benin, Faculty of Engineering, Department of Production Engineering, Benin City, Nigeria
[2]University of Benin, P.M.B 1154 Benin City, Nigeria

***Corresponding Author:** voke.ebojoh@uniben.edu
ORCID: 0000-0001-5432-6020

Article Info:

DOI: 10.22399/ijcesen.620040
Received : 13 September 2019
Accepted : 13 July 2020

Keywords

Finite Element Method (FEM)
Rectangular discretization
Triangular discretization
Lagrange interpolation function
Laser

Abstract:

The Model equation for the laser heating process is a two dimensional partial differential equation in cylindrical coordinate that is time dependent and involves a source term. This work presents a sequential method in obtaining solution to the laser heat equation using a unique method of solution known as Finite Element Method; a numerical approach as against the analytical method. The approach was used in analyzing the temperature of the irradiated material within the domain of the material. This was done by multiplying the model differential equation by a weighted function and carrying out integration over the domain of the problem to obtain the weak form of the equation. Triangular and rectangular Langrage interpolation functions were used for the spatial discretization and Alpha family of approximation was used for the time approximation. The domain of the problem was discretized manually using eight triangular and 4 rectangular finite element mesh. To obtain more accurate solutions, a programme written with MATLAB software was used to further discretize the domain into smaller finite elements (4000 triangular element mesh and 2000 rectangular element mesh). The results obtained was plotted and compared with literature.

1. Introduction

The Finite Element Method (FEM) (Sometimes referred to as Finite Element Analysis (FEA) is a numerical technique for finding approximate solution to partial differential equation (PDE), ordinary differential equation (ODE) as well as integral equations. This solution approach is based on either eliminating the differential equation completely (steady state problem), or rendering the PDE into an approximating system of ordinary differential equation, which are then numerically integrated using standard techniques. The concept of Finite element is well treated in many standard texts [1] and [2].As a result of the complexity and relative longer time to obtain analytical solution to several engineering model partial differential equation being developed by various researchers, approximate method of solutions (such as Finite difference and Finite Element) are often used for such analysis. Also to aid the computation some commercially developed Finite Element software like ANSYS, ADINA, Abaqus, GetFEM++, VisualFEA, JMAG, Nastran, Mecway are also used for analysis as well as to carry out simulations. Finite Element Method of numerical solution have been used to solve various engineering problems, [3] used finite element to analyze the distribution of velocity in viscous incompressible fluid flow using Lagrange interpolation function. Reference [4] investigated the Boussinesq-type flow model for non linear dispersive wave. They used Finite element discretization technique in their analysis of the wave equation.

Reference [5] Investigated numerically the mixed convection heat transfer through a vertical wavy isothermal channels the governing equations consisting of continuity, momentum and energy equations were solved numerically by finite element method using Characteristic Based Split (CBS) algorithm, the effect of Reynolds, Prandtl and Grashof numbers on flow and thermal fields were also investigated. Reference [6] used finite element method to analyze convective heat transfer in a porous medium. This method was used to analyze the convection in vertical surface embedded in the medium and convection in a confined porous medium enclosure. Considerable research studies have been carried out to explore heating and machining processes. Reference [7] gave an overview of the state of the art laser beam machining in general with special emphasis on applications of short and ultra-short lasers. The research showed that in micro-machining, shorter pulses reduce heat-affected damage of the material and opens new ways for nanometer accuracy. Reference [8] examined the laser thermal stresses during the laser drilling process. Other works on laser beam machining include those of [9]–[13].

Reference [14] used a numerical solution to analyze the partial differential heat equation. They examined the cavity depth and formations in the irradiated steel. Also [15] used Laplace transformation method to obtain an analytical solution for laser short pulse heating due to evaporative boundary condition. In this paper the laser heat equation is solved using both rectangular and triangular Finite Element discretization. A program written with MATLAB was used to increase the number of elements used for the discretization and to decrease the time step which consequently produced very accurate solution relative to the manual discretization.

2. Methodology

The governing equation being solved is the heat equation in cylindrical coordinate with an exponential source term (the Laser pulse), given as;

$$\rho c_p \frac{\partial T}{\partial t} = \frac{k}{r}\frac{\partial}{\partial r}\left(r\frac{dT}{dr}\right) + k\frac{\partial^2 T}{\partial z^2} + \left(I_o\delta(1-r_f)\exp(-\delta z)\exp\left(-\frac{r^2}{a^2}\right)\right) \quad (1)$$

Where c_p = Specific heat capacity, k = Thermal conductivity δ = absorption coefficient ρ = density, r_f = reflectivity I_0 = laser peak power intensity a = Gaussian parameter

conditions are as follows;

Initial condition at time $t = 0$

$$t = 0 \rightarrow T(r,z,0) = T_o \quad (2)$$

At the boundary,

$$z = b \rightarrow T(r,b,t) = T_o \quad (3)$$

$$r = a \rightarrow T(a,z,t) = T_o \quad (4)$$

From Symmetry

At position $r = 0 \rightarrow \frac{\partial T(0,z,t)}{\partial r} = 0$

At the surface where $z = 0 \rightarrow \frac{\partial T(r,0,t)}{\partial z} = 0 \quad (5)$

To obtain the weak form of (1), we multiply (1) by a weight function V and integrate over the domain

$$0 = \int_\Omega \left[\left(\rho c_p \frac{\partial T}{\partial t}\right) - V\frac{k}{r}\frac{\partial}{\partial r}\left(r\frac{dT}{dr}\right) - Vk\frac{\partial^2 T}{\partial z^2} - V\left(I_o\delta(1-r_f)\exp(-\delta z)\exp\left(-\frac{r^2}{a^2}\right)\right)\right] rdrdz \quad (6)$$

Representing $\left(I_o\delta(1-r_f)\exp(-\delta z)\exp\left(-\frac{r^2}{a^2}\right)\right)$ (7)

as f and carrying out integration by parts our week form becomes;

$$0 = \int_\Omega \left[Vr\left(\rho c_p \frac{\partial T}{\partial t} - Vf\right) + k\frac{\partial V}{\partial r}\left(r\frac{dT}{dr}\right) + k\frac{\partial V}{\partial z}r\frac{\partial T}{\partial z}\right] drdz - \left[\int_\Gamma q_n V ds\right] \quad (8)$$

where $q_n = r\frac{\partial T}{\partial r}n_r + r\frac{\partial T}{\partial z}n_z \quad (9)$

To obtain the Finite Element model, we assume an approximation solution for an element "e" of the form;

$$T(r,z,t) = \sum_{j=1}^{n}\left(T_j^e(t)\psi_j^e(r,z)\right) \quad (10)$$

The semi discrete finite element model is obtained by substituting the finite element approximation for the dependent variable T and substituting V for ψ_i, where ψ is the Lagrange interpolation function for a two dimensional differential equation.

We have the equation in Matrix form as;

$$\left[M_{ij}^e\right]\left\{\dot{T}_j^e\right\}+\left[K_{ij}^e\right]\left\{T_j^e\right\}=\left\{F_i^e\right\}+\left\{Q_i^e\right\} \quad (11)$$

Where functions enclosed in square brackets and curly brackets are square and column matrix respectively.

Also,

$$\frac{dT}{dt}=\dot{T} \quad (12)$$

$$M_{ij}^e=\int_{zaa}^{zaa+b}\int_{zaa}^{zaa+b}\left(\rho c_p r\psi_i\psi_j\right)drdz \quad (13)$$

$$K_{ij}^e=\int_{zaa}^{zaa+b}\int_{raa}^{raa+a}k\left(r\frac{d\psi_i}{dr}\frac{d\psi_j}{dr}+r\frac{d\psi_i}{dz}\frac{d\psi_j}{dz}\right)drdz \quad (14)$$

$$f_i^e=\int_{zaa}^{zaa+b}\int_{raa}^{raa+a}\left(r\psi_i\left(I_0\delta\left(1-r_f\right)\exp\left(-\delta z\right)\exp\left(-\frac{r^2}{a^2}\right)\right)\right)drdz \quad (15)$$

The coefficient matrix for M_{ij}^e, K_{ij}^e and f_i^e are evaluated from (13), (14) and (15);

Where for the rectangle interpolation, i and j takes values of 1, 2, 3 and 4

And for the triangular interpolation, i and j takes values of 1, 2 and 3.

The results of the integration are shown in matrix form, using the rectangular interpolation functions

$$M_{ij}^e=\rho c_p\begin{bmatrix}\frac{\left(ab\left(a+4raa\right)\right)}{36} & \frac{\left(ab\left(a+2raa\right)\right)}{36} & \frac{\left(ab\left(a+2raa\right)\right)}{72} & \frac{\left(ab\left(a+4raa\right)\right)}{72}\\ \frac{\left(ab\left(a+2raa\right)\right)}{36} & \frac{\left(ab\left(3a+4raa\right)\right)}{36} & \frac{\left(ab\left(3a+4raa\right)\right)}{72} & \frac{\left(ab\left(a+2raa\right)\right)}{72}\\ \frac{\left(ab\left(a+2raa\right)\right)}{72} & \frac{\left(ab\left(3a+4raa\right)\right)}{72} & \frac{\left(ab\left(3a+4raa\right)\right)}{36} & \frac{\left(ab\left(a+2raa\right)\right)}{36}\\ \frac{\left(ab\left(a+4raa\right)\right)}{72} & \frac{\left(ab\left(a+2raa\right)\right)}{72} & \frac{\left(ab\left(a+2raa\right)\right)}{36} & \frac{\left(ab\left(a+4raa\right)\right)}{36}\end{bmatrix} \quad (16)$$

Using triangular interpolation function we obtain;

$$M_{ij}^e=\frac{ab\rho c_p}{12}\begin{bmatrix}\left(a+4raa\right) & -raa & \left(a+3raa\right)\\ -raa & \left(a+2raa\right) & -raa\\ \left(a+3raa\right) & -raa & \left(2\left(a+2raa\right)\right)\end{bmatrix} \quad (17)$$

Also for rectangular interpolation function; Due to the presence of the exponential function, the f_i^e coefficient matrix would be evaluated numerically. Fig. 1 and 2 shows the local nodes (node1, node2, node3 and node4) four each of the four rectangular elements and the local nodes (node 1, node 2, and node 3) four each of the eight triangular elements that make up the domain respectively, as well as the global nodes when assembled (node1, node2, …, node8 and node9).fter inputting boundary condition the assembled equation using Rectangular Lagrange interpolation function we have and for the triangular interpolation function

$$K_{ij}^{e}=k\begin{bmatrix}\left(\frac{b\left(\frac{a}{6}+\frac{raa}{3}\right)}{a}+\frac{\left(\frac{a^3}{12}+\frac{raa\cdot a^2}{3}\right)}{ab}\right) & \frac{\left(a^2-2b^2\right)\left(a+2raa\right)}{12ab} & -\frac{\left(a^2+b^2\right)\left(a+2raa\right)}{12ab} & \left(\frac{b\left(\frac{a}{12}+\frac{raa}{6}\right)}{a}-\frac{\left(\frac{a^3}{12}+\frac{raa\cdot a^2}{3}\right)}{ab}\right)\\ \frac{\left(a^2-2b^2\right)\left(a+2raa\right)}{12ab} & \left(\frac{b\left(\frac{a}{6}+\frac{raa}{3}\right)}{a}+\frac{\left(\frac{a^3}{4}+\frac{raa\cdot a^2}{3}\right)}{ab}\right) & \left(\frac{b\left(\frac{a}{12}+\frac{raa}{6}\right)}{a}-\frac{\left(\frac{a^3}{4}+\frac{raa\cdot a^2}{3}\right)}{ab}\right) & -\frac{\left(a^2+b^2\right)\left(a+2raa\right)}{12ab}\\ -\frac{\left(a^2+b^2\right)\left(a+2raa\right)}{12ab} & \left(\frac{b\left(\frac{a}{12}+\frac{raa}{6}\right)}{a}+\frac{\left(\frac{a^3}{4}+\frac{raa\cdot a^2}{3}\right)}{ab}\right) & \left(\frac{b\left(\frac{a}{6}+\frac{raa}{3}\right)}{a}+\frac{\left(\frac{a^3}{4}+\frac{raa\cdot a^2}{3}\right)}{ab}\right) & \frac{\left(a^2-2b^2\right)\left(a+2raa\right)}{12ab}\\ \left(\frac{b\left(\frac{a}{12}+\frac{raa}{6}\right)}{a}-\frac{\left(\frac{a^3}{12}+\frac{raa\cdot a^2}{3}\right)}{ab}\right) & -\frac{\left(a^2+b^2\right)\left(a+2raa\right)}{12ab} & \frac{\left(a^2-2b^2\right)\left(a+2raa\right)}{12ab} & \left(\frac{b\left(\frac{a}{6}+\frac{raa}{3}\right)}{a}+\frac{\left(\frac{a^3}{12}+\frac{raa\cdot a^2}{3}\right)}{ab}\right)\end{bmatrix} \quad (18)$$

$$K_{ij}^{e}=k\begin{bmatrix}\frac{b\left(a+2raa\right)}{2a} & \frac{-b\left(a+2raa\right)}{2a} & 0\\ \frac{-b\left(a+2raa\right)}{2a} & \frac{\left(\left(a^2+b^2\right)\left(a+2raa\right)\right)}{2ab} & \frac{-a\left(a+2raa\right)}{2b}\\ 0 & \frac{-a\left(a+2raa\right)}{2b} & \frac{a\left(a+2raa\right)}{2b}\end{bmatrix} \quad (19)$$

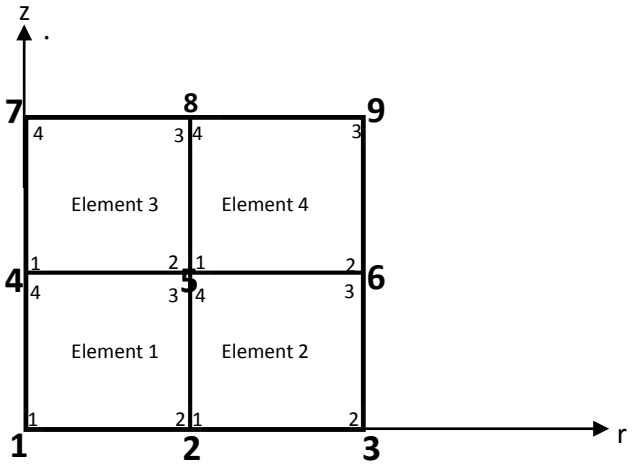

Fig. 1: *Four rectangular element mesh showing positions*

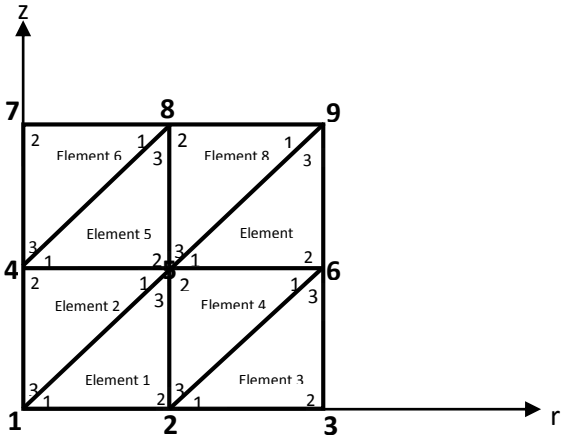

Fig. 2*: Eight triangular element mesh showing nodal nodal positions*

:

$$\begin{bmatrix}K_{11}^{1} & K_{12}^{1} & K_{14}^{1} & K_{13}^{1}\\ K_{21}^{1} & \left(K_{22}^{1}+K_{11}^{1}\right) & K_{24}^{1} & \left(K_{23}^{1}+K_{14}^{2}\right)\\ K_{41}^{1} & K_{42}^{1} & \left(K_{44}^{1}+K_{11}^{3}\right) & \left(K_{43}^{1}+K_{12}^{3}\right)\\ K_{31}^{1} & \left(K_{32}^{1}+K_{41}^{2}\right) & \left(K_{34}^{1}+K_{21}^{3}\right) & \left(K_{33}^{1}+K_{44}^{2}+K_{22}^{3}+K_{11}^{4}\right)\end{bmatrix}\begin{Bmatrix}T_1\\ T_2\\ T_4\\ T_5\end{Bmatrix}$$

$$+\begin{bmatrix} M_{11}^1 & M_{12}^1 & M_{14}^1 & M_{13}^1 \\ M_{21}^1 & \left(M_{22}^1+M_{11}^1\right) & M_{24}^1 & \left(M_{23}^1+M_{14}^2\right) \\ M_{41}^1 & M_{42}^1 & \left(M_{44}^1+M_{11}^3\right) & \left(M_{43}^1+M_{12}^3\right) \\ M_{31}^1 & \left(M_{32}^1+M_{41}^2\right) & \left(M_{34}^1+M_{21}^3\right) & \left(M_{33}^1+M_{44}^2+M_{22}^3+M_{11}^4\right) \end{bmatrix}\begin{Bmatrix} \square \\ T_1 \\ \square \\ T_2 \\ \square \\ T_4 \\ \square \\ T_5 \end{Bmatrix}=\begin{Bmatrix} FF_1^1 \\ FF_2^1+FF_1^2 \\ FF_4^1+F_1^3 \\ FF_3^1+FF_4^2+FF_2^3+FF_1^4 \end{Bmatrix} \tag{20}$$

Where;

$$\begin{Bmatrix} FF_1^1 \\ FF_2^1+FF_1^2 \\ FF_4^1+FF_1^3 \\ FF_3^1+FF_4^2+FF_2^3+FF_1^4 \end{Bmatrix}=\begin{Bmatrix} F_1^1 \\ F_2^1+F_1^2 \\ F_4^1+F_1^3 \\ F_3^1+F_4^2+F_2^3+F_1^4 \end{Bmatrix}-\begin{bmatrix} 0 & 0 & 0 & 0 & 0 \\ K_{12}^2 & K_{13}^2 & 0 & 0 & 0 \\ 0 & 0 & K_{14}^3 & K_{13}^3 & 0 \\ K_{42}^2 & \left(K_{43}^2+K_{12}^4\right) & K_{24}^3 & \left(K_{23}^3+K_{14}^4\right) & K_{13}^4 \end{bmatrix}\begin{Bmatrix} T_o \\ T_o \\ T_o \\ T_o \\ T_o \end{Bmatrix}$$

$$-\begin{bmatrix} 0 & 0 & 0 & 0 & 0 \\ M_{12}^2 & M_{13}^2 & 0 & 0 & 0 \\ 0 & 0 & M_{14}^3 & M_{13}^3 & 0 \\ M_{42}^2 & \left(M_{43}^2+M_{12}^4\right) & M_{24}^3 & \left(M_{23}^3+M_{14}^4\right) & M_{13}^4 \end{bmatrix}\begin{Bmatrix} T_o \\ T_o \\ T_o \\ T_o \\ T_o \end{Bmatrix} \tag{21}$$

And the assembled equation using Triangular Lagrange interpolation function is:

$$\begin{bmatrix} \left(K_{11}^1+K_{33}^2\right) & K_{12}^1 & K_{32}^2 & \left(K_{13}^1+K_{31}^2\right) \\ K_{21}^1 & \left(K_{22}^1+K_{11}^3+K_{33}^4\right) & 0 & \left(K_{23}^1+K_{32}^4\right) \\ K_{23}^2 & 0 & \left(K_{22}^2+K_{11}^5+K_{33}^6\right) & \left(K_{21}^2+K_{12}^5\right) \\ \left(K_{31}^1+K_{13}^2\right) & \left(K_{32}^1+K_{23}^4\right) & \left(K_{12}^2+K_{21}^5\right) & \left(K_{33}^1+K_{11}^2+K_{22}^4+K_{22}^5+K_{11}^7+K_{33}^8\right) \end{bmatrix}\begin{Bmatrix} T_1 \\ T_2 \\ T_4 \\ T_5 \end{Bmatrix}$$

$$+\begin{bmatrix} \left(M_{11}^1+M_{33}^3\right) & M_{12}^3 & M_{32}^2 & \left(\quad+M_{13}^2\right) & M_{13}^2 \\ M_{21}^1 & \left(M_{22}^1+M_{11}^3+M_{33}^4\right) & 0 & \left(\quad+M_{23}^1\right) & M_{23}^4 \\ M_{23}^2 & 0 & \left(M_{22}^2+M_{11}^5+M_{33}^6\right) & \left(\quad+M_{21}^2\right) & M_{21}^5 \\ \left(M_{31}^1+M_{13}^3\right) & \left(M_{32}^1+M_{23}^4\right) & \left(M_{12}^2+M_{21}^5\right) & M_{33}^1+M_{22}^4+M_{11}^7+M_{33}^8 & M_{31}^5+M_{13}^7 \end{bmatrix}\begin{Bmatrix} T_{11} \\ T_{12} \\ T_{13} \\ T_{14} \\ T_{15} \end{Bmatrix}=\begin{Bmatrix} FF_1^1+FF_3^2 \\ FF_2^1+FF_1^3+FF_3^4 \\ FF_2^2+FF_1^5+FF_3^6 \\ FF_3^1+FF_1^2+FF_2^4+FF_2^5+FF_1^7+FF_3^8 \end{Bmatrix}$$

(22)

Where;

$$\begin{Bmatrix} FF_1^1+FF_3^2 \\ FF_2^1+FF_1^3+FF_3^4 \\ FF_2^2+FF_1^5+FF_3^6 \\ FF_3^1+FF_1^2+FF_2^4+FF_2^5+FF_1^7+FF_3^8 \end{Bmatrix}=\begin{Bmatrix} F_1^1+F_3^2 \\ F_2^1+F_1^3+F_3^4 \\ F_2^2+F_1^5+F_3^6 \\ F_3^1+F_1^2+F_2^4+F_2^5+F_1^7+F_3^8 \end{Bmatrix}-\begin{bmatrix} 0 & 0 & 0 & 0 & 0 \\ K_{12}^3 & \left(K_{13}^3+K_{31}^4\right) & 0 & 0 & 0 \\ 0 & 0 & K_{32}^6 & \left(K_{13}^5+K_{31}^6\right) & 0 \\ 0 & \left(K_{21}^4+K_{12}^7\right) & 0 & \left(K_{23}^5+K_{32}^8\right) & \left(K_{13}^7+K_{31}^8\right) \end{bmatrix}\begin{Bmatrix} T_o \\ T_o \\ T_o \\ T_o \\ T_o \end{Bmatrix}$$

$$-\begin{bmatrix} 0 & 0 & 0 & 0 & 0 \\ M_{12}^3 & \left(M_{13}^3+M_{31}^4\right) & 0 & 0 & 0 \\ 0 & 0 & M_{32}^6 & \left(M_{13}^5+M_{31}^6\right) & 0 \\ 0 & \left(M_{21}^4+M_{12}^7\right) & 0 & \left(M_{23}^5+M_{32}^8\right) & \left(M_{13}^7+M_{31}^8\right) \end{bmatrix}\begin{Bmatrix} T_o \\ T_o \\ T_o \\ T_o \\ T_o \end{Bmatrix} \tag{23}$$

3. Results and Discussion

With a domain for the analysis of axial depth z $=3.5\times10^{-6}$ meters and radius R= 25×10^{-6} meters and using the parameters in Table 1, using Alpha family of approximation the computed results are tabulated and shown graphically.

Table 1: *Parameters used for the analysis*

Parameters	Value
Gaussian Parameter a	120000^{-1} I/m
Ambient temperature T_o	298 K
Thermal conductivity k	52 W/(mK)
Reflectivity r_f	0.9
Density ρ	7836kg/m^3
Absorption coefficient δ	6.16×10^7 I/m
Specific heat capacity C_p	330 J/kgK
Laser peak power intensity I_o	1×10^{13} W/m^2

Substituting the above parameters in Table 1 and the element size into (13), (14) and (15) to obtain the M, K and f element matrix for each of the elements making up the assembly as shown in Fig. 1 and Fig. 2 respectively.

For the Finite Element Analysis of the two dimensional time dependent partial differential equation, the solution comprises of two parts viz the semi discrete spatial approximation and the time approximation. For the semi discrete spatial approximation, uniform rectangular Lagrange interpolation functions were used to obtain the finite element model. Due to the rapid heating process, time spent during change of state (solid and liquid state) of the steel was assumed to be negligible and an average value of thermal conductivity k and specific heat capacity c_p was used for both states. Alpha α family of Approximation was used in the time analysis and the time step used was made as small as possible to improve the accuracy of the results. The accuracy of the method used in our analysis depends on the mesh discretization for the spatial approximation, and also the time step used for the time approximation. Highly accurate results are gotten from discretization with larger number of elements and smaller time step. To achieve this discretization a Finite Element Computer Programme is usually necessary. Table 2 and Table 3 shows the results of our computation of temperature values for 6 nano seconds using a discretization of 100 rectangular elements and 200 Triangular elements respectively. However with the computer programme developed we went further to discretized the domain using 2000 rectangular elements and 4000 triangular elements and the results were plotted alongside the results of [14] in Fig. 3 to 18. Fig. 3 to Fig. 10 shows comparison of temperature distribution along the *z*-axes at some specified radial positions inside the substrate material for four different heating periods Fig. 11 to Fig. 18shows comparison of temperature distribution along the r-axes at some specified axial positions inside the substrate material for four different heating periods. From the Figures, the temperature values increases as the time of irradiation is increased, but at relatively high distance away from the surface (at depth close to 3.5μm and radius close to 25μm) the temperature variation with time is minimal as it is almost constant and this conforms to the boundary conditions of (5) and (6). At early heating periods of about 6ns, evaporation of the surface in the region of the irradiated spot centre begins and as the time period progresses, the cavity is formed in the surface vicinity of the substrate material. This is due to the laser power intensity distribution across the irradiated spot, which is Gaussian and energy absorbed from the irradiated field is unidirectional and along the axial direction. This in turn results in higher temperature gradients in the axial direction than that of the radial direction. As the depth below the surface increases towards the solid bulk, temperature decay becomes gradual. This occurs because of the energy balance attained between the internal energy gain from the irradiated field and diffusional energy transfer to solid bulk from the surface region [14].

For the laser model equation analyzed in (1), it was assumed that the thermal conductivity k and specific heat capacity c_p are constant and do not depend on the temperature of the irradiated material, but in reality it varies as the temperature increases as well as during phase change as the material changes from solid to liquid and then to vapor. However, these variations were not incorporated into the solution. Again it was assumed that the substrate material has sharp melting and boiling temperatures of 1880^{o}C and 3030^{o}C respectively, but during the laser heating, phase-change occurs.

Table 2: *Temperature values in Kelvin after 6 nano seconds using 100 rectangular element mesh*

Axial Depth (micro meters)	Radius (micro meters)										
	0.00	2.50	5.00	7.50	10.00	12.50	15.00	17.50	20.00	22.50	25.00
3.50	298.00	298.00	298.00	298.00	298.00	298.00	298.00	298.00	298.00	298.00	298.00
3.15	298.01	298.00	298.00	298.00	298.00	298.00	298.00	298.00	298.00	298.00	298.00
2.80	297.98	297.98	297.99	297.99	298.00	298.00	298.00	298.00	298.00	298.00	298.00
2.45	297.97	297.97	297.98	297.99	297.99	298.00	298.00	298.00	298.00	298.00	298.00
2.10	298.52	298.47	298.36	298.23	298.12	298.05	298.02	298.01	298.00	298.00	298.00
1.75	297.33	297.40	297.54	297.71	297.85	297.93	297.98	297.99	298.00	298.00	298.00
1.40	285.65	286.87	289.54	292.67	295.20	296.78	297.56	297.87	297.97	297.99	298.00
1.05	323.38	320.86	315.39	308.98	303.78	300.53	298.92	298.28	298.07	298.02	298.00
0.70	825.21	773.30	659.12	525.71	417.45	350.08	316.87	303.68	299.42	298.31	298.00
0.35	2875.80	2622.80	2063.50	1410.40	880.92	551.81	389.83	325.61	304.88	299.49	298.00
0.00	7595.10	6881.90	5295.00	3443.60	1944.40	1013.80	556.52	375.57	317.28	302.18	298.00

Table 3: *Temperature values in Kelvin after 6 nano seconds using 200 triangular element mesh*

Axial Depth (micro meters)	Radius (micro meters)										
	0.00	2.50	5.00	7.50	10.00	12.50	15.00	17.50	20.00	22.50	25.00
3.50	298.00	298.00	298.00	298.00	298.00	298.00	298.00	298.00	298.00	298.00	298.00
3.15	298.07	297.80	298.22	298.16	297.80	297.90	298.00	298.03	298.03	298.01	298.00
2.80	298.41	297.21	298.23	298.76	297.93	297.75	297.84	297.94	298.01	298.03	298.00
2.45	299.84	295.80	297.14	299.64	298.84	298.10	297.82	297.79	297.88	297.96	298.00
2.10	305.71	293.65	292.45	298.65	300.02	299.46	298.67	298.11	297.92	297.91	298.00
1.75	328.96	296.58	281.89	289.96	296.55	299.27	299.66	299.03	298.43	298.11	298.00
1.40	414.59	336.76	280.54	273.29	281.41	290.23	295.86	298.01	298.36	298.23	298.00
1.05	698.48	531.72	380.85	303.26	278.51	278.86	286.91	293.35	296.52	297.66	298.00
0.70	1518.90	1198.90	873.61	594.65	419.58	333.32	302.82	296.35	296.58	297.40	298.00
0.35	3532.00	2969.80	2348.90	1592.20	982.21	599.38	408.44	331.56	306.44	299.72	298.00
0.00	3696.90	4128.50	3462.00	2384.40	1440.50	819.70	497.06	361.49	314.93	301.81	298.00

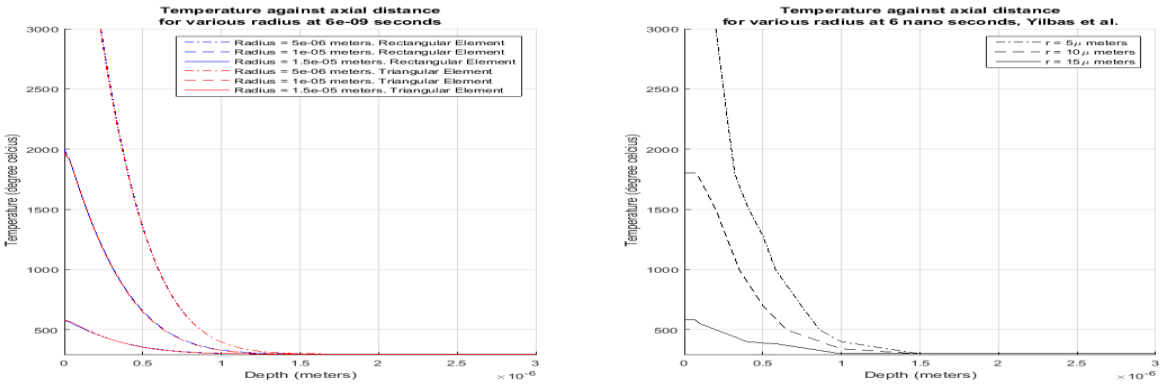

Fig. 3: *Temperature against axial distance at time 6 nano seconds (Comparison between this work and that of Yilbas et al. [13-15])*

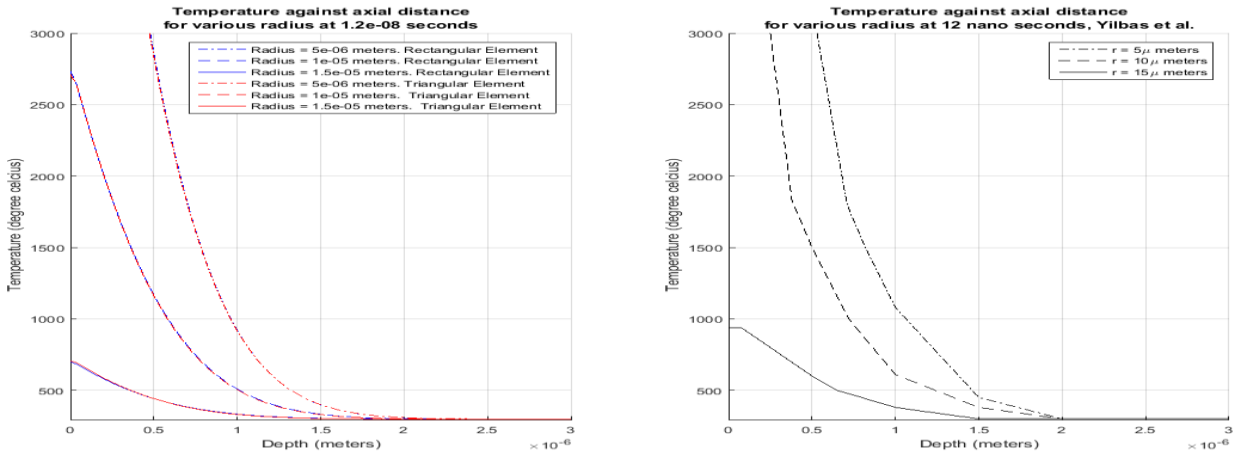

Fig. 4: *Temperature against axial distance at time 12 nano seconds (Comparison between this work and that of Yilbas et al. [13-15])*

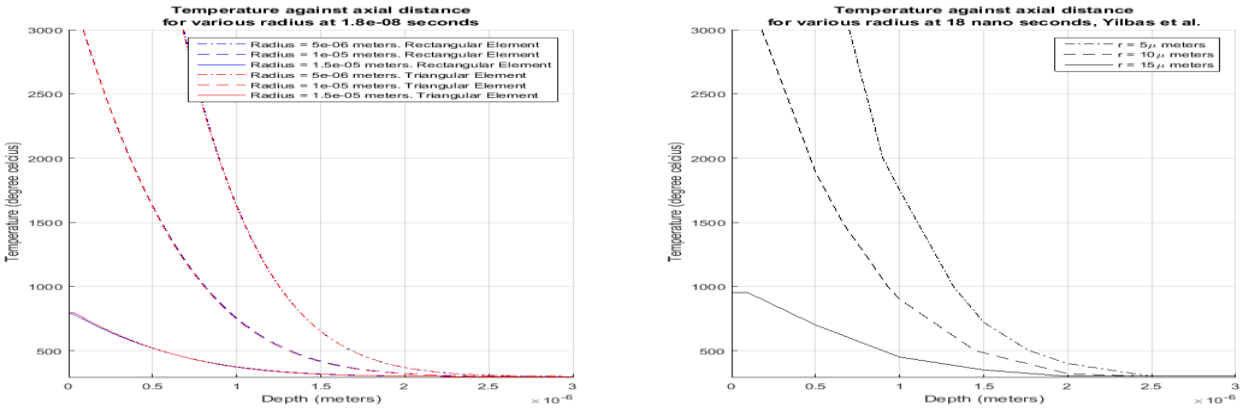

Fig. 5: *Temperature against axial distance at time 18 nano seconds (Comparison between this work and that of Yilbas et al. [13-15])*

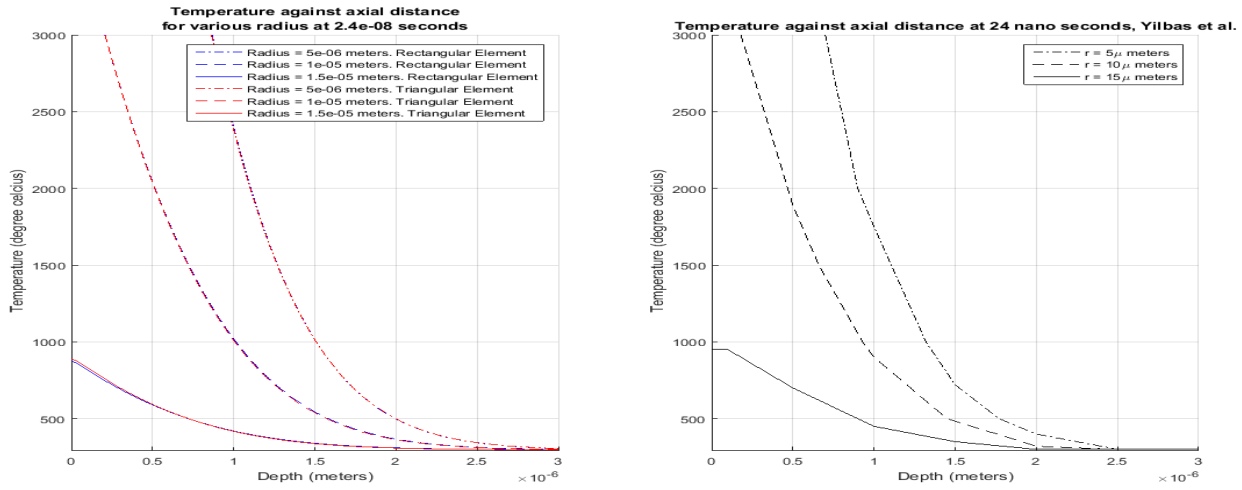

Fig. 6: *Temperature against axial distance at time 24 nano seconds (Comparison between this work and that of Yilbas et al. [13-15])*

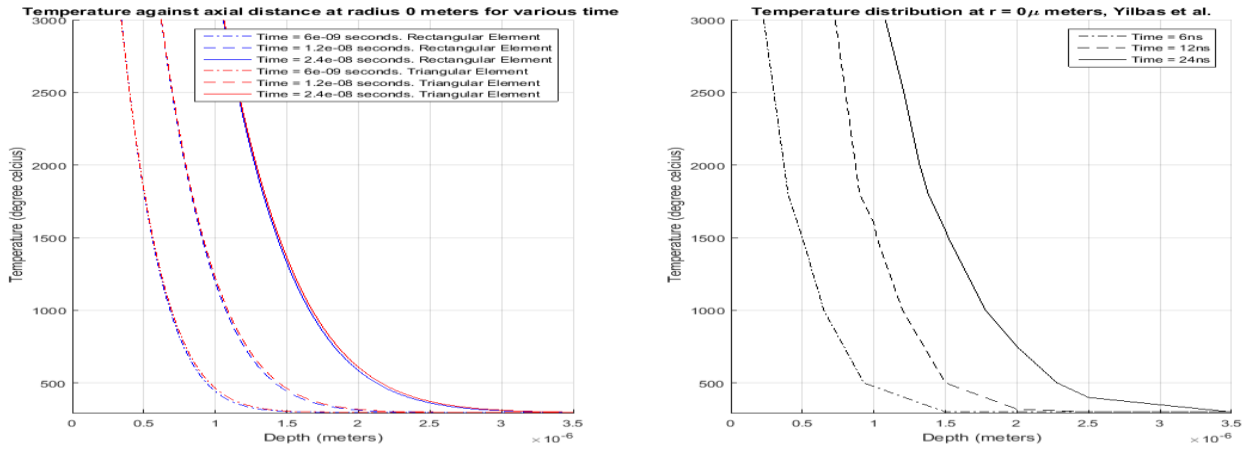

Fig. 7: *Temperature against axial distance for radius 0 micro meters (Comparison between this work and that of Yilbas et al [13-15])*

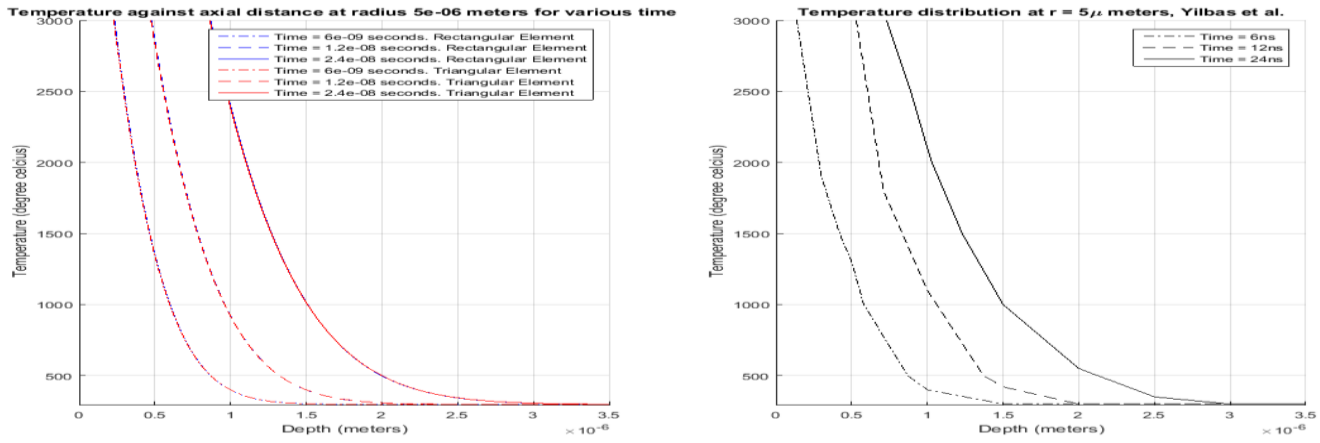

Fig. 8: *Temperature against axial distance for radius 5 micro meters (Comparison between this work and that of Yilbas et al [13-15])*

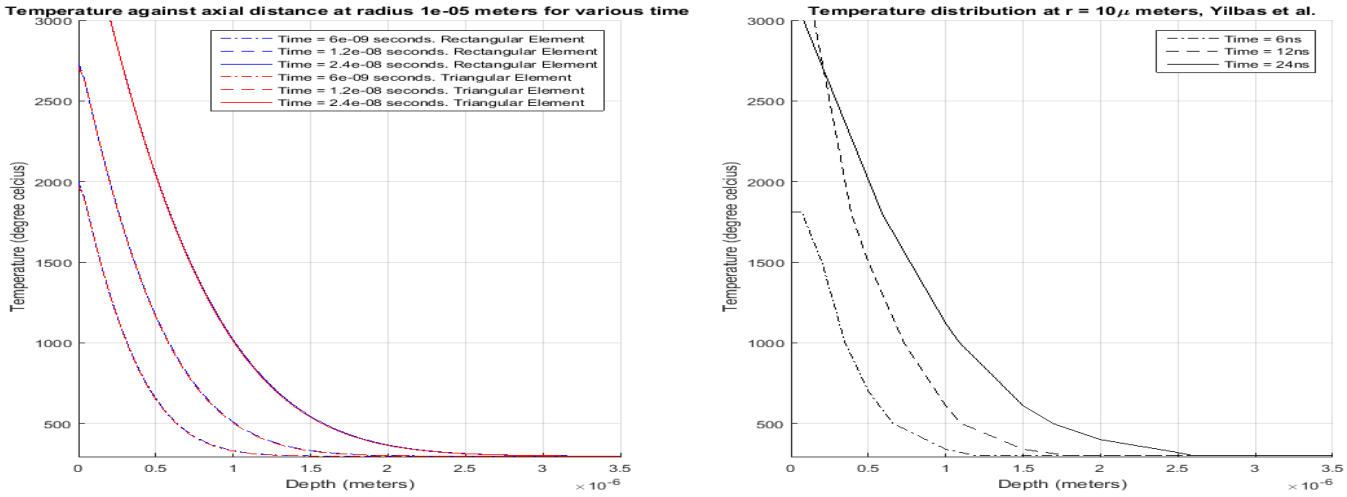

Fig. 9 *Temperature against axial distance for radius 10 micro meters (Comparison between this work and that of Yilbas et al [13-15])*

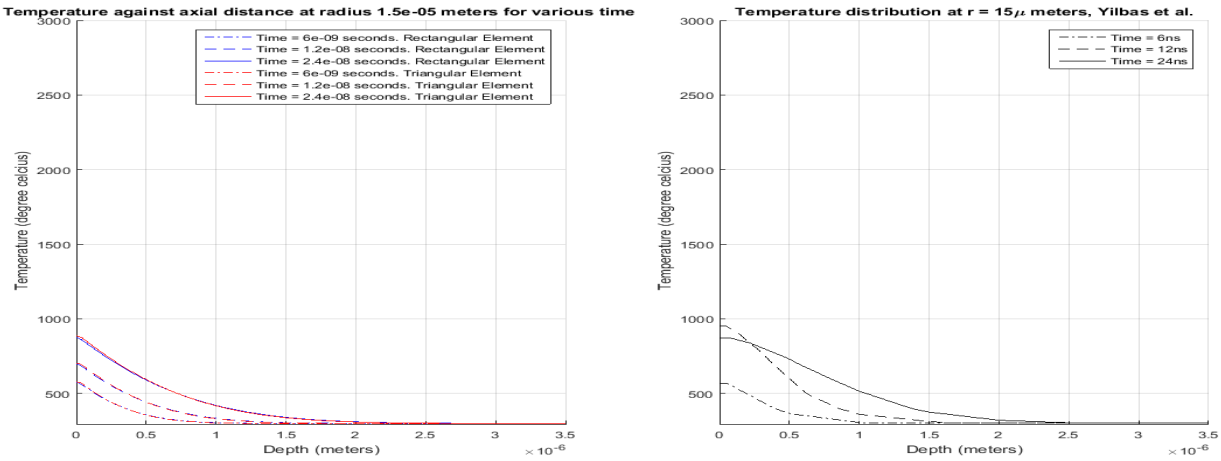

Fig. 10: *Temperature against axial distance for radius 15 micro meters (Comparison between this work and that of Yilbas et al[13-15])*

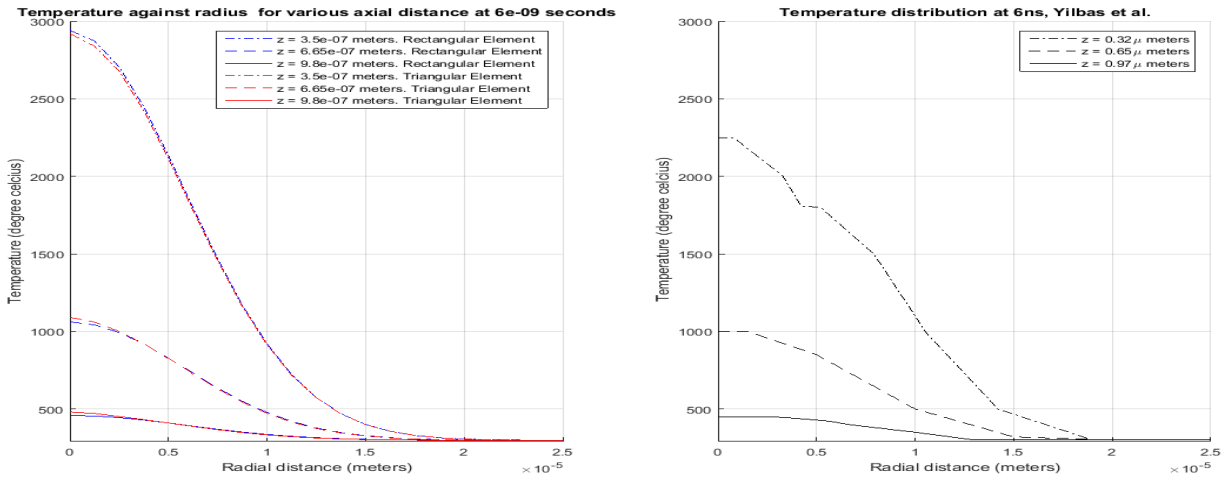

Fig. 11: *Temperature against radius at time 6 nano seconds (Comparison between this work and that of Yilbas et al. [13-15])*

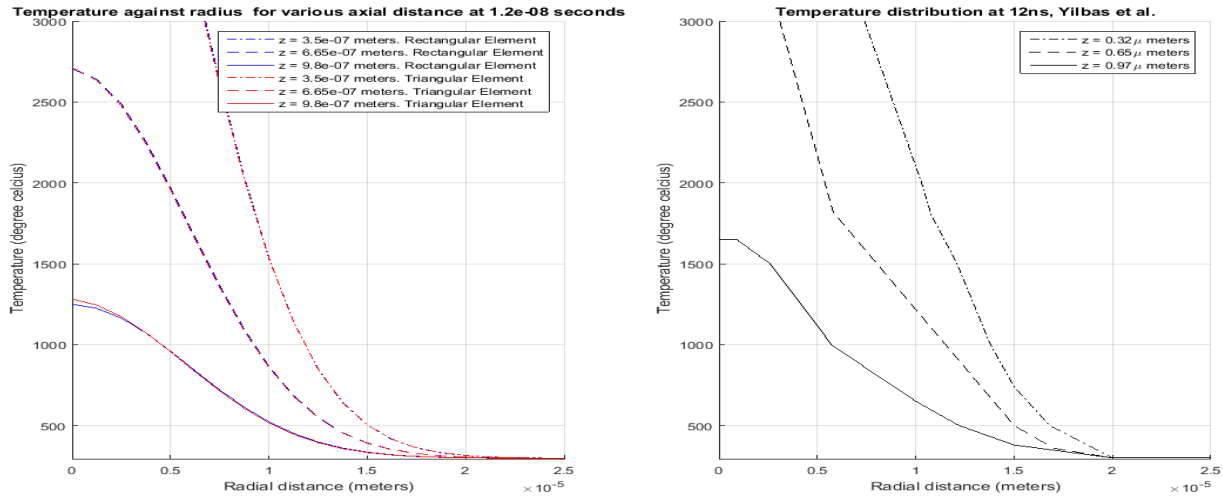

Fig. 12: *Temperature against radius at time 12 nano seconds (Comparison between this work and that of Yilbas et al. [13-15])*

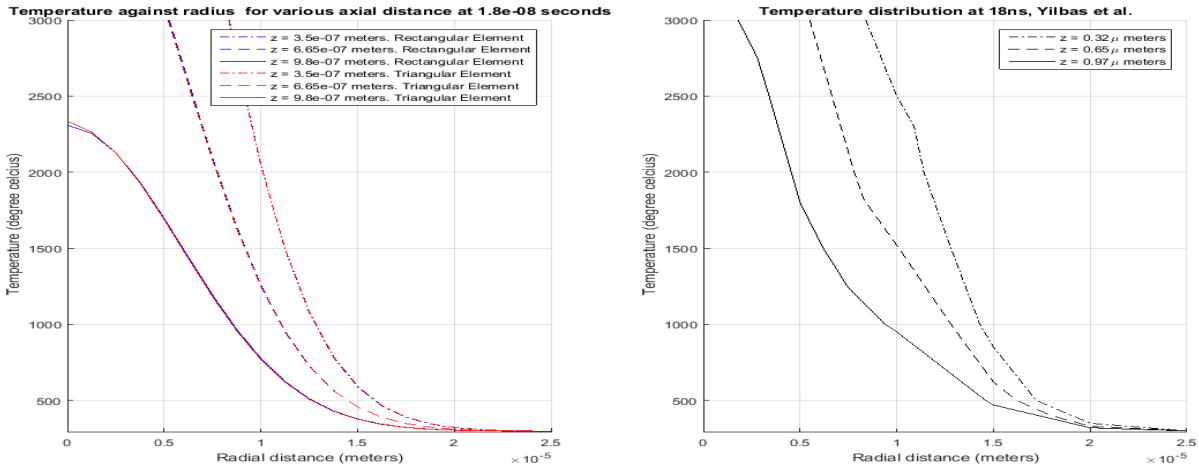

Fig. 13: *Temperature against radius at time 18 nano seconds. (Comparison between this work and that of Yilbas et al. [13-15])*

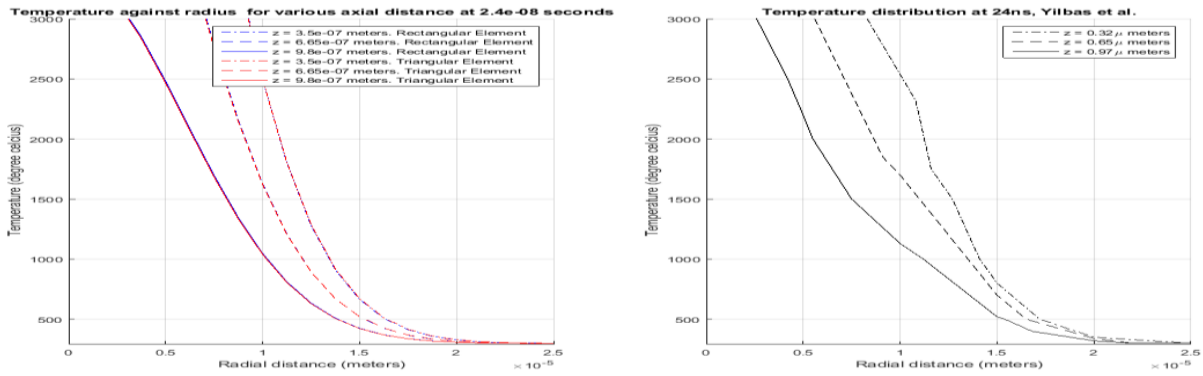

Fig. 14: *Temperature against radius at time 24 nano seconds (Comparison between this work and that of Yilbas et al. [13-15])*

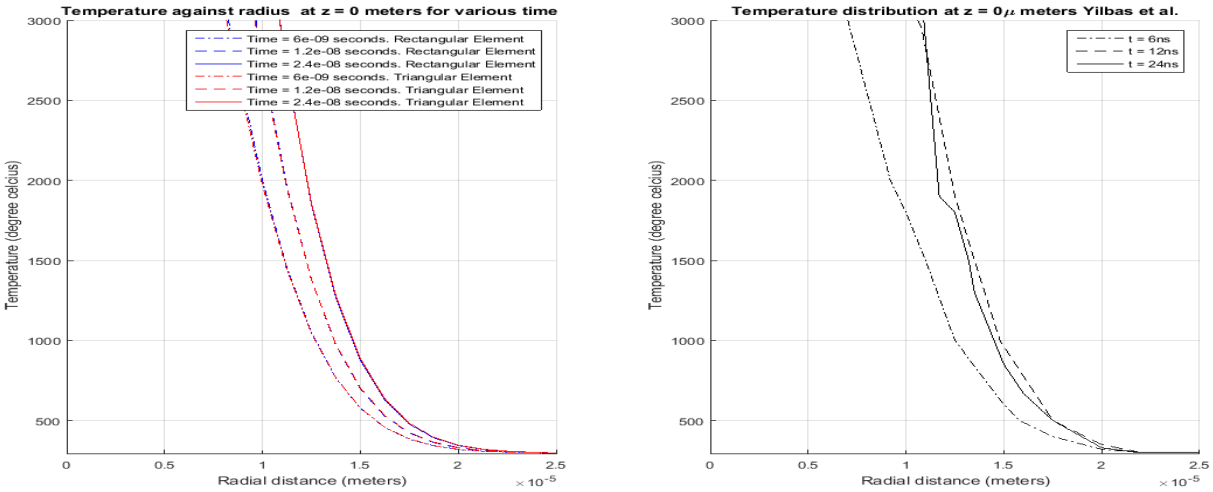

Fig. 15: *Temperature against radius at axial distance of 0 micro meters. (Comparison between this work and that of Yilbas et al. [13-15])*

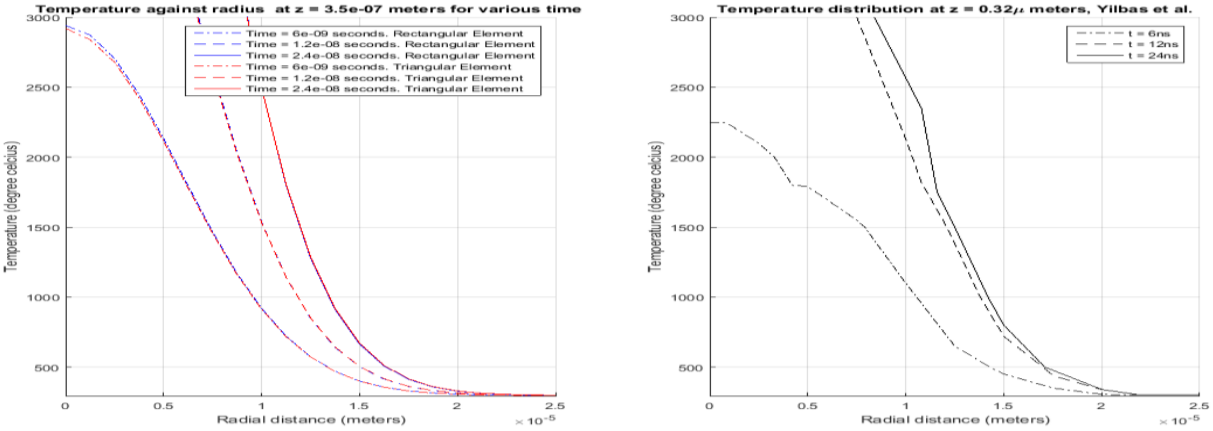

Fig. 16: *Temperature against radius at axial distance of 0.35 micro meters (Comparison between this work and that of Yilbas et al. [13-15])*

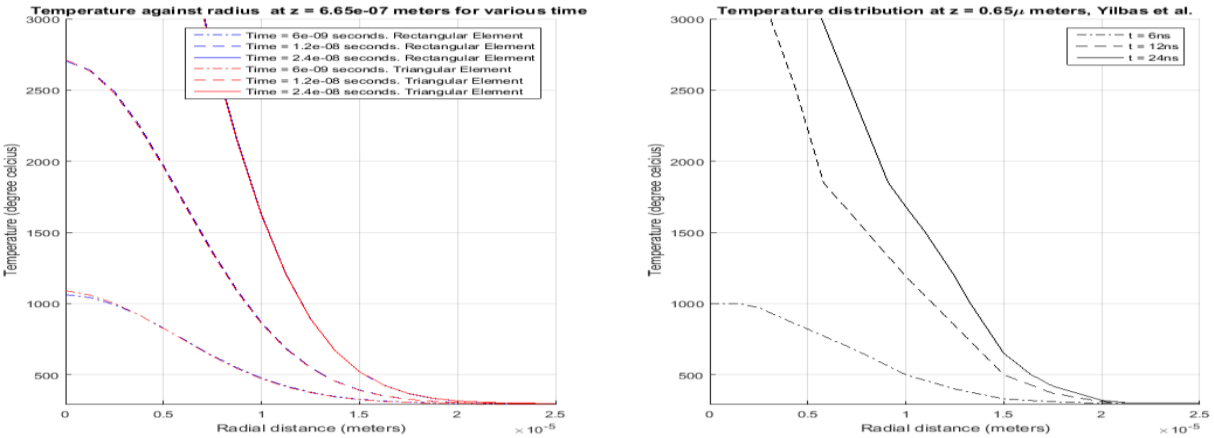

Fig. 17: *Temperature against radius at axial distance of 0.665 micro meters. (Comparison between this work and that of Yilbas et al. [13-15])*

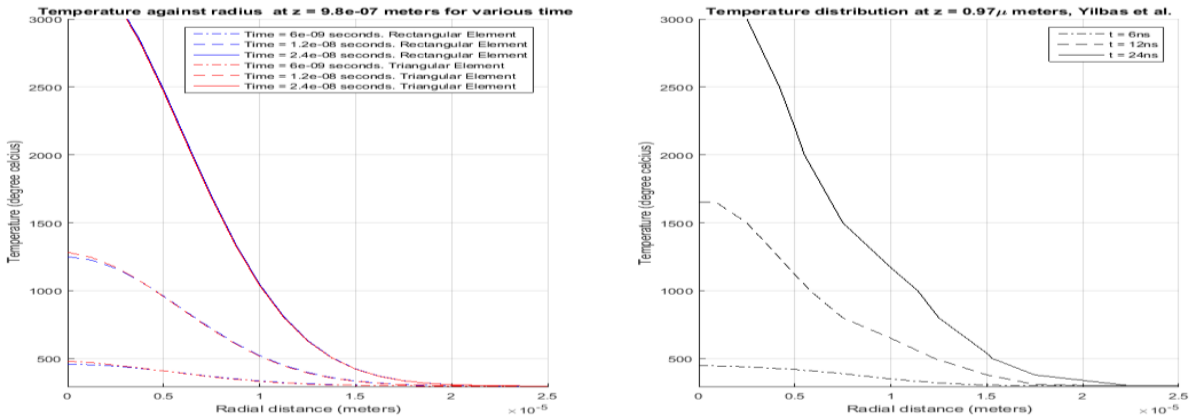

Fig. 18: *Temperature against radius at axial distance of 0.98 micro meters(Comparison between this work and that of Yilbas et al.[13-15])*

To accommodate the phase change process, a mushy zone is created and it should be considered if actual heating model is to be fully considered. That is, the Laser heating equation should be modified. For the modification an energy (or enthalpy) method can be used. In the enthalpy method, the governing equation of energy transport can be written in terms of an enthalpy equation. Once the phase change initiates, a mushy zone (partially solid and partially liquid or partially liquid and partially vapor) can be generated across the interface where the phase change occurs. During the phase change process, the temperature of the substrate material remains the same, but its enthalpy changes in this region. This can be formulated after considering the energy balance in the mushy zone, [14].

Conclusion

The Laser heating equation (1) has been successfully solved using Finite Element Method a numerical method as against the analytical. It can therefore be concluded that the Finite Element Method is capable of adequately and accurately predicting the temperature distribution in the irradiated material, With its accuracy increasing as we increase the number of Finite Elements discretization, Such that using a mesh discretization up to 2000 rectangular elements and 4000 triangular elements by the help of the MATLAB program developed we have results that were highly accurate as seen from the graphs. The Finite Element procedures used in the analysis can be applied to all similar Laser heat equations by simply substituting appropriate parameters and boundary conditions into the formulated coefficient matrix equation in the MATLAB Finite Element program developed.

References

[1] D S Burnett., *Finite Element Analysis, from Concept to Application.* Addison Wesley, New Jersey, 1987.

[2] J.N. Reddy, *An Introduction to the Finite Element Method*. Third ed. McGraw-Hill. 2006.

[3] J.A. Akpobi, and E.D., Akpobi. "A finite element analysis of the distribution of velocity in viscous incompressible fluids using the Lagrange interpolation function", *Journal of Applied Science*, vol.11, pp.31-38, 2007.

[4] J.A. Akpobi, and E.D., Akpobi. "Finite element solution of the Boussinesq wave equation", *Journal of the Nigeria association of Mathematical physics*, vol.11, pp. 223-228. 2007.

[5] H. Shokouhmand and S.M.A. Noori., "Finite element analysis of mixed convection heat transfer through a vertical wavy isothermal channel", *proceedings of the world congress on Engineering*, vol. 2, pp. 1415-1420, 2010.

[6] R. Rajamani, C. Srinivas, and K. N. Seetharamu, "Finite Element Analysis of convective Heat transfer in porous media", *International journal for Numerical Methods in Fluids*. Vol.11 (3), pp. 331-339, 1990.

[7] Johan Meijer,."Laser beam machining (LBM), state of the art and new opportunities", *Journal of Materials Processing Technolog* vol. 149 pp. 2–17, 2004.

[8] U. Paek, and F. P. Gagliano "Thermal analysis of laser drilling", *Journal of Quantum Electronics*, vol.8, pp.112-119, 1972.

[9] X.Liu, D. Du, and G. Mourou, " Laser ablation and micro machining with ultrashort laser pulses, Journal of Quantum Electron. Vol. 33, pp. 1706-1716, 1997.

[10] M. F. Modest and H. Abiakans, "Evaporative cutting of a semi-infinite body with a moving cw laser", *Journal of Heat Transfer*, vol. 108 pp. 602-607, 1988.

[11] P. S. Wei and J. Y. Ho, Energy consideration in high energy beam drilling, International Journal of Heat and Mass Transfer, vol. 33, pp. 2207-2217, 1990.

[12] S.Y. Bang and M. F. Modest, "Multiple reflection effects on evaporative cutting with a moving cw laser", *Journal of Heat Transfer*, vol. 113, pp. 663-669, 1991.

[13] B. S. Yilbas and I. Z. Naqvi, "Laser heating including the phase change process and thermal stress generation in relation to drilling", *Journal of Engineering Manufacture*, vol. 217(B) pp. 977-991, 2003.

[14] B. S. Yilbas, M. Saad, and S. Z. Shuja, "Laser pulse heating: modelling of cavity formation", *Journal of Mechanical Engineering Science*, vol. 221(C) pp. 307-328, 2006.

[15] B. S. Yilbas, "Analytical solution for time unsteady laser pulse heating of semi-infinite solid", *International journal of Mechanical Science*, vol. 39(6), pp. 671-682, 1997.

International Journal of Computational and Experimental Science and ENgineering (IJCESEN)
Vol. 6-No.2 (2020) pp. 122-126
http://.dergipark.org.tr/en/pub/ijcesen
ISSN: 2149-9144

Research Article

Mechanism of Using Dilute Microemulsion System (DMS) on Enhancing Hydrocarbon Production from Low Permeability Reservoirs

Xingyuan LIANG[1*], Fujian ZHOU[1], Tianbo LIANG[1], Bo ZHENG[2]

[1]China University of Petroleum, Beijing Unconventional Oil and gas Scientific and Technology Department, 102249, Beijing-China
[2]TUHA Oilfield Downhole Operation Company, 838200, Shansahn-China

* **Corresponding Author** : lxypetro@163.com
ORCID: 0000-0002-7583-3969

Article Info:

DOI: 10.22399/ijcesen.588096
Received : 07 July 2019
Accepted : 13 July 2020

Keywords

Imbibition
Unconventional reservoirs
Nanofluid

Abstract:

Dilute microemulsion system (DMS) can reduce the adsorption of surfactants on the rock surface, and it has been widely used as fracturing fluid additive for low permeability reservoirs in recent years. In some cases, it can reduce the water block caused by the invaded fracturing fluid and enhance the hydrocarbon production rate; while in some cases, it cannot. Although a few theories and models have been proposed to explain this discrepancy, it is still unclear (1) when DMS can enhance the hydrocarbon production, and (2) the impact of using DMS on hydraulic fracturing, flowback, and production. In this study, the imbibition test, contact angle test, and core flooding experiment were conducted to explore the answers to the above questions. Results from imbibition cell tests and contact angle measurements indicate our DMS can alter rock wettability from oil-wet to water-wet within half a day, but it cannot alter water-wet originally rocks. In core flooding experiments, the invasion step shows that the relative permeability to water is reduced after using DMS, suggesting DMS can reduce the forced water invasion during hydraulic fracturing; the flowback step shows that 0.1wt% DMS can reduce the water block and enhance the production rate by 12% comparing to the brine.

1. Introduction

The unconventional reservoir has become the vital part of the fossil energy. Although the permeability and porosity are low, the volume is so large that the original oil in place is giant [1]. Horizontal well and staged fracturing are the main technologies to exploit the oil. However, the production decreases fast, and the oil recovery is only about 5%-10%. The reason is that the reservoir is so tight that the energy decreases quickly [2]. Besides, the wettability of the reservoir is another critical factor [3,4]. The reservoir would tend to be oil-wet, after contact with the oil for a long period, because the surfactant in the oil would adsorb onto the stone, which would alter the wettability of reservoir. For tight reservoir, the imbibition is an essential mechanism of recovery, and if fracturing fluid can alter the oil-wet reservoir into the water –wet reservoir, the imbibition would happen, then the oil recovery would be enhanced a lot [5,6]. Surfactant and nanofluid have been added into fracturing fluid, which can help change the wettability of the reservoir [7]. Although kinds of surfactant have been used in the low permeability reservoir, the effect is unsatisfactory. The reason is that the surfactant is easier to adsorb onto the stone, which would reduce the effective area [8]. As a new fracturing additive, DMS has been widely used in the low permeability reservoir, which has shown that the DMS can improve the production at different levels [9]. However, the mechanism of

using DMS on enhancing production from low permeability reservoirs hasn't been figured out. In this paper, several experiments have been conducted to answer the question. Amott test and contact angle test were used to prove the wettability alteration, core flooding test can be used to justify the higher production and less water block after using the DMS.

2. Material and Procedure

Rock properties: The permeability to water is 0.7mD, the porosity is 0.135, and rock is taken at an outcrop, and its main mineral is dolomite.

Dilute Microemulsion System (DMS): The average diameter of DMS is 15 nm, the test result is listed as Fig1, the interfacial tension (IFT) of 0.1wt% DMS is 3mN/m. Adsorption is 3 mg/g. the core of DMS is oil phase, and the surfactant adsorbs on the oil phase.

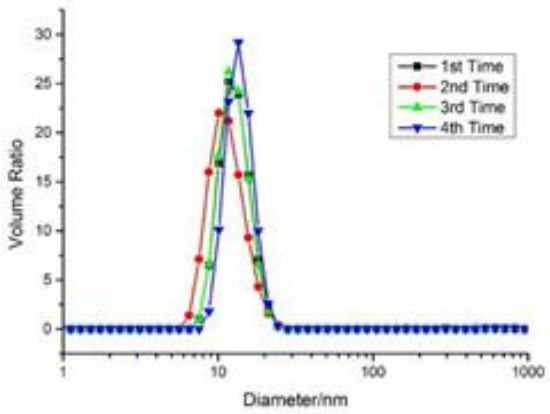

Fig 1. *Diameter distribution of DMS*

Amott cell: The cell (Fig 2) can hold a cylindrical rock core with 6cm length, the precision is 0.02ml, the maximum range is 2ml. A white cover put on the top of the cell is prevented the liquid from evaporation. A thin tube in the middle of cell can measure the variation of the oil-water boundary. The power of imbibition is the capillary force. If the stone is water wet, after putting the core into the water, the imbibition will happen, and the oil-water boundary will change, because the water would replace oil out; on the contrary, if the stone is oil wet, the capillary force is resistance, the imbibition wouldn't happen, the oil-water boundary still unchanged.

Contact angle equipment: the equipment can test the contact angle between solid surface and liquid (Fig 3).

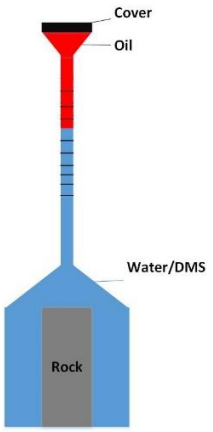

Fig 2. *Schematic diagram of Amott cell*

The test method is dropping a droplet on the solid surface, and the high precision camera can record the image of a droplet. We can adjust the camera until the droplet is clear enough. Computer screen would show the picture of a droplet. Then the contact angle between solid and surface would be tested through software. Because of different wettability, the contact angle between liquid and solid is different. If the contact angle between water and solid is larger than 105°, the solid is oil-wet; if the contact angle is between 75° to 105°, the solid is middle wet; if the contact angle is smaller than 75°, the solid is water wet.

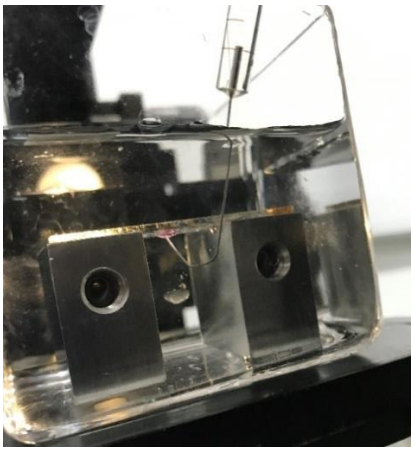

Fig 3. *Contact angle test*

Core Flooding System: The core flooding system (Fig 4) consists of 5 parts: pump system, the power system is a 100DX ISCO pump. The flow rate is from 0.00001cc/min-50ml/min, and the highest flooding pressure is 10000 psi. There are three containers which can fill in the water, DMS and kerosene. Their loading capacity is 10000psi. Five pressure transducers are loaded to monitor the pressure; the precision is 0.058psi. Core with different length is loaded in the core holder, the diameter of core is 2.54cm (1 inch). A hand pump loads confining pressure.

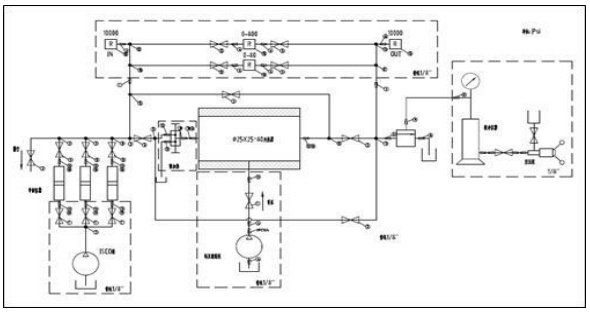

Fig 4. *Schematic diagram of the core flooding system*

Procedure:

Imbibition test:

①To change the wettability of carbonate rocks, the cores were flooded 10PV by the 1.5% oleic acid with kerosene, after that the cores were flooded with kerosene, the aim is to displace the oleic acid out in case the oleic acid influence the experiment.

②Testing the contact angle of rock, making sure the rock has become oil-wet.

③putting the core A into Amott cell and the loaded the distill water with 2wt%KCl until the water reaches the scale line of cell; putting the core B into Amott cell, and the loaded the 0.1wt% DMS until the water reaches the scale line of cell.

④recording the oil-water boundary with different time. At the start period, the interval time is 20min, after 2 hours, the interval is 1hr until the oil-water boundary doesn't change.

Core flooding experiment:

①To change the wettability of carbonate rocks, the cores were flooded 10PV by the 1.5% oleic acid with kerosene, after that the cores were flooded with kerosene, the aim is to displace the oleic acid out in case the oleic acid influence the experiment.

②0.1wt.%DMS was injected into the core reversely, which mimicked the fracturing fluid. And the fluid without the DMS was taken as the control group.

③At the end, the kerosene floods through the rock from the opposite direction. During the experiment, the pressure difference and volume of water and oil are supervised. The flow rate of the whole process is 0.05ml/min.

3. Result and Discussion

Spontaneous imbibition oil production

The imbibition test result shows that the core A immersed in the 0.1wt% DMS replace more oil than core B immersed in the fluid without the DMS. At the beginning of the imbibition test, oil-water boundary changes fast, after 1 hour, the oil-water boundary gradually unchanged (Fig 5). On the contrary, the core immersed with the core B, the oil-water boundary early keeps constant. The result proved that the DMS could alter the oil wet into water wet, because the oil was replaced by the water, and the capillary is the power. The more oil was replaced by the water; the water-wet properties are stronger. For core B, the core is oil-wet, the capillary is the resistance, and the water cannot enter the pore and replace the oil out. Therefore, the oil-water boundary in the cell is unchanged. The similar liquid called nanofluids has been proved to enhance the oil recovery through Amott cell [4].

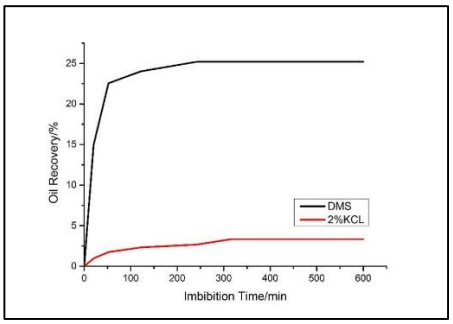

Fig 5. *The imbibition curve with two kinds of liquids*

Contact angle test

After flooded by the oleic acid, the average contact angle of core A is 145°， the average contact angle of core B is 143°. After the imbibition test, the average contact angle of core A is 65°, which proves that the core A is water-wet. This is because the DMS adsorb on the surface of a rock, and change the rock's wettability. The average contact angle of core B is 120°, which proves that the core B is still oil-wet. As shown in fig 6 and fig 7. Alvarez and Schechter has used the contact angle experiments to prove the anionic, nonionic surfactant, and complex nanofluid can alter the oil-wet to water-water at different levels [8]. Liang et al. also used the contact angle experiments to prove the liquid nanofluid can alter the oil-wet to water-water in the tight oil reservoir [5].

Core flooding test

The results show that the oil relative permeability with DMS is 12% higher than brine (Fig 8), which proves that the DMS can reduce the water invasion. The result also indicates that the core displaced with DMS has tended to water wet.

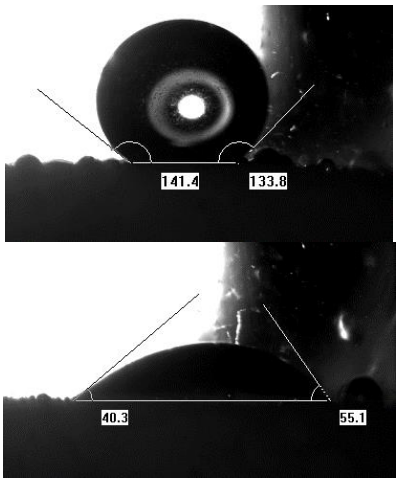

Fig 6. *Before and after submersed into the DMS*

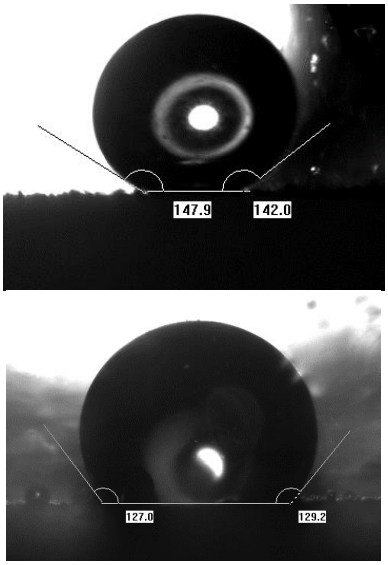

Fig 7. *Before and after submersed into the 2%KCl*

Because the relative permeability of the wetting phase is lower according to the relative permeability curve. At the third step, the pressure with DMS decreases fast, which state the core tends to water wet. On the contrary, the pressure with 2%KCl stays high, which demonstrates the core is still oil wet. The fracturing fluid loss into the reservoir can damage the reservoir and decrease the production. To asset the flow back rate, the effluent is also collected. The core displaced with DMS collected 0.15PV more water than brine at last. The result shows that the DMS can dissipate the lost fracturing fluid into the matrix and improve the flow back. Liang et al. have used the core flooding system with a surfactant to study the wettability alteration in low permeability [2].

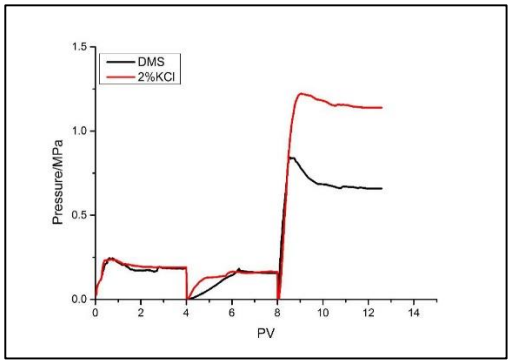

Fig 8. *Pressure variation during the flooding process*

4. Conclusion

Based on the experimental study, we propose the mechanisms of using DMS on enhancing the flowback and oil production, especially from oil-wet reservoirs. Meanwhile, we reveal the potentials of using DMS on (1) controllable altering rock wettability from oil-wet to water-wet (2) reducing water invasion and thus enlarging the fracture area. Our results also provide a criterion on screening/optimizing DMS for fracturing low permeability reservoirs.

Notes

The authors declare that they have no conflict of interests.

Acknowledgments

This work is financially supported by the PetroChina Innovation Foundation (2018D-5007-0205), the National Science and Technology Major Projects of China (2016ZX05051 and 2017ZX05030).

REFERENCES

[1] He, Y., Cheng, S., Li, S., Huang, Y., Qin, J., Hu, L., Yu, H., (2017). A Semianalytical Methodology To Diagnose the Locations of Underperforming Hydraulic Fractures Through Pressure-Transient Analysis in Tight Gas Reservoir. SPE J. 22, 924–939. https://doi.org/10.2118/185166-PA

[2]Liang, T., Luo, X., Nguyen, Q., DiCarlo, D.A., (2017a). Computed-Tomography Measurements of Water Block in Low-Permeability Rocks: Scaling and Remedying Production Impairment. SPE J. https://doi.org/10.2118/189445-PA

[3] Liang, T., Achour, S.H., Longoria, R.A., DiCarlo, D.A., Nguyen, Q.P., (2016). Identifying and Evaluating Surfactant Additives to Reduce Water Blocks after Hydraulic Fracturing for Low Permeability Reservoirs. Presented at the SPE Improved Oil Recovery Conference, Society of Petroleum Engineers. https://doi.org/10.2118/179601-MS

[4] Penny, G.S., Zelenev, A., Lett, N., Paktinat, J., O&apos, Neil, B.J., (2012a). Nano Surfactant System Improves Post Frac Oil and Gas Recovery in

Hydrocarbon Rich Gas Reservoirs. Presented at the SPE Improved Oil Recovery Symposium, Society of Petroleum Engineers. https://doi.org/10.2118/154308-MS

[5] Liang, T., Li, Q., Liang, X., Yao, E., Wang, Y., Li, Y., Chen, M., Zhou, F., Lu, J., (2018). Evaluation of liquid nanofluid as fracturing fluid additive on enhanced oil recovery from low-permeability reservoirs. J. Pet. Sci. Eng. 168, 390–399. https://doi.org/10.1016/j.petrol.2018.04.073

[6] Meng, M., Ge, H., Ji, W., Wang, X., (2016). Research on the auto-removal mechanism of shale aqueous phase trapping using low field nuclear magnetic resonance technique. J. Pet. Sci. Eng. 137, 63–73. https://doi.org/10.1016/j.petrol.2015.11.012

[7] Liang, T., Zhou, F., Lu, J., (2017b). Evaluation of wettability alteration and IFT reduction on mitigating water blocking for low-permeability oil-wet rocks after hydraulic fracturing. Fuel 209, 650–660. https://doi.org/10.1016/j.fuel.2017.08.029

[8]Alvarez, J.O., Schechter, D.S., (2016). Altering Wettability in Bakken Shale by Surfactant Additives and Potential of Improving Oil Recovery During Injection of Completion Fluids. Presented at the SPE Improved Oil Recovery Conference, Society of Petroleum Engineers. https://doi.org/10.2118/179688-MS

[9] Penny, G.S., Zelenev, A.S., Long, W., Lett, N.L., Crafton, J.W., (2012b). Laboratory and Field Evaluation of Proppants and Surfactants used in Fracturing of Hydrocarbon Rich Gas Reservoirs. Presented at the SPE Annual Technical Conference and Exhibition, Society of Petroleum Engineers. https://doi.org/10.2118/159692-MS

International Journal of Computational and Experimental Science and ENgineering (IJCESEN)
Vol. 6-No.2 (2020) pp. 127-131
http://dergipark.org.tr/en/pub/ijcesen

ISSN: 2149-9144

Research Article

The Determination of the Uniformity in Road Lighting Using Artificial Neural Networks

Mehmet KAYAKUŞ[1]*, İsmail Serkan ÜNCÜ[2]

[1]Akdeniz University, Faculty of Social Sciences and Humanities Science and Arts Faculty, Business Informatics Department, 07600, Antalya-Turkey
[2]Isparta University of Applied Sciences, Faculty of Technology, Electrical-Electronics Engineering Department, 32200, Isparta-Turkey

* **Corresponding Author** : mehmetkayakus@akdeniz.edu.tr
ORCID: 0000-0003-0394-5862- 0000-0003-4345-761X

Article Info:

DOI: 10.22399/ijcesen.753944
Received : 17 June 2020
Accepted : 13 July 2020

Keywords

Road Lighting
Uniformity
Artificial Neural Networks

Abstract:

To ensure that drivers can travel safely, it is necessary to provide good visibility conditions of the road lighting. Thanks to good road lighting, accident rates will decrease, pedestrians' safety will be increased and drivers will be able to travel comfortably. Road lighting standards are included in CIE's 115 "Recommendations for the Lighting of Roads for Motor and Pedestrian Traffic". According to this standard, there are 6 different lighting classes according to the road definition. There are different lighting standards for each class. These are: average luminance (L_{ave}), overall uniformity (U_0), longitudinal uniformity (U_1), disability glare (TI), lighting of surroundings (SR). Uniformity is a measurement of how equally light is distributed on the road. Overall uniformity ratio is of minimum luminance to mean luminance and longitudinal uniformity is the ratio of minimum luminance to maximum luminance. If the uniformity is good, all objects on the road can be easily seen by drivers. In this study, a new method was used to measure the uniformity of the road. Unlike classical methods, image processing and artificial intelligence techniques are used to calculate luminance and uniformity. The uniformity results of the test roads were examined to meet the standards according to the road class.

1. Introduction

The main purpose of road lighting is to ensure that drivers and pedestrians can travel safely and comfortably. Improving road lighting is a way to reduce the number of fatal and personal injury accidents[1-3].
Road lighting standards are included in CIE's 115 "Recommendations for the Lighting of Roads for Motor and Pedestrian Traffic" [4, 5]. According to this standard, there are 6 different lighting classes according to the road definition. There are different lighting standards for each class. These are, average luminance (L_{ave}), overall uniformity (U_0), longitudinal uniformity (U_1), disability glare (TI), lighting of surroundings (SR).

Table 1. *Road Lighting Standards [4, 5]*

Lighting classes	L_{ort}	U_o	U_1	TI (%)	SR
M1	≥2.0	≥0.4	≥0.7	≤10	≥0.5
M2	≥1.5	≥0.4	≥0.7	≤10	≥0.5
M3	≥1.0	≥0.4	≥0.6	≤15	≥0.5
M4	≥0.75	≥0.4	≥0.6	≤15	≥0.5
M5	≥0.50	≥0.35	≥0.4	≤15	≥0.5
M6	≥0.30	≥0.35	≥0.4	≤20	≥0.5

Overall uniformity [6]: Overall uniformity is a measure of how evenly lit the road surface is. The overall uniformity is established by dividing the minimum of luminance (L_{min}) by the average luminance (L_{ave}) [7]:

$$U_0 = L_{min}/L_{ave} \quad (1)$$

Longitudinal uniformity [8]: Longitudinal uniformity is a measure to reduce the intensity of bright and dark banding on road lit surfaces. In design it is expressed as the ratio of the minimum to maximum luminance within the lane of travel [7]:

$$U_1 = L_{min}/L_{max} \quad (2)$$

wherein L_{ave} the average road surface luminance, L_{min} and L_{max} are the minimum and maximum luminance on the central lane line passing through the observer position [6].

It is important to ensure uniformity when designing lighting in areas where artificial lighting is needed [9]. Thus, dark and light areas can be avoided [10]. In addition, lighting homogeneity should be provided for safety and comfort indoors and outdoors [11]. The uniformity of light is the most useful parameter that can define the quality of the field with a single value [12].

Higher luminous smoothness provides better passenger visual comfort [8]. It is desired that the level of illumination is the same on the illuminated surface, that is, the uniformity factor is 1. If uniformity is not achieved, the eye will strive to adapt itself to different levels of lighting and will be tired quickly [13, 14].

Special studies are carried out to ensure uniformity in road lighting. For example, Hu and Qian [15], in their study, they designed a special lens for LED luminaires used in lighting to provide high uniformity on the road surface. As a result of this study, overall illuminance 0,90; longitudinal uniformity has reached 0.85. Coşkuner and Öztop [14] stated that it is necessary to use diffuse beams of light sources to ensure uniformity and place them close together. Another study emphasized that it is necessary to increase the number and strength of LED lamps to increase uniformity[10].

Luminous values of many points in the measurement area have an effect on uniformity indices. Therefore, any changes in this area will affect the illumination homogeneity. Many parameters, including lighting distribution, area geometry, lamps, luminaire and electrical properties, will affect uniformity. Many of these factors have an impact, both initially and over time. Because changes in these factors are difficult to predict [16].

In this study, a software was used to calculate the overall uniformity and longitudinal uniformity on the road by using image processing and artificial intelligence techniques.

2. Methods and Materials

In this study, a software based system has been developed to calculate overall uniformity and longitudinal uniformity. The system consists of 3 basic stages.

In the first stage, the road was photographed according to the determined standards. The image acquisition system has been developed to establish a standard for the photographs taken. Thus, it will be provided to take photographs on the same standards on different roads.

In the second stage, the photographs taken are transferred to the developed software. Using the software, the measurement areas of the road were determined from the images and this area was removed from the image and transferred to a new image file.

In the third stage, the luminance of the road was calculated. For this, reference points have been determined on the road; a correlation is established between the luminance of these points and the pixel values (R, G, B). The luminance of the road is calculated according to the observer by using artificial neural networks [1], one of the artificial intelligence techniques for this correlation. This stage was carried out in the previous study [17].

At the last stage, overall uniformity and longitudinal uniformity are calculated with the developed software. Minimum uniformity was analysed according to the road class. The flow chart of the system operation is given in Figure 1.

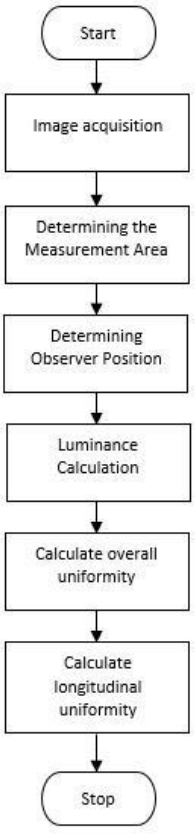

Figure 1. *Flow-chart of the system operation*

2.1. Image Acquisition System

An image acquisition system has been created to take a photo of the road. This system consists of tripod, camera and lens (Canon Eos 200D, Lens: 18-55mm). Some precautions have been taken when taking pictures to avoid affecting measurements. The flash equipment of the image acquisition system has not been used, and the manual settings of the camera are used. This prevents the machine from correcting the automatic photo after the photo is taken. The .raw file format is also used as a photo format. Thus, the procedures were performed on the original photo.
The image acquisition system is set to a height of 1.5m from the ground and photographed at the same angle as the luminance meter. Figure 2 shows the image acquisition system.

Figure 2. *Image acquisition system*

2.2. Determining the measurement area of the road

In this step, the first photo of the road is uploaded to the system. Then the corners of the measurement areas on the road are marked. The system saves the space between these points as a new photo as a measurement area. Figure 3 shows the process of "Determining the Measurement Area of the Road". The developed system determines the observer at the midpoint of each road lane.

2.3. Luminance calculation

Using the artificial neural network method, the luminance value was calculated according to the observer. An artificial neural network model was designed with three input (R, G, B) nodes, three hidden layers and one output (luminance) layer. There are 2-4-5 nodes in three hidden layers. In this design, the backpropagation algorithm network model is used [17]. artificial neural network model is shown in Figure 5.

Figure 3. *Determining the Measurement Area of the Road*

Figure 4. *The position of the observer.*

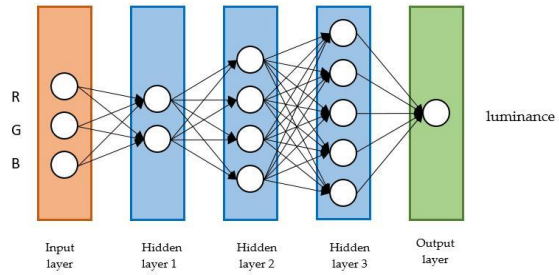

Figure 5. *Artificial neural network model*

3. Experimental Study

Roads have been selected in Antalya, Konyaaltı district in accordance with M3 road lighting class. Although the roads provide the same standard, it has different features. Asphalt structure, homogeneity, number of luminaires, lamp feature, pollution rate of lamps, efficiency of lamps, interval between luminaires differ. The roads are shown in Figure 6. The photos of the test roads were transferred to the software and the measurement areas on the road were determined by the software. Luminance were calculated according to the observer. The calculated luminance is shown in Table 2.

Figure 6. *Test Roads*

Table 2. *Luminance on the Road*

ID	Road ID					
	Road 1		Road 2		Road 3	
	Lane A	Lane B	Lane A	Lane B	Lane A	Lane B
1	2,54	2,63	1,51	1,85	2,47	2,51
2	2,62	2,79	1,92	2,01	1,95	2,32
3	2,2	2,32	1,1	1,95	1,62	2,02
4	1,53	2,01	0,69	1,2	1,24	1,95
5	1,86	1,55	0,59	1,1	1,97	2,22
6	0,55	0,10	0,55	0,95	1,82	2,19
7	0,68	0,15	0,44	0,75	1,07	1,65
8	0,65	0,17	0,43	0,67	1,19	1,55
9	0,65	0,29	0,35	0,55	1,29	1,65
10	0,72	1,65	0,33	0,46	1,22	1,55
11	0,66	1,90	0,21	0,32	1,67	1,92
12	0,71	2,1	0,39	0,44	2,41	2,77
13	1,36	2,12	0,43	0,67	3,07	3,35
14	1,52	2,02	0,66	0,88	3,67	3,95
15	1,37	1,95	0,92	0,99	3,01	3,65
16	0,87	1,85	0,96	1,01	2,24	2,65

Uniformity was calculated according to the luminance of the road. Uniformities of roads are shown in Table 3.

Table 3. *Uniformity of Roads*

Road ID		Luminance (cd/m²)			Uniformity	
		L_{ave}	L_{min}	L_{max}	U_0	U_1
Road 1	Lane A	0,28	0,55	2,62	0,43	0,21
	Lane B	1,60	0,10	2,79	0,06	0,04
Road 2	Lane A	0,72	0,21	1,92	0,29	0,11
	Lane B	0,99	0,32	2,01	0,32	0,16
Road 3	Lane A	1,99	1,07	3,67	0,54	0,29
	Lane B	2,37	1,55	3,95	0,65	0,39

The measured paths are the M3 lighting class and the standard required for longitudinal uniformity (U_1) is 0.6 and the desired value for overall uniformity (U_0) is 0.4. The longitudinal uniformity and overall uniformity rankings are the same from the best to the worst in all three ways: Road ID C, Road ID A, Road ID B. 50% of the lanes on the tested roads meet the desired longitudinal uniformity condition. For overall uniformity, no lane in any roads could provide the desired value.

4. Conclusions

Lighting should be uniform all the road. Road lighting with low homogeneity has a negative effect on human psychology. It prevents drivers from traveling comfortably and causes fatigue. These reasons increase the probability of an accident at night.

Generally, only average luminance is taken into consideration in road lighting. Although it is in the standards, uniformity is not taken into consideration sufficiently. If good lighting is desired, it should be taken into consideration in uniform as much as the luminance.

Uniformity can change over time. Decreases in the efficiency of lamps, environmental factors and incorrectly planned lighting designs affect uniformity. Therefore, periodically, the luminance in the road should be measured and uniformity should be calculated.

Uniformity can be measured easily and quickly with the system developed in this study. Lighting results can be improved with the results obtained here: Lighting results can be improved with the

results obtained here: The location of the luminaires can be adjusted again, environmental factors affecting the lighting (tree, pollution rates) can be kept under control.

References

[1] A.K. Jägerbrand, J. Sjöbergh, "Effects of weather conditions, light conditions, and road lighting on vehicle speed," SpringerPlus, 5(1), 2016.

[2] M.T. Vaaja, M. Kurkela, M. Maksimainen, J.P. Virtanen, A. Kukko, V.V. Lehtola, J. Hyyppä, H. Hyypp, "Mobile mapping of night-time road environment lighting conditions," Photogrammetric journal of Finland, 26(1), 1-17, 2018.

[3] A. C. Sutandi, R. D. A. Pinem, "The application of road lighting standard towards sustainable transportation in large cities in Indonesia," Procedia Engineering, 171, 1463-1471, 2017.

[4] C. Publikacja, "CIE 115-2010: Lighting of roads for motor and pedestrian traffic," CIE, Vienna, 2010.

[5] Road Lighting Calculations, 2019.

[6] Z. Feng, Y. Luo, Y. Han, "Design of LED freeform optical system for road lighting with high luminance/illuminance ratio," Optics express, 18(21), 22020-22031, 2010.

[7] M. Jackett, W. Frith, "Quantifying the impact of road lighting on road safety—A New Zealand Study," IATSS research, 36(2), 139-145, 2013.

[8] M. Alrubaih, M. F. M. Zain, M. Alghoul, N. L. N. Ibrahim, M. Shameri, O. Elayeb, "Research and development on aspects of daylighting fundamentals," Renewable and Sustainable Energy Reviews, 21, 494-505, 2013.

[9] T. İnan, "An investigation on daylighting performance in educational institutions," Structural Survey, 2013.

[10] A. Burton, H. Le Minh, Z. Ghasemlooy, S. Rajbhandari, "A study of LED lumination uniformity with mobility for visible light communications," in 2012 international workshop on optical wireless communications (IWOW), 1-3, 2012.

[11] A. Galatioto, M. Beccali, "Aspects and issues of daylighting assessment: A review study," Renewable and Sustainable Energy Reviews, 66, 852-860, 2016.

[12] S. Carlucci, F. Causone, F. De Rosa, L. Pagliano, "A review of indices for assessing visual comfort with a view to their use in optimization processes to support building integrated design," Renewable and sustainable energy reviews, 47, 1016-1033, 2015.

[13] M. Güner, A.A. İlleez, "Konfeksiyon İşletmeleri Kalite Kontrol Departmanlarındaki Aydınlatma Seviyeleri," presented at the IV. Ulusal Aydınlatma Sempozyumu, İzmir, Türkiye, 2007.

[14] S. Coşkuner, H. Öztop, "Farklı kullanım alanlarının aydınlatılması: verimlilik ve temel ilkeler," Hacettepe Üniversitesi Sosyolojik Araştırmalar E-Dergisi, pp. 1-20, 2016.

[15] X. Hu, K. Qian, "Optimal design of optical system for LED road lighting with high illuminance and luminance uniformity," Applied Optics, 52(24), 5888-5893, 2013.

[16] K. W. Houser, M. Wei, M. P. Royer, "Illuminance uniformity of outdoor sports lighting," Leukos, 7(4), 221-235, 2011.

[17] M. Kayakuş and I. Üncü, "Research note: the measurement of road lighting with developed artificial intelligence software," Lighting Research & Technology, 51(6), 969-977, 2019.

International Journal of Computational and Experimental Science and ENgineering (IJCESEN)
Vol. 6-No.2 (2020) pp. 132-137
http://dergipark.org.tr/en/pub/ijcesen

ISSN: 2149-9144

Research Article

The Relationship Between the Incidence of the Vitamin D Deficiency and the Heart Failure Stages in Patients with Chronic Heart Failure

Gökhan KESKİN*

Assistant Prof., Amasya University Sabuncuoglu Serefeddin Education and Research Hospital, Department of Cardiology

* **Corresponding Author**: gokhan.keskin@amasya.edu.tr
ORCID: 0000-0002-1695-5624

Article Info:

DOI: 10.22399/ijcesen.730683
Received: 01 June 2020
Accepted: 31 July 2020

Keywords

Heart Failure
Vitamin D
Vitamin D Deficiency
Parathormone

Abstract:

Objective: Vitamin D deficiency is known to be associated with increased incidence of hypertension, myocardial infarction (MI), heart failure and stroke. This study aimed to investigate the relationship between vitamin D deficiency and heart failure stages in patients with chronic heart failure.

Materials and Methods: This study included 106 patients who were either treated in clinics or admitted to outpatient cardiology clinics between January and July 2010 in Turkey High Specialized Hospital. The patients were classified between NYHA classes I-IV and physical examination, echocardiography, electrocardiography and routine blood tests were performed on all patients. Blood tests were performed to determine vitamin D and parathormone levels from all patients.

Results and conclusion: The mean age of the patients included in the study was 65.67 ± 10.4 years. At least one risk factor was present in 95% of the patients, and hypertension was found as the most prevalent factor (73.58%). According to the NYHA classification, 41.50% of the vitamin D levels were less than 25 nmol / L and vitamin D levels of patients with NYHA class III and IV heart failure were significantly different ($p < 0.05$). Comparison of the vitamin D levels in the patients with heart failure class C and D were significantly different ($p < 0.05$). Moreover, a statistically positive correlation was found between the heart failure stages and Vitamin D levels ($p < 0.05$; $r = 0.267$). A negative and statistically significant relationship was identified between vitamin D and parathormone levels ($p < 0.05$, $r = -0.417$). Correlation analysis showed that as the class of heart failure increased, the severity of vitamin D deficiency elevated, and this was accompanied with an increased level of parathormone.

Conclusion: In conclusion it was observed that the prevalence of vitamin D deficiency was high in patients with stage C and D heart failure. Reasons for this may include the widespread urban lifestyle and inadequate daylight, disordered vitamin D absorption from intestines due to heart failure, and a decrease in active vitamin D synthesis due to a decrease in renal perfusion. When considering the roles of vitamin D on ventricular contractility, and vitamin D replacement therapy should be considered in heart failure patients and this should be investigated by more comprehensive studies.

1. Introduction

Chronic heart failure is a complex syndrome secondary to hereditary / acquired anatomical or functional cardiac anomalies, affecting approximately 23 million people worldwide and is the leading cause of mortality and morbidity [1-2]. Approximately 10 million patients in Europe are affected by chronic heart failure, and despite significant advances in therapeutic options in recent years, no significant changes in prognosis have been observed in the five-year survival rate of

patients diagnosed with chronic heart failure that is 35-50% [3-4]. There are several mechanisms in the pathogenesis of heart failure that explain the suboptimal effect of existing treatments on the clinical outcome, including hemodynamic abnormalities, neurohormonal activation, enhanced inflammation and micronutrient availability [5]. Vitamin D is an important micronutrient that plays an important role in autocrine and paracrine regulation of cellular functions and in the growth and differentiation of many organs, including the heart. In fact, vitamin D deficiency is known to be associated with increased incidence of hypertension, myocardial infarction (MI), heart failure, and stroke [6]. Although vitamin D was discovered about a century ago, our knowledge about it has altered recently. Over the years, its effects on calcium absorption, roles in bone health, and more recently, effects on neuromuscular function have been proven. In the last 15 years, it has been reported that vitamin D has been metabolized in various cells and tissues such as macrophages and placenta, its receptors are present in almost all body organs and it affects the function of more than 60 genes [7]. Epidemiological studies showed that vitamin D deficiency is associated with increased hypertension, MI, stroke, chronic kidney disease, and type 2 diabetes mellitus [8]. Low vitamin D levels have been found to activate the renin-angiotensin-aldosterone system, cause inflammatory response and endothelial dysfunction. Patients suffering from cardiovascular diseases are often deficient in steroid hormone vitamin D, and vitamin D deficiency has been shown to be associated with the development of chronic heart failure in a number of studies [9]. Around 90% of patients with chronic heart failure, even the ones living in sunny climate, have hypovitaminosis D [10]. Vitamin D has a number of pleiotropic effects that may affect the severity of the disease and adjustment of its doses in chronic heart failure is required [11].Significant observational evidences revealed a link between low vitamin D status and the risk of clinical outcomes in heart failure, including ventricular remodelling and mortality. However, studies evaluating vitamin D supplementation and its impact on clinical outcomes in heart failure have generally been small and inconclusive [12]. The randomized control trial on 400 patients in which the effect of vitamin D supplementation on mortality in heart failure was investigated revealed no change in echocardiographic parameters after 12 months and 36 months, while an increase in the left ventricular diastolic diameter was observed in patients over 50 years of age, however, that increase in the diameter decreased after 36 months [2].

Based on the vascular effects of vitamin D has recently been reported, this study aimed to determine the relationship between low vitamin D incidence and heart failure stages in patients with chronic heart failure.

2. Materials and methods

Type of the Study

This study was a descriptive correlational study.

Location of the Study Conducted

The research was conducted at the Cardiology Clinic in Turkey High Specialization Hospital between January 2010 and July 2010.

Research Population

This study was conducted on the patients either admitted to the cardiology outpatient clinics and the patients treated with the diagnosis of chronic heart failure in Turkey High Specialization Hospital between January 2010 and July 2010.A total of 106 patients (25 from cardiology clinics and 81 from cardiology outpatient clinics) who were diagnosed with chronic heart failure and agreed to participate in the study were included.

Data Collection Tools

Data including physical examination, echocardiography, electrocardiography and routine blood tests of the patients included in the study were examined. Before the study, all patients were informed about the aim of the study and their informed consent forms were obtained. Data were collected by using personal information form and heart failure classifications of the patients were determined according to the New York Heart Association (NYHA) Functional Classification.

Table 1: *NYHA functional classification Criteria [13]*

Class	NYHA functional classification
I	Patients have cardiac disease but without resulting in limitation of physical activity. Ordinary physical activity does not cause undue fatigue, palpitation, dyspnea or anginal pain.
II	Patients have cardiac disease resulting in slight limitation of physical activity. Patients are comfortable at rest. Ordinary physical activity results in fatigue, palpitation, dyspnea or anginal pain.
III	Patients have cardiac disease resulting in notable limitation of physical activity. Patients are comfortable at rest. Less than ordinary physical activity results in fatigue, palpitation, dyspnea or anginal pain.
IV	Patients have cardiac disease resulting in inability to carry on any physical activity. Symptoms of cardiac insufficiency or of the anginal syndrome may be present even at rest. Discomfort is increased if any physical activity is undertaken.

The New York Heart Association (NYHA) Functional Classification: NYHA functional classification is a widely used method for classifying the extent of the heart failure in patients with heart failure (Table 1). Its validity was accepted in 1928 and it was revised many times. Its final revised version was published in 1994.

Collection and Evaluation of Data

The data were collected by the researcher between January 2010 and July 2010.In the study, patients who had chronic heart failure were interviewed once, and the information in the informed consent form was read at the interview and their consents were obtained. The treatments of the patients who agreed to participate in the study were planned in accordance with the current treatment guidelines after the admission of the patients to outpatient clinic diagnostic procedures. Their NYHA functional capacity were determined and patients with stage C and D heart insufficiency and with class III and IV and heart failure included in the study and vitamin D deficiency were evaluated. In our study, IMMUCHROM VIT D kits were used, and vitamin D levels were evaluated by using high-performance liquid chromatography (HPLC) method on a SHIMADZU HPLC machine. Then the patients were interviewed, and the interview lasted approximately 30 minutes.

Pathological Q waves, branch blocks, atrial fibrillation, ventricular arrhythmias, ST segment and T wave changes were examined by evaluating the results of 12-lead electrocardiograms of the patients. Heart size and its borders, lung tissue, pulmonary vascular structures, abnormal densities and presence of pleural fluid were examined by echocardiography. Routine blood tests (complete blood count, fasting blood sugar, blood urea nitrogen, creatinine, serum sodium and potassium levels, HDL, LDL, total cholesterol, triglyceride levels, liver and thyroid function tests) were performed. Plasma samples taken from the patients for vitamin D were obtained in the morning while the patients were fasting, and the samples were stored in accordance with the cold chain standards.

The statistical evaluation of the obtained data was conducted by using SPSS for windows computer package program (version 20.0). In the analysis of the data, besides the descriptive statistics (mean, standard deviation, minimum and maximum values and ratio), t-test to test the differences between two groups and chi-square test and Pearson correlation analysis to determine the direction and degree of the relationship between the variables were performed. For determination of the factors affecting mortality, multivariate logistic regression analysis was performed with the variables found important as a result of two-way analysis. A p value lower than 0.05 was considered as statistically significant.

Ethical Aspect of the Research

Approval for this study was obtained from the institutional Educational Planning Board of Turkey High Specialized Hospital. The study was carried out in accordance with the Helsinki Declaration Principles.

Limitations of the Study

Patients receiving renal replacement therapy, having renal insufficiency, received oncological treatment within last one year, diagnosed with primary pulmonary hypertension, having a life expectancy less than six months, having severe pulmonary disorders, having recent surgical history, having history of acute coronary syndrome or having history of pulmonary embolism were excluded from the study although the they were diagnosed with coronary insufficiency.

Results

Table 2 shows personal information of the patients with the percentage and frequency values. Mean age of the participants was 65.67 ± 10.4, and it was found that there was no statistically significant difference between Vitamin D levels and age factor ($p > 0.05$).The educational status of the majority of the patients (74.52%) was middle school and below and the majority of them were male patients (66.99%). Considering the presence of risk factors that may trigger chronic heart failure in patients, it was determined that hypertension was accompanied in the vast majority (73.58%), and it was found that there was a significant difference in comparison with vitamin D levels ($p = 0.002$; $p < 0.05$).In addition, 88.67% of patients stated that they had palpitations.

According to the data obtained as a result of the physical examinations and the test results of the participants, according to the NYHA classification of patients, classes of heart failure were defined. While planning the treatment schedule according to the NYHA classification and other test results, planning was made considering the information from latest the heart failure guidelines (2010) information. A comparison was made between the NYHA classification of patients and routine blood test results. According to the analysis, while there were significant differences between creatine, BUN, uric acid, sodium, LDL, triglyceride, albumin, and haemoglobin levels in patients with NYHA class III and IV heart failure ($p < 0.05$), potassium, HDL, total cholesterol, total protein and WBC levels were not significantly different between two patient groups ($p > 0.05$). In addition,

Table 2: *Comparison of the socio-demographic characteristics of the participants (n = 106)*

	Participants (n=210)		Test Value (Comparison with Vitamin D Levels)	
Socio-demographic Features	**n**	**%**	x^2 / **t***	**p**
Age				
< 45 age	10	9,43	0,222	0,895
46-56 age	12	11,32		
> 57 age	84	79,24		
Average age (mean±SD)	65,67±10,4			
Gender				
Female	35	33,01	1,224	0,269
Male	71	66,99		
Education Status				
Middle school or lower	79	74,52	0,172	0,678
High school and higher	27	25,47		
Presence of a Risk Factor*				
Hypertension	78	73,58	***9,427***	***0,002***
Smoking	46	43,39		
Family History of	56	52,83		
Hyperlipidaemia	44	41,50		
Diabetes	47	44,33		
Presence of Disease-Specific Symptoms *				
Shortness of breath	52	49,05	1,742	0,419
Chest Pain	67	63,20		
Palpitation	94	88,67		

***** Since there was more than one risk factor in the participants, each risk factor has been evaluated according to whole population.

when the vitamin D levels were compared according to NYHA classes, a statistically significant difference between the two groups were observed (Table 3; p = 0,000; p <0.05). In the post hoc analysis (Z test) made according to the result obtained, it was found that the group that constituted the difference was the 50-99.9 nmol / L group of the NYHA class III group.

Table 3: *Comparison of Vitamin D Levels According to NYHA Classification*

		NHYA Groups						Chi-square	
		NHYA III		NHYA IV		Total			
		n	%	n	%	n	%	x^2	p
Vitamin D Level	<25 nmol/L	30	37,97	14	51,85	44	41,50	27.626	0.000
	25-49,9 nmol/L	23	29,12	8	29,63	31	29,25		
	50-99,9 nmol/L	26	32,91	5	18,52	31	29,25		
	Total	79	100,0	27	100,0	106	100,0		

Table 4 shows the analysis results between participants' heart failure stages and vitamin D levels. According to the analysis performed based on the normal distribution of groups of patients with heart failure at stage C and D levels, there was a significant difference between heart failure levels and vitamin D levels (p = 0.000; p <0.05). In the post hoc analysis (Z test) made according to the result obtained, it was found that the <25 nmol / L group of stage D patients that caused the statistical difference in vitamin D level group. According to the correlation analysis between the stages of heart failure and vitamin D levels, there was a positive correlation between the groups (p = 0.006; r = 0.226).In addition, according to the correlation analysis between vitamin D and parathormone levels of patients, there was a negative and significant correlation between two (p = 0.000, r = -0.417).According to these results, it was determined that as the stage of heart failure increased, the level of vitamin D decreased, and this was accompanied by an increase in the level of parathormone.

Table 4: *Comparison of the Heart Failure Stages and Vitamin D Levels*

		Heart Failure Stage Grouping						Chi-square	
		Stage C		Stage D		Total			
		n	%	n	%	n	%	x^2	p
Vitamin D Level	<25 nmol/L	36	39,56	8	53,33	44	41,50	20.218	0,000
	25-49,9 nmol/L	27	29,68	4	26,67	31	29,25		
	50-99,9 nmol/L	28	30,76	3	20,00	31	29,25		
	Total	91	100,0	15	100,0	106	100,0		

Discussion / Conclusion

Vitamin D deficiency is a common and preventable condition. It is estimated to affect more than 1 billion people worldwide. One of the earliest prospective studies to confirm the relationship between vitamin D deficiency and cardiovascular disease was conducted by Wang et al. in 2008 [14]. After providing appropriate treatment for the risk factors in the patients, researchers found a significant association between increased incidence of cardiovascular disease and vitamin D deficiency. It is known that there are various risk factors for cardiovascular diseases not only in Turkey but also in the world. One of these factors is gender [14].Our study was similar to the literature [15], and it was observed that the number of male patients were more than the number female patients, and the mean age (65.67 ± 10.4 years) was similar to the ones with heart failure.

One of the effects of vitamin D on the cardiovascular system is by mediating parathormone levels. It is well known that vitamin

D is included in the calciotropic hormone system together with parathormone [16]. Our research results also showed that there was a negative and significant association between the groups according to the correlation analysis between vitamin D levels and parathormone levels of patients (p = 0,000, r = -0,417).According to these results, it was determined that as the stage of heart failure increases, the level of vitamin D decreases, and this is accompanied by an increase in the level of parathormone. This result is parallel with the literature. Gruson et al. in 2012 stated that the results obtained with the NYHA functional classification were correlated with the results obtained from the studies that they have compared the levels of vitamin D and parathormone levels of patients with chronic heart failure according to the NYHA classification system [17]. A similar result was obtained in our study and it was found that there was a statistically significant correlation between NYHA classification and vitamin D levels. Liu et al. (2011) in their study on the population with stage C heart failure [18], the prevalence of patients in NYHA class III compared to our study were 52% compared to 72%, mean vitamin D levels (<25 nmol / L level) were 14.6ng / mL, whereas in our study the mean vitamin D levels were 36.6 nmol / L in NYHA III. Finally, Gotsman et al. (2012) measured the 25OHD levels by immunoassay in 3009 patients with heart failure and compared it with the levels in the control group [19]. Our study found the prevalence of severe vitamin D deficiency (<10ng / mL or 25 nmol / L) as 34%, similar to that of Gotsman et al. (34%), and confirmed that the lower levels of 25OHD compared to healthy people as it was in patients with heart failure in the study of Gotsman et al. Other data in the literature support this relationship between 25OHD and heart failure. In addition, our results regarding the vitamin D levels according to the stages of heart failure, a similar result was obtained in the NYHA classification. Accordingly, the average vitamin D levels in patients in the stage C group were determined as 36 nmol / L, while the mean vitamin D levels in the stage D group were 28.9 nmol / L and the difference between the groups was found statistically significant (p <0.05). Significant observational evidence has linked low vitamin D status to many problems that may affect the clinical course of heart failure, including cardiac insufficiency, ventricular remodelling and mortality. However, studies evaluating the effect of vitamin D supplementation on markers and clinical outcomes in heart failure have generally been limited and inconclusive. There is insufficient data to recommend routine vitamin D evaluation or vitamin D supplementation for the prevention or treatment of chronic heart failure. Strong and detailed prospective studies are required for clinical outcomes. In conclusion, considering the contribution of vitamin D on ventricular contractility, detection of the vitamin D deficiency and the efficacy of replacement therapy in the heart failure patients with vitamin D deficiency should be investigated by more comprehensive studies.

References

[1]. Borst MH, Vervloet MG, Wee PM, Navis G. Cross talk between the renin-angiotensin-aldosterone system and vitamin D-FGF-23-klotho in chronic kidney disease. JASN. 2011;22: 1603–1609. https://doi.org/10.1681/asn.2010121251

[2]. Zitterman A, Ernst JB, Prokop S, Fuchs U, Gruszka A, Dreier J. et all. Vitamin D supplementation of 4000 IU daily and cardiac function in patients with advanced heart failure: The EVITA trial. International Journal of Cardiology, 2019;280:117-123. https://doi.org/10.1016/j.ijcard.2019.01.0270167-5273

[3]. Bleumink GS, Knetsch AM, Sturkenboom MC, Straus SM, Hofman A, Deckers JW, Witteman JC, Stricker BH. Quantifying the heart failure epidemic: prevalence, incidence rate, lifetime risk and prognosis of heart failure The Rotterdam Study. Eur Heart J 2004; 25:1614-19. https://academic.oup.com/eurheartj/article/25/18/1614/400157

[4]. Levy D, Kenchaiah S, Larson MG, Benjamin EJ, Kupka MJ, Ho KK, Murabito JM, Vasan RS. Long-term trends in the incidence of and survival with heart failure. N Engl J Med 2002; 347:1397-1402. DOI: 10.1056/NEJMoa020265

[5]. Rauchhaus M, Doehner W, Francis DP, Davos C, Kemp M, Liebenthal C, Niebauer J, Hooper J, Volk HD, Coats AJ, Anker SD. Plasma cytokine parameters and mortality in patients with chronic heart failure. Circulation. 2000; 102: 3060-67. https://doi.org/10.1161/01.cir.102.25.3060

[6]. Anderson JL, May HT, Horne BD, Bair TL, Hall NL, Carlquist JF, Lappé DL, Muhlestein JB; Intermountain Heart Collaborative (IHC) Study Group. Relation of vitamin D deficiency to cardiovascular risk factors, disease status, and incident events in a general healthcare population. AmJCardiol.2010;106:963-68. https://doi.org/10.1016/j.amjcard.2010.05.027

[7]. Whitham, D.M. Vitamin D in chronic heart failure. Curr Heart Fail Rep. 2011; 8:123–130. DOI 10.1007/s11897-011-0048-6 https://doi.org/10.1007/s11897-011-0048-6

[8]. Desai CK, Huang J, Lokhandwala A, Fernandez A, Riaz IB, Alpert JS. The role of vitamin supplementation in the prevention of cardiovascular disease events. Clin Cardiol. 2014; 37:576–581. https://onlinelibrary.wiley.com/doi/full/10.1002/clc.22299

[9]. Ford JA, MacLennan GS, Avenell A, Bolland M, Grey A, Witham M. et al. Cardiovascular disease and vitamin D supplementation: trial analysis, systematic review, and meta-analysis. Am J Clin Nutr.2014;100:746–55. DOI:10.3945/ajcn.113.082602

[10]. Ameri P, Ronco D, Casu M, Denegri A, Bovio M, Menoni S., High prevalence of vitamin D deficiency and its association with left ventricular dilation: an echocardiography study in elderly patients with chronic heart failure. Nutr Metab CardiovascDis.2010;20:633–40. https://doi.org/10.1016/j.numecd.2010.01.002

[11]. Witte KK, Byrom R. Micronutrients for chronic heart failure: end of the road or path to enlightenment? J Am Coll Cardio HF. 2014; 2:318–20. https://doi.org/10.1016/j.jchf.2014.04.001

[12]. Brinkley MD, Omair MA, Sandip KZ, Wang TJ. Correction to: Vitamin D and heart failure. Current HeartFailureReports.2018;15:280. https://doi.org/10.1007/s11897-018-0394-8 .

[13]. The Criteria Committee of the New York Heart Association. Nomenclature and criteria for diagnosis of diseases of the heart and blood vessels. Boston: Little Brown, 1964.

[14]. Wang TJ, Pencina MJ, Booth SL, Jacques PF, Ingelsson E, Lanier K, et all. Vitamin D Deficiency and risk of cardiovascular disease. Circulation. 2008;117:503-511. https://doi.org/10.1161/CIRCULATIONAHA.107.706127

[15]. Porto CM, Silva VDL, Luz JSB, Filho BM, Silveria M. Association between vitamin D deficiency and heart failure risk in the elderly. ESC Heart Failure. 2018; 5:63–74. https://doi.org/10.1002/ehf2.12198

[16]. Zitterman A, Ernst JB. Calciotropic and phoshaturic hormones in heart failure. Nutrition, Metabolism & Cardiovascular Disease. 2016; 26:971-9. https://doi.org/10.1371/journal.pone.0164459

[17]. Gruson D, Lepoutre T, Ahn SA, Ketelslegers JM, Rousseau MF. Increased circulating concentrations of bioactive PTH 1-84 in patients with heart failure. Journal of Endocrinological Investigation. 2012;35(11):987–991. DOI: 10.3275/8286

[18]. Liu LC, Voors AA, van Veldhuisen DJ, van der Veer E, Belonje AM, Szymanski MK, et al. Vitamin D status and outcomes in heart failure patients. European Journal of Heart Failure. 2011; 13:619–625. https://doi.org/10.1093/ eurjhf/hfr032

[19]. Gotsman I, Shauer A, Zwas DR, Hellman Y, Keren A, Lotan C, et al. Vitamin D deficiency is a predictor of reduced survival in patients with heart failure; Vitamin D supplementation improves outcome. European Journal of Heart Failure. 2012; 14:357–366. https://doi.org/10.1093/eurjhf/hfr175